

Day 1 – Wednesday 1st July -

Session 1.A Biomechanics Biomaterials

14h - 14h30	Introduction Prof. Kambiz Kayvantash, Chair in Automotive - Cranfield University		Jazz Page 4
14h30-15h00	Keynote 1 Prof. Ariel Fernandez, Karl F. Hasselmann, Chair in Engineering - Rice University		Jazz Page 18
15h00-15h30	Keynote speaker 2 Mr. F. Bendjellal – Britax		Jazz Page 19
15h30-16h00	Break <i>Sponsors exhibition - Open discussions</i>		Méditerranée
16h00-16h20	Mr. D. Lehmhus Fraunhofer IFAM	Approaches towards Integration of Simulation Techniques for the Description of Smart Materials and Structures	Jazz 1 Page 20
16h20-16h40	Mr. R. Mongrain McGill	Characterization of aortic tissue fracture toughness and stiffness under cyclic fatigue loading	Jazz 1 Page 21
16h40-17h00	Mr. M. Avalle Politecnico di Torino	Mechanical modelling of biopolymer materials	Jazz Page 22
17h00-17h20	Mr. A. Burlibies Faunhofer IFAM	Cancellous Bone - Computational Bone, Remodelling and Manufacturing	Jazz 1 Page 23
17h20-17h40	Miss A. Garo University of the Méditerranée	An inverse finite element method to estimate the bone mechanical properties of the vertebral body	Jazz 1 Page 24
17h40-18h00	Mr Minnock Cranfield University	Simulating the Passage of Ultrasound Through the Phalanx	Jazz 1 Page 25
18h00-18h10	Day conclusion Dr P.J. Arnoux – INRETS		Jazz 1 Page 5
19h00-20h00	Welcome Cocktail		Méditerranée

Session 1.B Biomechanics and Physiology

14h- 14h30	Introduction Prof. Kambiz Kayvantash, Chair in Automotive - Cranfield University		Jazz Page 4
14h30-15h00	Keynote speaker 1 Prof. Ariel Fernandez Karl F. Hasselmann, Chair in Engineering - Rice University		Jazz Page 18
15h00-15h30	Keynote speaker – 2 Mr. F. Bendjellal – Britax		Jazz Page 19
15h30-16h00	Break <i>Sponsors exhibition - Open discussions</i>		Méditerranée
16h00-16h20	Mr. H. Amadi Imperial College London	A Joint Coordinate System for the simulation of the functional kinematics of the glenohumeral joint	Jazz 2 Page 26
16h20-16h40	Mr. D. O'Reilly University of Limerick	Finding forces at the hip joint resulting from everyday activities	Jazz 2 Page 27
16h40-17h00	Mr. S. Li Hubei University	Jockeys posture characteristics on the simulation horse	Jazz 2 Page 28
17h00-17h20	Prof. D. Howard University of Salford	Predictive Modelling of Human Walking Over a Complete Gait Cycle	Jazz 2 Page 29
17h20-17h40	Miss P. Gérus Univ. Méditerranée	Hybrid numerical methods for estimating muscle forces	Jazz 2 Page 30
17h40-18h00	M. F. Coulangeat INRETS	Windscreen material characterization for multibody simulation of pedestrian head impact	Jazz 2 Page 31
17h40-18h00	Day conclusion Prof. Kambiz Kayvantash, Chair in Automotive - Cranfield University		Jazz 2 Page 4
19h00 - 20h00	Welcome Cocktail		Méditerranée

Session 2.A Biomedicine - Biomolecules

9h00 - 9h10	Introduction Dr. PJ Arnoux INRETS		Jazz Page 5
9h10- 9h40	Keynote speaker 3 Mr. D. Cesari INRETS		Jazz Page 36
9h40- 10h00	Gold Sponsor Mrs M. Alexandre – Dassault Simulia Systems		Jazz Page 7
10h00- 10h30	Break Sponsors exhibition - Open discussions		Méditerranée
10h30- 10h50	Mr. C. Savoldelli CHU Pasteur Nice CEMEF	Development of a Finite Element Model of the Temporomandibular Joint for Distraction Osteogenesis Studies	Jazz 1 Page 37
10h50- 11h10	Miss V. Astier INRETS	Finite element simulation of humerus intramedullary nailing: case of torsion loading	Jazz 1 Page 38
11h10- 10h30	Mr. D.G. Woo Yonsei University	Effect of Mandible Trabecular Bone Microstructure on Stress Distribution within Premolar Tooth and Dental Implant using micro-Finite Element Analysis	Jazz 1 Page 39
11h30- 11h50	Mr. T. Heimann INRIA Sophia Antipolis	A Transversely Isotropic Hyperelastic Material for Real-Time FEM Simulations	Jazz 1 Page 40
11h50- 12h10	Mr. A. Completo Universidade de Aveiro	Notching In Anterior Femur with use of Femoral Stems - Finite Element Study	Jazz 1 Page 41
12h10- 14h00	Lunch		Méditerranée

Session 2.B Biomechanics and Physiology

9h00 - 9h10	Introduction Dr. PJ Arnoux INRETS		Jazz Page 5
9h10- 9h40	Keynote speaker 3 Mr. D. Cesari INRETS		Jazz Page 36
9h40-10h00	Gold Sponsor Mrs M. Alexandre – Dassault Simulia Systems		Jazz Page 7
10h00- 10h30	Break Sponsors exhibition - Open discussions		Méditerranée
10h30- 10h50	Miss. C. Conte INRETS	On liver modelling and simulation under trauma situations	Jazz 2 Page 37
10h50- 11h10	Mr. H. Daanouni CEMEF	Development of an Hyperlastic Finite Element Model to Simulate the Behavior of Complex Organs (Envelope and Underlying Tissues)	Jazz 2 Page 38
11h10- 11h30	Mr. S. Roth University of Technology of Belfort-Montbéliard	Influence of mesh density on a finite element model submitted to dynamic loading	Jazz 2 Page 39
11h30- 11h50	Mr. PJ Liotier University of Méditerranée	Spongy bone multicellular unit remodelling model; a physico-chemical approach	Jazz 2 Page 40
11h50- 12h10	PhD. D. Vashishth Rensselaer Polytechnic Instit.	Cohesive Finite Element Approach to Determine Contribution of Bone Quality to Fracture Toughness	Jazz 2 Page 41
12h10- 14h00	Lunch		Méditerranée

Day 2 – Thursday 2nd July – Afternoon

Session 3.A Biomedicine - Biomolecules

14h00-14h20	Mr. D. Willems Materialise	Using FE simulations to optimize implant and medical device design	Jazz 1 Page 51
14h20-14h40	Mr. J. Mejia Mc Gill	Non newtonian and transient effects on the wall shear stress within a stented artery	Jazz 1 Page 52
14h40-15h00	Mr. K. Vlasak SZ Design S.r.l.	Parameterization and Optimization of Balloon Expandable Stent	Jazz 1 Page 53
15h00-15h20	Mr. V. Barbour Lab. Biomechanics	Subject-specific finite element model of a cementless femoral stem	Jazz 1 Page 54
15h20-15h40	Mrs Y. Aminkashani islamic azad university	Modeling the appropriate sleep system and the spine of the patients who suffer from ankylosing-spondylitis, designing and excluding the mattress stiffness cartography according to their sex and body shape.	Jazz 1 Page 55
15h40-16h00	Mr. M. Moatamedi Cranfield University	Multiphysics Modelling of Aorta Implementing a Physiologically Realistic Material Model	Jazz 1 Page 56
16h00-16h30	Break <i>Sponsors exhibition - Open discussions</i>		Méditerranée
16h30-16h50	Prof. R. Mongrain Mc Gill	Simulation based characterization of stenotic vessels	Jazz Page 57
16h50-17h10	Mr. E. Wagnac Ecole Polytechn. Montreal	The effect of strain rate on thoracolumbar spine injuries : a finite element investigation in dynamic compression	Jazz Page 58
17h10-17h40	Keynote speaker4 Mr. H. Delingette, Research Director in the ASCLEPIOS research group, INRIA research center		Jazz Page 50
17h40-18h00	End of the day – Discussion – P.J Arnoux - INRETS		Jazz
18h00-19h00	1/1 meetings		Méditerranée
20h00-20h30	Awards given by Altair Engineering		Beach
20h30	Gala dinner on the beach		Beach

Session 3.B Biomechanics Biomaterials

14h00-14h20	Mr. I. Symeonidis Inst. für Rechtsmed. der Univ. München	Developing a method to simulate injury mechanisms in motorcycle crashes	Jazz 2 Page 59
14h20-14h40	Mr. JS Raul IMFS	Numerical modelling of the shaken baby syndrome	Jazz 2 Page 60
14h40-15h00	Dr. B Serpil Acar Loughborough university	Computational Modelling and Simulations for Pregnant Occupant Safety	Jazz 2 Page 61
15h00-15h20	Mr. J. Delotte CHU Nice	Transformation of the Humos 50th centile Male Humos Model to 50th centile Female Model and proposed methodology to build a Pregnant Model	Jazz 2 Page 62
15h20-15h40	Mr. J. Peres INRETS	Study on the hypothesized Abruptio Placentae Mechanisms	Jazz 2 Page 63
15h40-16h00	Mr. F. MEYER IMFS	Numerical tools for real world whiplash accident investigation	Jazz 2 Page 64
16h00-16h30	Break <i>Sponsors exhibition - Open discussions</i>		Méditerranée
16h30-16h50	Prof. R. Mongrain Mc Gill	Simulation based characterization of stenotic vessels	Jazz Page 57
16h50-17h10	Mr. E. Wagnac Ecole Polytechn. Montreal	The effect of strain rate on thoracolumbar spine injuries : a finite element investigation in dynamic compression	Jazz Page 58
17h10-17h40	Keynote speaker4 Mr. H. Delingette, Research Director in the ASCLEPIOS research group, INRIA research center		Jazz Page 50
17h40-18h00	End of the day – Discussion – J Arnoux - INRETS		Jazz
18h00-18h30	1/1 meetings		Méditerranée
20h00-20h30	Awards given by Altair Engineering		Beach
20h30	Gala dinner on the beach		Beach

SimBio-M

Simulation for Bio- Mechanics, Materials, Medicine, Molecules

Day 3 – Friday 3rd July -

Session 4.A Impact Biomechanics

8h50- 9H00	Introduction Dr. P.J. Arnoux – INRETS		Jazz
9h00- 9h30	Keynote speaker 5 Dr. Peter Zioupos- Cranfield University		Jazz Page 67
9h30-9h50	Mr. J. Sun INRETS	Does neck segment exhibit the same vulnerability according to various impact conditions?	Jazz Page 69
9h50-10h10	Mrs. H. Deck IMFS	Improved model based head injury criteria	Jazz Page 70
10h10-10h40	Break <i>Sponsors exhibition - Open discussions</i>		Mediterranee
10h40-11h00	Miss M. Montava APHM	<i>Petrous Bone fracture identification by FE simulation under side impact</i>	Jazz Page 71
11h00-11h20	Mr.J.F. Libra INRETS	Kinematics and injury patterns of vulnerable road users involved in road accidents with commercial vehicles	Jazz Page 72
11h20-11h50	Keynote speaker 6 Prof. Carl Eric Aubin – Ecole Polytechnique Montreal		Jazz Page 68
11h50-12h00	Conclusion Prof. K. Kayvantash – Cranfield University		Jazz
12h00-13h30	Cloture Cocktail		Méditerranéée

SimBio-M

Simulation for Bio- Mechanics, Materials, Medicine, Molecules

5th Keynote speaker

Dr. Peter Zioupos
Reader in Biomechanics of Materials
Cranfield University
UK
p.zioupos@cranfield.ac.uk



Current activities

Peter Zioupos was elected in 2006 in the Council of the European Society of Biomechanics where he is currently the Chair of the Education Committee. He is a member of the Editorial board: of J.BIOMECHANICS, J.BIONIC ENGINEERING and J.MECHANICAL BEHAVIOUR OF BIOMEDICAL MATERIALS.

Member of the EPSRC Peer Review College.

Member of the: European Society of Biomechanics, International Society of Biomechanics, Institute of Physics and Engineering in Medicine, and a Chartered Scientist (CSci).

He is in charge of the Biomechanics laboratories at Shrivenham and he is active in hard and soft tissue biomechanics research and Bone biomechanics in particular His most recent work was on the Fracture toughness of Cancellous bone and on the Biomechanics of ACL reconstructions He is active in forensics where he has offered consultancy in forensic science legal cases regarding accidental or otherwise caused death, which resulted primarily from bone injuries. He has developed a patent for the 'Forensic determination of age at time of death by analytical laboratory examination of bone matrix. Report

He offers consultancy to industry via nanoindentation studies on fuel cells, health care products, anodising layers, design of test chambers and testing standards. (Microhardness and Nano-hardness laboratories)

One such principle is the concept of nerves, and pain. The latter may not seem desirable, but this clearly is a fallacy. Pain means local processing of sensor information allowing extremely fast reaction in critical situations. Thus there are several reasons why engineering, too, should care for it. Some of the more important ones are related to costs, and the background to these is how engineering handles unexpected events. As a conscientious engineer, you have designed your structure to all the loads to be expected, but what if usage goes beyond the normal? You can introduce safety factors, thus adding weight and reducing efficiency. You can take your critical component out of use deliberately after certain intervals and thoroughly examine it. If you find fault, you will replace or repair, if not, you will put it back in use until the next maintenance interval has passed. What you have done in any case is incurred significant costs. Depending on the branch of industry, this cost is felt more or less heavily. The time a plane is grounded, and cannot earn its revenue, is extremely costly for an airline, while having to perform highly skilled technical tasks no matter what the weather some 10 miles out at sea is a major cost factor in wind energy, which is currently moving its plants offshore.

Nature has its own answer. Consider bones: Their internal structure is an intricate adaptation to major loads that act on them. Cyclic loads are not reflected, though, and neither are one-of-a-time events. This is an innate limitation, since structural change takes time and thus needs a long-lasting stimulus. For this reason, the internal structure is only part of the picture. Besides, there is the periosteum, a thin membrane surrounding the bones, and there are muscles and sinews, and elasticity. The periosteum means nerves and specifically nerve endings receptive to imminent damage, which on being overloaded, to use a technical term, can transmit this information to the consciousness of the individual in question. Depending on severity, this may be felt as pain, which will cause a reaction that is again supported or put to question by feedback from the nerves - either more or less pain. A reflex can be an alternative, a faster way to react on a lower level of consciousness. Here, elasticity of kinematic chains in the human body and local interpretation of signals received via the nerves may be used to advantage – for speed, that is.

Sensors are the technical equivalent of part of this complex system. Muscles and sinews are replaced by actuators, their reactions controlled by microcontrollers. Elasticity may be engineered into technical products, too. These are, in short, the basics. However, there is so far no technical system having a sensor density anywhere near to the nervous system of a human being. To some degree, this is a result of differing needs: So far, there are very few technical systems which come near a human being in terms of versatility. However, with new capabilities in manufacturing technology and materials science, interest in materials and structures that know their state or can react to their environment is growing. Aircraft and wind energy industry have already been named as examples highlighting the former, structural health monitoring aspect; robotics may in contrast serve as reference where interactive properties take the stress.

In all the above-mentioned applications, an increasing quantity of data is to be handled, and handled in limited time. Possible solutions to this problem involve the use of artificial intelligence methods in analysis and interpretation of data as well as decision making. Besides, limiting the number of sensors while maintaining a high sensor density where needed is an option, leading to an optimisation problem with parameters like accuracy of reconstruction and robustness of the system as major

criteria [Jed09]. No matter which way is chosen, adequate simulation techniques are a necessity, and adequate means techniques which cover the whole range of the system's capabilities, starting from its response to external loads, the sensor signals effected by these loads, and moving on to covering the interpretation of these signals and the reaction strategies derived. Such a simulation technique is currently not available. The state of the art addresses the different fields separately, using tools like finite element analysis at the one and multiagent based simulation techniques at the other end of the spectrum, with the prediction of sensor signals as another, major step in between these [Ben00, Rob06].

Using these observations as a starting point, the following text presents approaches towards new simulation techniques that address the needs identified above. Besides, some effects expected from their use and the introduction of sensorial materials on structural design and application are highlighted. The relation to biomaterials is manifold. As has already been shown, technical systems with multitudes of highly integrated sensors and peripheral systems are mimicking biomaterials. If they are to be realised, it is reasonable to assume that engineering can learn from nature about how to use a nervous system efficiently. Besides, there are applications in medical engineering in which technical structures have to replace biological ones – as implants, for example. And finally, since simulation techniques are at the heart of the present study, techniques that incorporate the features discussed here may help human body modelling in being able to reflect, besides structural characteristics of materials, the likely reactions to certain situations – such as crash tests, for the simulation of which active human body models are already being developed.

2 – Structural Analysis, Materials Science and System identification

In structural analysis, we are used to defining a model of the technical system we intend to study, provide the loads we anticipate to act on it, and calculate the system response. If the former are forces, the latter will be displacements. The method of choice is Finite Element Analysis, a general method for numerically approximating partial differential equations with boundary conditions. The calculated results are exact, but only for the model we defined in the first place. This model includes more or less well-founded assumptions about suitable descriptions of material behaviour, boundary conditions, mathematical representation of the response on element level, fineness of the representation or mesh, etc.

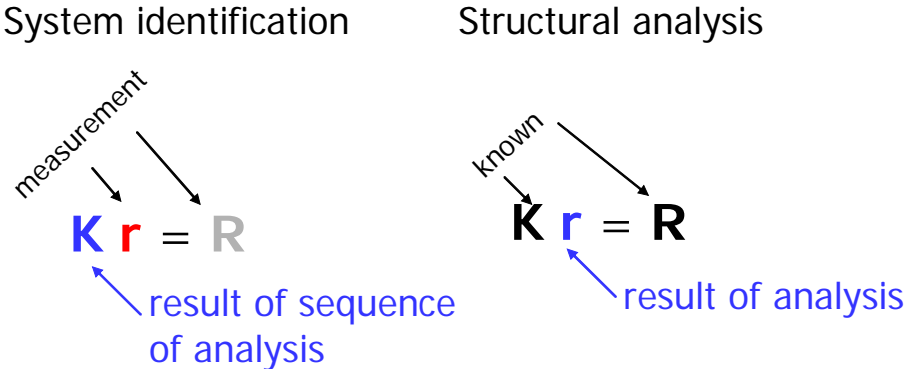


Fig. 1: Comparison between the system identification and the structural analysis approach.

Materials science supplies part of this model in the form of material laws, which in the present example define the fundamental relationship between load and response on the material level – in the classical case of structural analysis, stress and strain. In practice, we define a test setup, apply a load and measure the response using sensors e. g. to record displacement or strain. This basic procedure is used on different levels. Component tests are usually employed to confirm or validate the models and parameters originally selected for the structural analysis. For characterisation of materials, and thus effectively parameter determination for the material laws, the test conditions are deliberately chosen to yield a response as unambiguous as possible to clearly defined, preferably simple loads.

The latter case already follows the system identification approach, which is distinguished by a change in perspective (see figure 1): Loads and the related system response are measured with the aim to derive a general description of the system’s behaviour - a model - from a set of discrete load cases, this set being necessarily limited in cardinality.

Cardinality, or the number of test cases, is not the only limitation in this kind of system identification, though: A second one is granularity, since evaluation of materials data usually involves a very limited number of sensors (in a tensile test, often enough just one), with all the implications this has for the accuracy of the conclusions derived. This problem occurs again on the level of component testing, where sensor equipment defines the points for which conformity between model and physical component can be established.

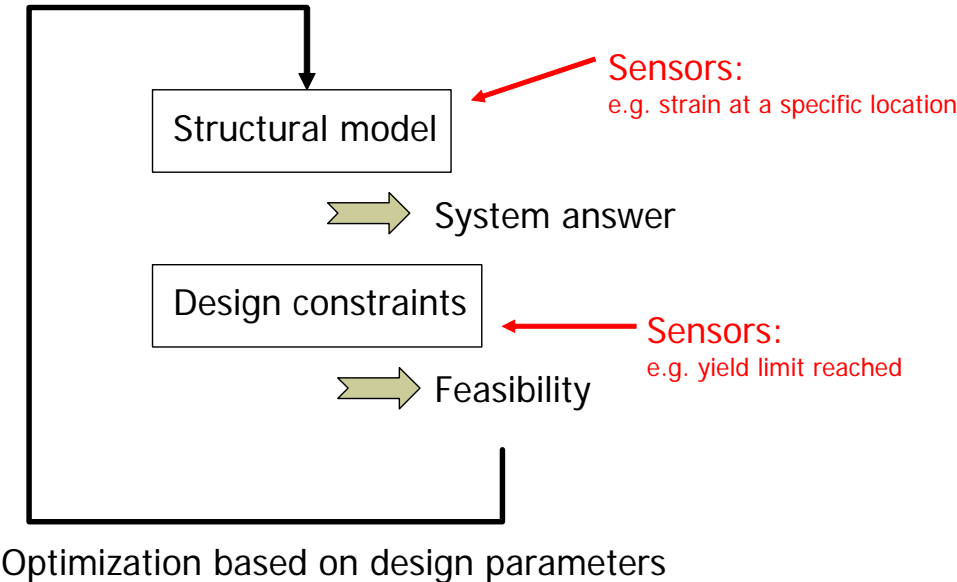


Fig. 2: Comparison between the system identification and the structural analysis approach.

Given this procedure, structural design starts with a set of requirements and design constraints, translates them into a first solution, which is put to the test virtually in the form of a structural model. From this, a system answer to specific load cases is gained and cross-checked against the design constraints that apply. Any violation discovered thus will afford an optimisation step. The design loads, however, are

arbitrarily chosen, and any supporting test campaign will rely on predefined conditions, to which the limited amount of information to be gathered from discrete sensors adds (see figure 2). The result is the already-mentioned system identification problem.

3 – Simulating Complex Interaction and Decision Making using Multiagent Systems

In contrast to FEM, Multiagent-based Simulation or MABS is object- instead of equation-based [Par98]. It is implemented in the form of individual agents, which model entities that make up the system under investigation. The aim, as in simulation in general, is to create a model as imitation of a system's behaviour and structure, and by using this model to generate new findings on the system's characteristics which can be transferred back to reality. In MABS, though, system behaviour emerges from local interactions of the agents (see figure 3). The method as such is known through application e.g. in social sciences, but has potential far beyond this [Dav00, Kir06, Tim06].

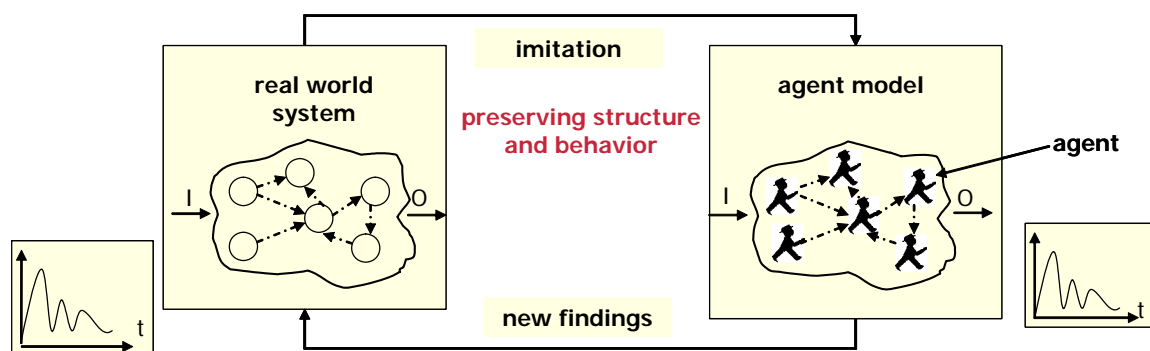


Fig. 3: Schematic sketch of the principle of Multiagent-based simulation.

The internal complexity of the individual agents varies very much. For many applications the 'simple reflex agent' architecture is sufficient, i.e., an agent which reacts directly and deterministically, given a particular, typically hard-coded input pattern. The mapping from sensorial input to the agent's actions is defined by a finite set of stimulus-response rules. This kind of agent architecture has no means for reasoning, nor does it involve any explicit knowledge base that goes beyond the above-mentioned stimulus-response patterns. As a consequence, the simple reflex agent is not well-suited for context-sensitive self-adaptation or even learning. Although the individual simple reflex agents seems to be trivial, the interaction of many of them in a multiagent system might result in the emergence of structure and behaviour close to what we usually consider to be typical only for complex biological and social systems. Well known examples of emerging complex behaviour in systems of very simple agents come from 'Swarm Intelligence' research: The so-called 'Ant Colony Optimisation' (ACO) algorithm is such an example. The individual agents in this scenario reduce to a pheromone sensor and the ability to recognize food as such. The actions are Move-to-a-target (e.g., some source of food), Return-to-home, Mark-the-path-you-take-with-a-pheromone-trail. Although a single agent

(the individual ant) doesn't have any explicit internal representation of what a path to a source of food is and how they are assessed according to their length, this simple algorithm converges to a good approximation of shortest-path search in graphs. Finding the shortest path in a graph is also the formulation of a very general optimisation problem with many practical applications, where 'shortest' means 'best' relative to some domain-dependent utility function.

The other extreme in the broad spectrum of proposed agent architectures is the very popular Belief-Desire-Intention (BDI) architecture. This architecture is motivated by certain assumptions about human cognition. A BDI agent has an explicit knowledge base (the 'beliefs'). Some initial 'background knowledge', the incoming sensorial input during the agent's runtime as well as information provided by other agents can become part of this knowledge base. Usually it is assumed that the agent's knowledge base is consistent and that the agent has some ability to draw inferences from his beliefs. The agent's desires can be thought of as his basic long-term needs or goals. The desires of an agent are not necessarily consistent, i.e., he might have conflicting goals (e.g., "good health" and "smoking cigarettes" at the same time). His intentions are states which enable an agent to achieve his desires. The intentions, finally, are rather short or medium term, as opposed to the long-term desires, and have to be consistent in order to enable rational decision making and planning.

Whatever agent architecture is chosen in a particular application, another important choice is the appropriate agent interaction protocol. Inter-agent communication can be based on the FIPA (Foundation for Intelligent Physical Agents) standard. This standard includes the specification of the FIPA version of the Agent Communication Language (ACL) and several protocols, e.g. contract net and many auction protocols [Fip02a, Fip02b, Schu08]. ACL messages include the speech act theory-inspired performatives (e.g., "inform"), but do not specify the semantics of the message content. The content semantics is often given by an external ontological representation.

4 – Best of both Worlds: Integrating MAS and FEM Approaches

When considering the new concept of sensorial materials, the two disparate aspects of structural characteristics and processing of information need to come together. Effectively, this can be achieved by integrating the major two approaches used in simulation of structural performance and information processing.

Naturally, availability of modelling and simulation techniques of this kind will affect knowledge of and design with novel sensorial materials: When studying sensorial materials, their built-in measuring capability can also be made use of during testing, providing a near-continuous rather than discrete answer of reactions of the system. Sensors would detect locally any overloading of the material, where overloading could stand for strain level exceeding the yield point, or a predefined number of load cycles reached, depending on the respective requirement profile and accordingly the type of sensors used. For the design process, and for component lifetime, this could mean that instead of doing the design work once and performing tests following predefined intervals or based on special events during usage, the material could control itself. Effectively this is again the basic idea of the sensorial material when used in structural applications: The concept of structural health monitoring with

individual sensors usually applied externally is advanced to the material level. The material in turn is then built up of a combination of structural subsystems and sensors, to which loads can be arbitrarily applied.

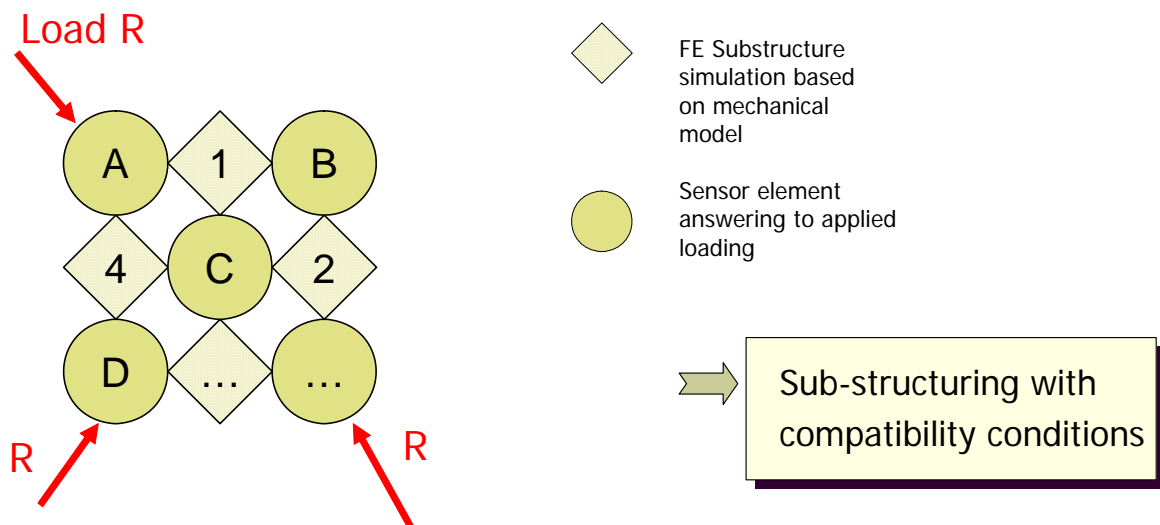


Fig. 4: A system of structural subsystems and sensors to which loads can be arbitrarily applied.

As promising approach to simulate such a structure, we propose a multiagent system where the structural subsystem agents have behavioural knowledge based on FE simulations. This system should then be able to deduce from the combination of sensor information and structural subsystem response the loads applied as well as any violation of design rules (see figure 4). Instead of having been designed to loads and tested to conditions, the system, and, in its physical realisation, this material or structure, can *experience* and *report* design constraint violations.

- Imagine a finite element model in which groups of elements, or, at higher granularity, even each individual element, is at the same time an agent in the MAS sense.
- Each of these agents has specific structural knowledge derived from validated structural models.
- Assume then further sensors described as material agents which represent the material law of a specific element.
- Each of these agents responding to any load applied by giving a direct answer based on the agents' original knowledge.
- Imagine now a load R applied to the structure: The displacements r will then be negotiated between the agents based on their knowledge of the element or group of elements they are associated with.

We will thus combine two modelling methods, one function-based (ontology), the other physics-based (FEM). For the structure of the agent based system verification we suggest an approach as given in fig. 5.

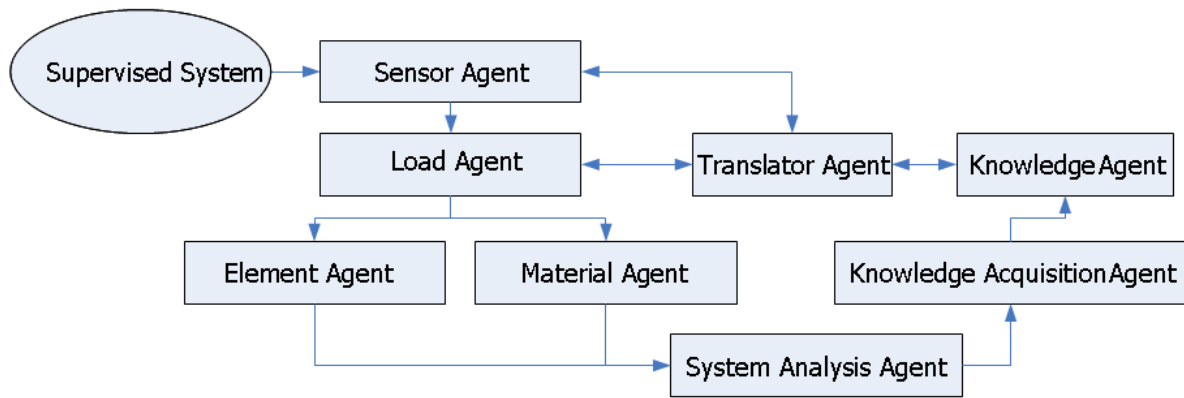


Fig. 5: Structure of the agent based system verification system

The ontology provides a standard vocabulary and a technical terminology as well as a domain model for knowledge integration. It can thus meet the requirements of information integration and information sharing [Dor05, Lan06]. For a selected design constraint the knowledge acquisition requires a conceptualization that has to be implemented and can be reused for the evaluation of the respective design constraint. We thus transfer the design process to a post-processing of the finite element analysis. The domain ontology will have three layers for the different agents with their information sources: (1) the ontology representation with the ontology browser, (2) the exchange layer with the annotation and implementation and (3) the reasoning with the similarity calculation and the ontology learning.

Steps towards the above system are being realised in a research project entitled “Functional Mockup”, which forms part of a research initiative at Bremen University to progress in the field of smart and specifically sensorial materials.

The primary aim of this project is to allow simulation of such materials on micro as well as macro level with respect to the materials functional properties, using MABS as basic technology. This research work is to be one building block of the envisaged overall system joining MAS and FEM. Until then, the project will provide capabilities in

- simulation and modelling of functional and qualitative properties of sensorial materials
- semantic interpretation of sensor data
- modelling of relations between sensors and actuators
- representing interaction and communication of sensors

5 – Conclusion and Outlook

Simulation techniques as described here are a prerequisite for an efficient implementation of what we call “sensorisation”, i. e. to equip technical structures with an analogue of a nervous system by providing a network of sensors, communication facilities linking these and specific hardware as well as computational methods to derive meaning from their combined signals. For “sensorial materials” in the sense introduced here, this need is even more urgent, not the least since it will facilitate representation of the high granularity envisaged for these materials.

Besides usage as a design and analysis tool, we expect from the realisation of the system we have outlined new findings regarding the emergence phenomenon in such materials. We are confident such a system would help to analyse and improve robustness of engineering structures, both from the point of view of information processing and structural properties, and we see a potential to help determine the levels of sensor density as well as optimum sensor locations needed to reach certain targets with respect to redundancy and accuracy: It is obvious that for practical purposes, as many sensors as possible cannot be the answer to this question [Jed09].

For these reasons, we intend to actively promote further research efforts in this field.

6 – References

- [Ben00] Benjeddou, A.: Advances in piezoelectric finite element modelling of adaptive structural elements: A survey. *Computers and Structures*, 76(1–3):347–363.
- [Dav00] Davidsson, P.: Multi Agent Based Simulation: Beyond Social Simulation. In S. Moss and P. Davidsson (eds.): *Proceedings of the Workshop on Multiagent-Based Simulation (MABS 2000)*, Lecture Notes in Artificial Intelligence, Vol. 1979, pp. 97–107. Springer, 2000.
- [Dor05] D. Dori, M. Shpitalni, Mapping Knowledge about Product Lifecycle Engineering for Ontology Construction via Object-Process Methodology. *Annals of the CIRP*, 54 (1): 117–120, 2005.
- [Fip02a] *FIPA Abstract Architecture Specification*. Document Nr.: SC00001L. Internet: <http://www.fipa.org/specs/fipa00001/>. 2002.
- [Fip02b] *FIPA ACL Message Structure Specification*. Document Nr.: SC00061G. Internet: <http://www.fipa.org/specs/fipa00061/>. 2002.
- [Jed09] Jedermann, R.; Lang, W.: The minimum number of sensors - Interpolation of spatial temperature profiles. In: Rödiger, U.; Sreenan, C.J.,(eds.): *Wireless Sensor Networks*, 6th European Conference, EWSN 2009, Lecture Notes in Computer Science (LNCS), Berlin/Heidelberg, Springer, 2009, Vol. 5432, pp. 232-246. (doi: 10.1007/978-3-642-00224-3_15)
- [Kir06] Kirn, S.; Herzog, O.; Lockemann, P. and Spaniol, O. (eds.): *Multiagent Engineering: Theory and Applications in Enterprises*. Springer, 2006.
- [Lan06] Langer, H.; Gehrke, J. D.; Hammer, J.; Lorenz, M.; Timm, I. J. and Herzog, O.: A Framework for Distributed Knowledge Management in Autonomous Logistic Processes. *International Journal of Knowledge-based and Intelligent Engineering Systems*, 10 (4): 277–290.
- [Par98] Parunak, H. V. D.; Savit, R. and Riolo, R. L.: Agent-Based Modeling vs. Equation-Based Modeling: A Case Study and User's Guide. In Sichman, J. S.; Conte, R. and Gilbert, N. (eds.): *Multi-Agent Systems and Agent-Based Simulation, First International Workshop (MABS '98)*, Lecture Notes in Computer Science, Vol. 1534, pp. 10–25. Springer, 1998.
- [Rob06] Robaldo, A.; Carrera, E. and Benjeddou, A.: A unified formulation for finite element analysis of piezoelectric adaptive plates. *Computers and Structures*, 84 (22-23):1494–1505.
- [Tim06] Timm, I. J.; Scholz, T. and Herzog, O: Emerging Capabilities in Intelligent Agents for Flexible Production Control. *Advanced Engineering Informatics Journal*, 20(3):247–295, 2006.
- [Schu08] Schuldt, A.; Gehrke, J. D. and Werner, S.: Designing a Simulation Middleware for FIPA Multiagent Systems. In *2008 IEEE/WIC/ACM International Conference on Web Intelligence and Intelligent Agent Technology*, Sydney, Australia, Dec. 9-12, 2008, pp. 109–113.

CHARACTERIZATION OF AORTIC TISSUE FRACTURE TOUGHNESS AND STIFFNESS UNDER CYCLIC FATIGUE LOADING

Boby Chu (1), Rosaire Mongrain (1), Jean-Claude Tardif (2)

(1) Department of Mechanical Engineering, McGill University, Montreal, Quebec, Canada

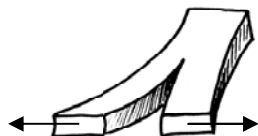
(2) Montreal Heart Institute, Montreal, Quebec, Canada

INTRODUCTION

An aortic aneurysm is the abnormal bulging of the aorta brought upon by the weakening of the aortic wall. Some known causes of aneurysms include genetic conditions such as Marfan syndrome [1], and vascular diseases like atherosclerosis [2]. While aneurysm ruptures can be lethal, prophylactic surgical intervention usually in the form of a aortic resection is not risk free [3] and should be used only when rupture is imminent. Unfortunately, there is no accurate method of assessing rupture risk currently available to clinicians [4]. There is therefore a need to better understanding the mechanics of aneurysm rupture in order to predict such event.

The microstructure of aortic tissue plays a significant role in tissue integrity. Because the aorta evolves in a pressurized pulsatile environment, it is under constant cyclic fatigue loading which affects its microstructure through, among other mechanisms, damage accumulation. The latter will have adverse effects on tissue integrity and should be reflected by variations in the tissue's mechanical properties. In this work, two properties of interest are the tissue's fracture toughness and its elasticity.

When examined from a fracture mechanics perspective, aneurysm rupture can be viewed as a Mode I fracture (Figure 1) of the aortic tissue. A material's resistance to fracture is its toughness, the energy required to produce a unit area of crack, a concept first proposed by Griffith



ire

[5]. From this energy-based viewpoint, the pathological tissue is viewed as a wall with flaw-like microscopic cracks and voids that grow in quantity and size with cyclical loading. At a given instant, these flaws can quickly expand catastrophically once a threshold level of mural strain energy has been surpassed, thus leading to an aneurysm rupture. Coupled with the notion of fatigue, the fracture mechanics approach is advantageous as it may be possible to exploit the inherent notion of time to account for material fatigue induced by the pulsating nature of aortic environment, thus offering the possibility for better characterization and prediction of the risk of rupture.

However, because fracture toughness is difficult to measure in vivo, as destructive testing of a given tissue sample is often required. Fortunately, the same damage accumulation mechanism that alters fracture toughness should also modify other mechanical properties, including elasticity. The latter benefits from its ability to be assessed by benign methods such as transesophageal tissue echography [6].

While elastic properties of both porcine and human aortic tissues [7-10] and toughness of porcine aortas [11] have been examined separately, no attempt has been made to quantify the relationship between them.

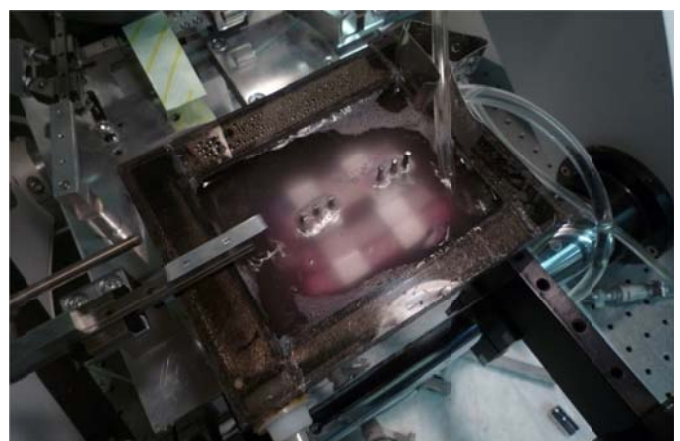
This current work involves the tensile megacycle loading of aortic tissue excised from porcine ascending aortas. At varying intervals, the elastic and fracture toughness properties of the samples will be measured by biaxial extension and guillotine testing, respectively. The results will help establish and quantify the relationship between the tissue's stiffness, fracture toughness, and fatigue life.

MATERIALS AND METHODS

A custom guillotine fracture toughness testing attachment was built and attached to a Bose/EnduraTEC ElectroForce (ELF) 3200 2-axis test apparatus configured for simple uniaxial testing. The guillotine attachment design consists mainly of a razor blade mounted solidly on the testing arm of the test apparatus. The tissue sample of interest is fixed on a stainless steel slotted base mounted on the machine's table and instrumented to capture the force applied to the sample. As the ELF 3200's arm advances, the blade cuts through the test sample and into the slot. Displacement of the arm and the applied force are recorded by the Wintest software supplied by the tester's manufacturer.

Porcine ascending aortas were harvested from a local slaughterhouse. Two rings 1-cm in width are cut from each ascending aorta and their circumference recorded. The rings are then opened on the medial quadrant (corresponding to the inner curvature of the aorta) to measure their opening angles. One strip is kept in a refrigerated Krebs solution both and serves as the control specimen. The other is attached to a custom-built, temperature-controlled fatigue apparatus (Figure 2) that stretches the strip's lateral section (corresponding to the outer curvature of the aorta) by a stretch ratio $\lambda_{\theta\theta}$ of 1.15. All fatigue cycling is done at 37°C with the sample immersed in aerated Krebs solution.

Figure 2. Fatigue apparatus with samples loaded

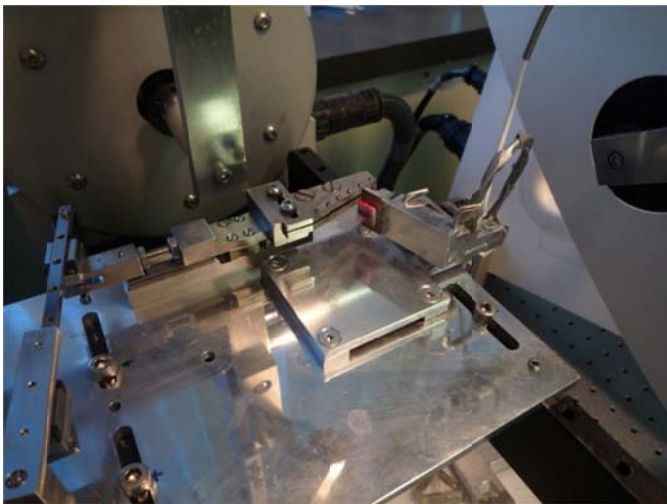


When a desired number of fatigue cycles are complete, a 1 cm × 1 cm square is extracted from each strip. This tissue square corresponds to the lateral section of the original ring. Each tissue

square is biaxially tested. The samples are attached to the movers of the biaxial testing machine using sutures. The movers are equiaxially displaced by 8 mm. Each sample is preconditioned via 9 loading and unloading cycles at 0.4 mm/s, with 3 more subsequent cycles at 0.1 mm/s counting as test runs. All tests were conducted at room temperature (about 20°C to 22°C) with the samples immersed in Krebs solution.

Once the biaxial testing complete, each square sample is loaded onto the aforementioned fracture toughness tester (Figure 3). The sample is mounted so that the circumferential direction is parallel to the blade. When the sample is cut through completely at the end of the test, the area of the freshly cut surface is measured. The sample's toughness is the work required to cut the sample over the area of the cut. All samples are processed within 36 hours of acquisition from the slaughterhouse. All samples were stored at around 4°C when not being tested, and none of the samples were ever frozen.

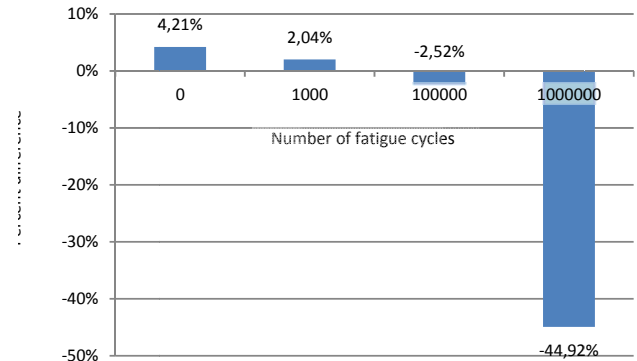
Figure 3. Guillotine attachment with sample attached



PRELIMINARY RESULTS

The experimental component of this work is currently still in progress. Only a limited number of samples were available and tested as of the date of this publication. However, a trend appears to be forming in the preliminary fracture toughness data. The variation in the fracture toughness between the control sample and the fatigue sample of a same ascending aorta seems to show a negative correlation with the number of stretching cycles (Graph 1). This can possibly be attributed with the cumulative damage incurred during fatigue loading. The 4.21% difference at 0-cycle shows the regional variation in mechanical properties in the aorta, particularly as the location of the samples approaches the aortic arch. Regional variations have been noted previously [11] and demonstrate the need to establish a good 0-cycle baseline for comparison purposes. The immediate future will see the number of test specimens increased and the arrival of the first elasticity measurements results correlated with the number of fatigue loading cycles. It is hoped that by integrating concepts of fracture mechanics and the data obtained from this work into existing models [9, 12-14], one can potentially develop an accurate clinically-applicable tool for assessing the risk of aneurismal rupture.

Graph 1. Variation of fracture toughness between control and fatigued samples with varying number of fatigue cycles



REFERENCES

- [1] Gott, V. L., Cameron, D. E., Alejo, D. E., Greene, P. S., Shake, J. G., Caparelli, D. J., and Dietz, H. C., 2002, "Aortic root replacement in 271 Marfan patients: a 24-year experience," *The Annals of thoracic surgery*, 73(2), pp. 438-443.
- [2] Chan, W. L., Pejnovic, N., Hamilton, H., Liew, T. V., Popadic, D., Poggi, A., and Khan, S. M., 2005, "Atherosclerotic abdominal aortic aneurysm and the interaction between autologous human plaque-derived vascular smooth muscle cells, type 1 NKT, and helper T cells," *Circ Res*, 96(6), pp. 675-683.
- [3] Stringfellow, M. M., Lawrence, P. F., and Stringfellow, R. G., 1987, "The Influence of Aorta Aneurysm Geometry Upon Stress in the Aneurysm Wall," *Journal of Surgical Research*, 42(4), pp. 425-433.
- [4] Vorp, D. A., 2007, "Biomechanics of abdominal aortic aneurysm," *Journal of Biomechanics*, 40(9), pp. 1887-1902.
- [5] Griffith, A. A., 1921, "The phenomenon of rupture and flow in solids," *Philosophical Transactions, Royal Society of London, A* 221, p. 25.
- [6] Vitarelli, A., Conde, Y., Cimino, E., D'Angeli, I., D'Orazio, S., Stellato, S., Padella, V., and Caranci, F., 2006, "Aortic wall mechanics in the Marfan syndrome assessed by transesophageal tissue Doppler echocardiography," *Am J Cardiol*, 97(4), pp. 571-577.
- [7] Raghavan, M. L., Webster, M. W., and Vorp, D. A., 1996, "Ex vivo biomechanical behavior of abdominal aortic aneurysm: Assessment using a new mathematical model," *Annals of Biomedical Engineering*, 24(5), pp. 573-582.
- [8] Vorp, D. A., Raghavan, M. L., Muluk, S. C., Makaroun, M. S., Steed, D. L., Shapiro, R., and Webster, M. W., 1996, "Wall strength and stiffness of aneurysmal and nonaneurysmal abdominal aorta," *Abdominal Aortic Aneurysm: Genetics, Pathophysiology, and Molecular Biology*, 800, pp. 274-276.
- [9] Vande Geest, J. P., Sacks, M. S., and Vorp, D. A., 2006, "The effects of aneurysm on the biaxial mechanical behavior of human abdominal aorta," *Journal of Biomechanics*, 39(7), pp. 1324-1334.
- [10] Choudhury, N., Bouchot, O., Rouleau, L., Tremblay, D., Cartier, R., Butany, J., Mongrain, R., and Leask, R. L., 2008, "Local mechanical and structural properties of healthy and diseased human ascending aorta tissue," *Cardiovasc Pathol*.
- [11] Purslow, P. P., 1983, "Positional Variations in Fracture-Toughness, Stiffness and Strength of Descending Thoracic Pig Aorta," *Journal of Biomechanics*, 16(11), pp. 947-953.

- [12] Wang, D. H. J., Makaroun, M. S., Webster, M. W., and Vorp, D. A., 2002, "Effect of intraluminal thrombus on wall stress in patient-specific models of abdominal aortic aneurysm," *Journal of Vascular Surgery*, 36(3), pp. 598-604.
- [13] Vande Geest, J. P., Bohra, A., Sun, W., Di Martino, E., Sacks, M. S., and Vorp, D. A., 2004, "Development and 3D Finite Element Implementation of a Multiaxial Constitutive Relation for Abdominal Aortic Aneurysms," ASME International Mechanical Engineering Conference Anaheim, California.
- [14] Raghavan, M. L., and Vorp, D. A., 2000, "Toward a biomechanical tool to evaluate rupture potential of abdominal aortic aneurysm: identification of a finite strain constitutive model and evaluation of its applicability," *Journal of Biomechanics*, 33(4), pp. 475-482.
- [15] Pape, L. A., Tsai, T. T., Isselbacher, E. M., Oh, J. K., O'Gara, P. T., Evangelista, A., Fattori, R., Meinhardt, G., Trimarchi, S., Bossone, E., Suzuki, T., Cooper, J. V., Froehlich, J. B., Nienaber, C. A., Eagle, K. A., and Investigators, I., 2007, "Aortic diameter ≥ 5.5 cm is not a good predictor of type A aortic dissection - Observations from the international registry of acute aortic dissection (IRAD)," *Circulation*, 116(10), pp. 1120-1127.



SimBio-M

Simulation for Bio- Mechanics, Materials, Medicine, Molecules

Session 1A

Biomechanics Biomaterials

Mr. Massimiliano Avalle

Politecnico di Torino,
Italy
massimiliano.avalle@polito.it



“Mechanical modelling of biopolymer materials”

Alessandro Scattina, Marco Peroni, Massimiliano Avalle, Lorenzo Peroni

Keywords: Biopolymers, pedestrian safety

Summary:

Plastics are materials with the higher rate of exploitation in engineering. Plastics are obtained from oil, a non renewable resource with, probably, very limited reserves. Although the well known, and undoubt, problem of CO₂ increase is only slightly related to the polymer synthesis, great interest is growing about new “green” polymers from organic sources. Moreover, the use of plant based raw material does not create ethical problems since only a little fraction (<<5%) of oil is used for plastics. The interest in biopolymers, obtained from organic matter, is related to the unavoidable increase in oil prices. Among bio-plastics PLA, obtained from corn bio-masses through fermentation with bacteria, is one of the most known and interesting. It has properties similar to polystyrene and it can be used in packaging as a replacement of PS and PET. Applications in the biomedical area are already well documented, whereas there are only some experiments in automotive, for interior parts. Possible and longed for applications are for exterior car parts for weight reduction. To use any material for car body parts, it is necessary to have detailed information on its behaviour, physical, thermal, mechanical, etc.

Knowledge of the mechanical properties is fundamental for the design of vehicle structures. One of the more demanding function is crash performance, which involves high strain and strainrate and failure. All these behaviours have to be modelled in structural simulations. This work presents some results about modelling a biopolymer with future applications in automotive components, taking into account strain-rate and temperature. In particular both creep and the influence of strain-rate are modelled in a unified way. Usually these two behaviours are studied separately. However, creep and strain-rate are two different aspects of the same physical behaviour (viscoplasticity) evaluated at two different time scales. The work starts from a large number of experimental tests obtained under different loading conditions, with different temperatures and strain rates by means of both dynamic loading (short time) and creep tests (long time) Based on experimental data, different analytical models, are studied obtaining a good correlation between the experiments and the numerical models.



Session 1A

Biomechanics Biomaterials

Mr. Andreas Burbliès

Fraunhofer IFAM,
Germany
bur@ifam.fraunhofer.de

“Cancellous Bone – Computational Bone Remodelling and Manufacturing”

Andreas Burbliès, Natalia Reichert, Liciane Sabadin, Bertol Sonja Larm

Keywords:

Bone, remodelling, computing

Summary:

Mechanical loads affect cancellous bone structure by bone mineralisation processes. This kind of self optimisation which produces maximum stiffness is called “bone remodelling”. The healthy bone performs the remodelling process without loss of mass. Multi Phase Topology Optimisation (MPTO) - a numerical structure optimisation method developed by Fraunhofer IFAM - is based on finite element method and determines the optimal spatial distribution of a given number of different materials for a mechanically loaded part. MPTO keeps mass and material composition constant, so it is useful to simulate bone remodelling processes. It has been applied in two and three dimensions to functionally graded porosity of human femur and mandible cancellous bone under several biomechanical conditions. Effects of multiple load cases are discussed. The femur case study validates Wolff’s law with trabecular bone structure. The mandible case study has been used to generate three dimensional virtual cancellous bone structures of the lower jaw with different trabecular architectures, e.g. tetrahedral or hexahedral topology. The computed microstructure of the whole mandible could be manufactured at Fraunhofer IFAM by Selective Laser Melting (SLM). Future applications will be in the area of medical implants.



Session 1A

Biomechanics Biomaterials

Mr. Eric Wagnac
(for Miss Anais Garo)
Ecole Polytechnique de Montreal
Canada
eric.wagnac@polymtl.ca



“An inverse finite element method to estimate the bone mechanical properties of the vertebral body”

A. Garo, P. J. Arnoux, E. Wagnac, C. E. Aubin

Keywords: Bone, dynamic properties, finite element model, vertebra

Summary:

Objectives : Finite element models of the spine can help improve our knowledge on the mechanism of burst fracture. However, little is known about the mechanical properties of bone tissue in dynamic loadings. The objective of this study was to evaluate the mechanical properties of cortical and trabecular bone in static and dynamic conditions.

Methods : A finite element model of a L5 vertebral body based on a CT-scan was created and tested in compression at two different velocities (10 and 2500mm/s). Ultimate strain and stress were optimized using a Central Composite Design until the failure load (FL) and energy absorbed at failure (EaF) reached experimental results from the literature. Mechanical properties were then derived from these strains and stresses. **Results :** For both velocities, the failure load of the vertebra was greatly influenced by the ultimate stress of the trabecular bone. The ultimate stress of trabecular bone and the ultimate strain of cortical bone were the most important factors for the EaF. The mechanical properties obtained were influenced by the displacement rate. The ultimate stress of trabecular bone was higher at high displacement rates (6.25 vs 2.6MPa), as well as its ultimate strain (10 vs 8%). For the cortical bone, the ultimate stress was higher (190 vs 140MPa) and the ultimate strain was lower (7.1 vs 8%) at high displacement rate.

Conclusion : This study presented an inverse finite element method to evaluate the mechanical properties of bone components of the vertebral body at two loading rates. The primary results showed the importance to adapt these properties according to strain rates. The integration of the strain rate in the material law of bone is currently under investigation. Further explorations will be to integrate these results into a more detailed model of the spine and study the burst fracture mechanism.



Session 1A

Biomechanics Biomaterials

Mr. Enda Minnock

Cranfield University,
UK

e.b.minnock@cranfield.ac.uk



“Simulating the Passage of Ultrasound Through the Phalanx”

Enda Minnock (a), Peter Zioupos (a), Keith Winwood (b), Lars Mulder (c)

a Biomechanics Lab, DASSR, Cranfield University, Swindon, UK

b Dept of Exercise & Sport Science, Alsager Campus, Manchester Metropolitan University, UK

c Dept of Biomedical Engineering, Eindhoven University of Technology, 5600 MB Eindhoven, The Netherlands

Keywords: Quantitative Ultrasound (QUS), Osteoporosis, Wave2000

Summary:

The goal of the work was to determine the ability of Quantitative Ultrasound (QUS) at the finger to predict overall skeletal condition.

Many attempts have been made to relate QUS parameters to measurements such as Bone Mineral Density (BMD). But few authors have looked at how the geometry and density of the region of interest actually affect the received waveform. We believe that understanding how these affect the passage of ultrasound will help in determining better, more appropriate, parameters. For example, changes in cortical area or density that could be predicted using surrogate measurements might allow clinicians to monitor the progress of osteoporosis.

CT images of the proximal phalanges of volunteers were collected. Using these images and density values, the geometry and the acoustic properties were determined and simulations were carried out using the Wave2000 package. This allowed for visualisation of the passage of ultrasound and the collection of the simulated received waveform. The waveforms allowed for the calculation of various ultrasound parameters including velocity and energy measurements. These variables could also be related to the CT parameters, such as cortical area and cortical density.

Initial results suggest that certain parameters can be used to predict the cortical area. This fact could prove very useful given that cortical area decreases with the progress of osteoporosis as a result of endocortical thinning. Also, this suggests that simple, inexpensive, repeat QUS measurements over a number of years may record the rate of bone loss, or bone thinning, for an individual. We also wish to compare the QUS from the finger with BMD measured at the clinically relevant sites including the lumbar spine and the proximal hip. In conclusion, these simulations have helped in understanding the ultrasonic pathways across the finger and how this affects the received waveform.



Session 1B

Biomechanics and Physiology

Dr. Hippolite Amadi

Imperial College London
UK

hippolite.amadi00@imperial.ac.uk



“A Joint Coordinate System for the simulation of the functional kinematics of the glenohumeral joint”

Dr Hippolite Amadi Dr Anthony MJ Bull

Keywords: JCS, Glenohumeral, shoulder, window, sequenceindependent

Summary:

Introduction: The functional anatomy of the glenohumeral joint (GHJ) is complicated and does not easily allow the application of Grood and Suntay's (1983) joint coordinate system (JCS) (Wu et al, 2005). A JCS at the GHJ is however necessary for the simplification of its complex kinematics to allow accurate simulation of the functions of its attaching soft tissues during joint motion. **Methods:** A square window guide that bounded the mobile humerus was devised to implement a JCS at the GHJ. This was such that the long axis of the humerus (h_x) and the lateral axis of the scapula (sz) parented a normal unit vector (f) to the window plane. However, the square window that trailed the mobile humerus was bounded by h_x and an orthogonalised axis (sz -orth) produced as a cross product of h_x and the plane normal, f . The axis, sz -orth, updates after every implementation of a motion component of a humeral position. Abduction/anterior translation, flexion/lateral translation and rotation/compression were implemented upon f , sz -orth and h_x respectively. This was applied in a step-wise decomposition of an acquired humeral motion along its 6 degrees of freedom to extract its quantifications of the JCS variables. This technique was numerically applied to physiological kinematics data from the literature to convert them to JCS and to visually reconstruct the motion on a set of GHJ bones for validation. **Results:** Reconstructions achieved the same results irrespective of the sequence of motion implementation and there was no manifestation of gimbal-lock effect. **Significance:** This application would enhance accurate simulation of GHJ physiological motion and the study of the attaching soft tissues to improve understanding, diagnoses and treatment of the associated diseases.



Session 1B

Biomechanics and Physiology

Mr. David Oreilly

Centre for Applied Biomedical Engineering
Research
university of Limerick,
UK
david.oreilly@ul.ie



“Finding forces at the hip joint resulting from everyday activities”

David O'Reilly, Maurice Donoghue, Tim McGloughlin, Michael Walsh

Keywords: Aseptic Loosening, Motion Analysis, Musculoskeletal modeling, Hip Forces.

Summary:

Aseptic loosening is seen as the most important cause of late failure after total hip replacement surgery and it is believed that hip joint forces on the hip prosthesis from movements such as stair climbing, and even walking, over a long time can lead to the loosening of the prosthesis. Motion analysis was carried out using 6 inferred cameras and 15 markers placed on the subject using the Helen Hayes Marker Set. The data was recorded and processed using EVaRT 5.0 (Santa Rosa, CA, USA). The marker positions were then used as the motion input for models created in LifeMod (San Clemente, CA, USA), a musculo-skeletal modelling software. Results were found for forces at the hip joint and at the ground where the foot hits the floor. Moments were found in the sagittal, coronal and transverse planes. Although there were slight differences in the forces for all 4 subjects there was very little difference between the moments for all the subjects. Only 4 subjects have been tested so more subjects, both healthy and hip replacement subjects, are needed to get a better understanding of the differences in hip forces.



Session 1B

Biomechanics and Physiology

Mr. Shuping Li

Center of Motor Control and Evolution,
Hubei University,
China
dli349@gmail.com



“Jockeys posture characteristics on the simulation horse”

Li Shuping (a), Zhu Weiming(a), Li Lin(a), Tao Jiang(a), Chan L.C(b), John Graham(b), Luk Tze Chung(c), Chu Pak Keung(d)

(a)Center of Motor Control and Evolution, Hubei University, Wuhan, China

(b)The Hong Kong Jockey Club, Hong Kong

(c)Hong Kong Baptist University

(d)Hong Kong Sports Institute

Keywords: posture

Summary:

Harmony has been used to describe the quality of horse – rider coordination, not only in horse race and equestrian but also in rehabilitation and recreation. This study was to explore jockeys posture characteristics on a mechanical horse with simulation race speeds.

One professional and eight apprentice jockeys postures with jockey's style on the mechanical horse under three race speeds were filmed. Jockeys performances were measured by a JVC camera with 100 fps. The three speeds of the mechanical horse for each jockey were given randomly so that the results didn't be affected by the muscle fatigue. Kinematical parameters of represent points' of jockeys based on the mechanical horse movements were analyzed by means of APAS software.

The professional showed jockey high body height (hip joint center: 93.5 cm) and large variance (23.1 cm). The apprentice jockeys presented other three different style: high body height (94.8 cm) and small variance (8.4 cm), low body height (61.4 cm) and large variance (20.6 cm), as well as low body height (69.2 cm) and small variance (9.2 cm). It was showed that the professional jockey presented a good rhythmic with the mechanical horse motion under all three speeds. While, the most apprentice jockeys didn't present a good rhythmic, such as phase delay, amplitude unstable within one speed as well as among three different speeds.

The results indicated that the vertical amplitude and rhythmic of jockeys on mechanical horse could be valuable index to evaluate the jockeys control ability.



Session 1B

Biomechanics and Physiology

Prof. David Howard

School of Computing, Science and Engineering
University of Salford
UK
d.howard@salford.ac.uk



“Predictive Modelling of Human Walking Over a Complete Gait Cycle”

Lei Ren², Richard K Jones (a) and David Howard (b)

(a)University of Salford,
(b)Kings College

Keywords: gait prediction, inverse dynamics, optimisation, optimal motor task

Summary:

The most popular approach to gait prediction has been to combine optimisation with forward dynamics. However, since the system differential equations must be numerically integrated, the forward dynamics method leads to very long simulation times. In addition, realistic initial guesses for all control inputs (e.g. muscle activations) and initial values for all state variables (e.g. joint angular positions and velocities) are required to ensure that reasonable gait patterns can be obtained. This depends on the availability of measurement data and compromises the capability of this approach as a predictive modelling tool.

In contrast, the inverse dynamics method is very efficient computationally as it does not require numerical integration of the system differential equations. In addition, initial values for optimisation parameters can be set without the need for measurement data and initial values for the state variables are unnecessary.

In this paper, we present a combined inverse dynamics and optimisation method to predict normal human walking. In contrast to previous studies, the model predicts a complete gait cycle, including a normal double support phase. The foot segment is allowed to rotate freely during stance, rather than remaining flat on the floor. In addition, no predefined or measured trajectory constraints are imposed on segmental motions. The gait motions and joint torques are predicted from only three simple gait descriptors, average walking speed, cycle period and double stance duration, which minimizes the requirements for experimental data.

Quantitative comparisons of the model predictions with gait measurements show that the model reproduced the significant characteristics of normal gait in the sagittal plane. The simulation results suggest that minimising energy expenditure is a primary control objective in normal walking. However, there is also some evidence for the existence of multiple concurrent performance objectives.

Hybrid numerical methods for estimating muscle forces

Pauline GERUS, Guillaume RAO, André JACQUES & Eric BERTON

Institut des Sciences du Mouvement E.J. Marey, UMR6233 Aix-Marseille Université, France

Introduction

Simulations of musculoskeletal system, as a complement of experimental studies, provide a way to estimate important variables that are difficult to measure experimentally (Delp et al., 2007). For example, a finite element (FE) analysis could be used to compute the internal loading of musculoskeletal system during human movement. The estimation of in-vivo joint contact forces from a FE model is highly challenging because their values may depend on factors such as joint geometry and material properties (Besier et al., 2008). Moreover, human movement is achieved via muscle forces acting on body segment they attach. These forces influence peak and distribution of joint cartilage stress (Besier et al., 2005), thus, being an important factor to account for during FE analysis.

However, the muscular redundancy (the number of muscles exceeding the degrees of freedom at a joint) makes difficult the assessment of the contribution of each muscle to the net joint moment (the sum of all the muscular actions around a joint). EMG-driven models were developed (Buchanan et al., 2004) to estimate muscle forces combining the physiological and mechanical properties of the muscle-tendon complex using all the available peripheral data (EMG, force plate, and kinematics). These models take into account physiological and mechanical factors influencing the magnitude of the forces developed by the muscle-tendon complex such as the muscle level of activation, the muscle force production capacity (depending on size, length, and lengthening velocity), the geometry of the muscle-tendon complex, and the mechanical properties of the tendon.

Few studies investigated the influence of muscle forces on joint stress during human movement despite their obvious influence. The aim of this paper was to describe EMG-driven models in order to propose methods to estimate joint stress during human movement. The muscle forces estimated during a human movement should be fed into a FE model in order to estimate realistic in-vivo joint contact forces.

EMG-driven models

The EMG-driven models used to estimate the muscle or muscle group forces rely on experimental data (kinematics, electromyography, ground reaction), anatomical parameters

(muscle fiber lengths, tendon moment arms), and numerical optimization process in order to adapt the initial EMG-driven model to the subject. Depending on the joint of concern, the complexity of the musculoskeletal model used to estimate the muscle forces could be adapted. As an example, the ankle joint could be represented with a single muscle group for the plantar flexion (muscle group including the gastrocnemius lateralis, medialis, and soleus muscles) and a dorsiflexor muscle group (with a single muscle, the tibialis anterior) as these muscle group forces are transmitted to bones through a single tendon. Oppositely, the knee joint is more complex and requires the implementation of more detailed models.

The force exerted by the muscle fibers results from the muscle activation, the length of the fiber (force-length relationship: Gordon et al., 1966), and their lengthening velocity (force-velocity relationships: Schutte et al., 1993). Then fiber forces are transmitted to bones via tendinous tissues (tendon and aponeurosis). These tendinous tissues are not inextensible (Scott and Loeb, 1995) and present an elastic behavior characterized by a non-linear force-strain relationship (Zajac, 1989). This generic musculoskeletal model presented in the Figure 1 contains adjustable parameters aiming at taking into account the differences inherent to each individual. For different tasks, the model calibration step consists in tuning the adjustable model parameters. To reach this goal, a non-linear optimization routine minimizes the difference between the net joint moment estimated by the EMG-driven model and the one obtained from experimental data (inverse dynamics). Once the calibration process is achieved, the muscle forces can be estimated.

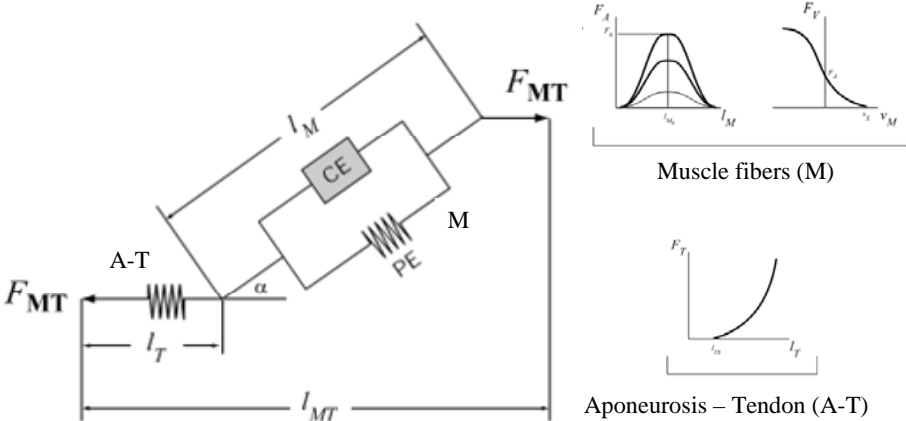


Figure 1: Representation of modified Hill-type muscle model including the geometric model of muscle-tendon complex and mechanical properties associated for each component. l_{MT} represents the length of muscle-tendon complex, l_T the length of aponeurosis-tendon et l_M the muscle fiber length.

The two previous EMG-driven models allow estimating the subject-specific muscle forces during dynamic conditions that can be used as input to a FE model in order to compute the in-vivo joint contact stress.

Conclusion

Researchers could use simulations using FE models to estimate “in-vivo” joint contact stress that are hard to measure experimentally. This model needs to take into account factors influencing the distribution and peak of joint stress. As a result, the muscle forces need to be used as input parameters. EMG-driven models were developed to estimate these muscle forces by combining peripheral data (EMG, dynamics, kinematics) and physiological and mechanical properties of muscle-tendon complex that affect the muscle force production.

The presence of muscular cocontraction (simultaneous contraction of the flexor and extensor muscle groups around a joint) could be used to stabilize a joint after injury. More specially, Doorenbosch and Harlaar (2003) showed that patients with an anterior cruciate ligament (ACL) deficiency increase the co-contraction level around the knee to increase active joint stabilization. From our thoughts, the increased cocontraction level should lead to higher “in-vivo” joint contact forces. These increased joint stress and joint stabilization have to be taken into account especially when studying situations where the joint stability is challenged (car crash, sport injuries...).

References

- BESIER, T. F., GOLD, G. E., BEAUPRÉ, G. S. and DELP, S. L. (2005). A modeling framework to estimate patellofemoral joint cartilage stress in vivo. *Med Sci Sports Exerc*, 37(11):1924–1930.
- BESIER, T. F., GOLD, G. E., DELP, S. L., FREDERICSON, M. and BEAUPRÉ, G. S. (2008). The influence of femoral internal and external rotation on cartilage stresses within the patellofemoral joint. *J Orthop Res*, 26(12):1627–1635.
- BUCHANAN, T. S., LLOYD, D. G., MANAL, K. and BESIER, T. F. (2004). Neuromusculoskeletal modeling : estimation of muscle forces and joint moments and movements from measurements of neural command. *J Appl Biomech*, 20(4):367–395.
- DELP, S. L., ANDERSON, F. C., ARNOLD, A. S., LOAN, P., HABIB, A., JOHN, C. T., GUENDELMAN, E. and THELEN, D. G. (2007). Opensim : open-source software to create and analyze dynamic simulations of movement. *IEEE Trans Biomed Eng*, 54(11):1940–1950.
- DOORENBOSCH, C. A. M. and HARLAAR, J. (2003). A clinically applicable emg-force model to quantify active stabilization of the knee after a lesion of the anterior cruciate ligament. *Clin Biomech (Bristol, Avon)*, 18(2):142–149.
- GORDON, A. M., HUXLEY, A. F. and JULIAN, F. J. (1966). The variation in isometric tension with sarcomere length in vertebrate muscle fibres. *J Physiol*, 184(1):170–192.
- SCHUTTE, L., RODGERS, M., ZAJAC, F. and GLASER, R. (1993). Improving the efficacy of electrical stimulation-induced leg cycle ergometry : an analysis based on a dynamic musculoskeletal model. *IEEE Trans. Rehab. Eng.*, 1(2):109–125.
- SCOTT, S. H. and LOEB, G. E. (1995). Mechanical properties of aponeurosis and tendon of the cat soleus muscle during whole-muscle isometric contractions. *J Morphol*, 224(1): 73–86.
- ZAJAC, F. E. (1989). Muscle and tendon : properties, models, scaling, and application to biomechanics and motor control. *Crit Rev Biomed Eng*, 17(4):359–411.

Windscreen material characterization for multibody simulation of pedestrian head impact

François Coulongeat¹, Robert W.G. Anderson², Alexandra D. Long², Thierry Serre¹

¹ Laboratoire de Biomécanique Appliquée, Institut National de Recherche sur les Transports et leur Sécurité, Université de la Méditerranée, FRANCE

² Centre for Automotive Safety Research, The University of Adelaide, AUSTRALIA

E-mail: francois.coulongeat@inrets.fr
robert@casr.adelaide.edu.au
alex@casr.adelaide.edu.au
thierry.serre@inrets.fr

ABSTRACT

Objective

A good knowledge of the contact properties between the windscreen and the head during an impact is necessary to obtain a reliable pedestrian-vehicle crash simulation. Contrary to other parts of the vehicle, windscreen may not only be bent but also cracked during an impact. The purpose of this study is to analyse the behaviour of a head impact on a windscreen and to design a numerical model of windscreen which account for rate-dependent damping effect.

Methods

Subsystem impact tests were used to measure the impact characteristics of the windscreen. Headform impactors were launched normal to windscreens at different velocities. Images from a very high speed video camera and acceleration data from the impactors were then recorded. The results of the subsystem tests were used to define contact-impact characteristics for the windscreen which correctly account for the damping effect. The characteristics were then implemented in a multibody model and the subsystem impact tests were simulated in order to validate it by comparison with experimental test.

Results

Two phases can be distinguished in the contact-impact characteristics. The first part corresponds to the bending and the fracture of the windscreen whereas the second part is associated to the bending of the windscreen once it is broken. The behaviour law of the windscreen has been implemented using a hysteresis model. The results from the numerical windscreen model are consistent with the results from the subsystem tests. Comparison of HIC values gives an additional validation of the consistency of our model.

Conclusions

The numerical model needs to be corroborated with more impact tests on a greater variety of windscreens. Particularly, we could check if the numerical model is always consistent for a very low or a very high impact velocity. It could also be interesting to consider the possibility to adapt the models in function of the impact location.

Keywords: Windscreen; Contact properties; Pedestrian-vehicle crash; Multibody simulation

NOMENCLATURE

F	Normal contact impact force
F_e	Elastic component of the contact-impact force
δ	Penetration
δ_p	Permanent indentation
$\dot{\delta}$	Penetration velocity
c	Hunt-Crossley damping parameter
K	Hertzian stiffness parameter
n	Hertzian stiffness index

INTRODUCTION

The objectives of simulations of collisions between pedestrians and motor vehicles include the reconstruction of actual crash [Serre *et al.* (2006a) ; Serre *et al.* (2006b) ; Van Rooij *et al.* (2003)] and the study of injury mechanism and influence of vehicle design on pedestrian injury [Glasson *et al.* (2000) ; Liu *et al.* (2002) ; Longhitano *et al.* (2005)]. A good knowledge of the contact properties between the pedestrian and the vehicle during impact is required to obtain a reliable simulation. Particularly, the contact between head of a pedestrian and a vehicle is critical to the estimation of head impact severity [Anderson *et al.* (2005)].

Description of a windscreen

A windscreen is basically constructed by placing an adhesive polymeric interlayer between two pieces of glass. The purpose of the interlayer is to prevent fragment of glass from being dispersed on impact thereby reducing the risk of injury caused by sharp piece of glass. In the case of small deformation, the elastic behaviour of the windscreen is determined by the glass, whereas for large deformations, the glass layers of the windscreen fail and the interlayer plays a dominant role because the brittle glass cannot withstand large strains [Timmel *et al.* (2007)]. There are two different fracture modes. Either the fracture begins after a short bending phase following the contact of the impactor on windscreen or a sudden fracture occurs after a long bending phase. Fracture behaviour is probably dependent on internal stress of the glass or micro scratches present on the windscreen surface, but fracture modes are not really predictable [International Organization of Motor Vehicle Manufacturers (2005)]. Characteristics of contact are also dependent on the location of the impact [Mizuno and Kajzer (2000)].

To our knowledge, no previous multibody model of contact on windscreen takes into account the rate-dependent damping effect.

Contact characteristics

Vehicle stiffness characteristics are indeed often based on experimental data in which energy loss is an important parameter. [Van Rooij *et al.* (2003)] incorporated experimentally this energy loss by examining force-deflection data and considering a fixed loading phase prior to an unloading phase with unloading completed at some finite permanent deformation. While such an approach may be successful when the simulated impact is under the same conditions than the impact test, there may be problems when it is not, due to a rate-dependent damping [Anderson *et al.* (2009)]. Thus, even if a multibody contact-impact model of the windscreen is based on experimental data e.g. [Mizuno and Kajzer (2000)] and is validated at the same

velocity e.g. [Van Rooij *et al.* (2003)], it may have other unintended properties under other impact conditions (i.e. different impact masses and speeds).

[Liu *et al.* (2002)] considered contact loading and unloading forces as linear stiffness functions of penetration. A hysteresis slope connects the loading curve at peak of displacement and unloading curve. While energy lost may be predicted thanks to this approach, it leads to unrealistic force-time data due to the inherent discontinuities in the contact definition [Anderson *et al.* (2009)].

Our study is based on the model of contact developed by [Anderson *et al.* (2009)]. This model is based on the [Hunt and Crossley (1975)] model, which includes a rate-dependent damping and is extended to include permanent indentation. After characterising subsystem impact test data on windscreen, according to the [Anderson *et al.* (2009)] method, we implemented the model of contact in a multibody model. We also analysed the behaviour of the windscreen during the impact. Contrary to other parts of the vehicle, windscreen may indeed not only be bent but also cracked.

METHODS

Subsystem tests

The contact interaction between head and windscreen was characterised thanks to subsystem tests on windscreen using headform impactors. The impact tests were undertaken at the Pedestrian Impact Laboratory at the Centre for Automotive Safety Research, Australia. The laboratory includes a free-flight headform launcher that is capable of propelling a headform of 4.8 kg at speeds up to 70 km/h. The headform impactors used for this study were conform to the specifications of [EEVC Working Group 17 (2002)]: an adult impactor which has a diameter of 165 mm and weighs 4.8 kg and a small adult impactor which has a diameter of 165 mm and weighs 3.5 kg. The impactors were launched normal to the windscreen. In this study the headforms include damped accelerometers in accordance with [JARI (2004)] recommendations, which is important as windscreen fracturing can cause the natural frequency of an undamped accelerometer to be excited, distorting the signal [Stammen *et al.* (2001)]. Velocity and penetration of the impactors are given by successive integrations of acceleration data. Newton's Second Law gives contact force from acceleration. Images from a very high speed video camera were also recorded in order to analyse the behaviour of the impactor during the impact.

Three subsystem tests were conducted on a Toyota Corolla near the lower windscreen frame and on a Renault Scenic near the centre of windscreen. One out of the five tests was conducted on the original windscreen and the others were conducted on new windscreens. A summary of the configuration of tests is given in Table 1.

Vehicle	Corolla			Scenic	
Test number	C1	C2	C3	S4	S5
Head mass (kg)	4.8	3.5	3.5	3.5	3.5
Location of impact	lower frame	lower frame	lower frame	centre	centre
Speed at contact (m/s)	8.45	11.05	9.87	7.58	9.8
Kinetic energy (J)	171.4	213.7	170.5	100.6	168.1
Windscreen state	new	new	new	old	new

Table 1 – Configuration of experimental tests

Data analysis

Feature times of the impact were picked out from curves and videos. Times of first and last fractures and rebound of impactor on windscreen were identified from video analysis. The beginning of the rebound of the impactor was identified from the velocity data.

The results of the impact tests were used to derive contact interaction models according to [Anderson *et al.* (2009)] method : the expression of normal contact force between the impactor and the windscreen is given by Eq.(1). This force arises from experimental data. It is a function of penetration velocity, elastic component and of a damping parameter.

$$F = F_e [1 + c\dot{\delta}] \quad (1)$$

Hunt-Crossley damping parameter c was empirically fixed to $0.15 \text{ m}^{-1}.\text{s}$ for all force-penetration characteristics according to [Anderson *et al.* (2009)] method. Dividing force data by $[1 + c\dot{\delta}]$ produced the F_e -penetration characteristics.

Implementation and validation of the model

Multibody model including the windscreen and the headform impactor was implemented with MADYMO multibody software [TNO Automotive (2001)]. The windscreen is modelled by a degree-4 ellipsoid and the headform impactor is modelled by a spherical ellipsoid which has the same dimension than the adult headform impactor (external diameter equal to 165 mm).

A model of characteristic is designed in order to fit to the experimental data F_e -penetration. This model of characteristic and the Hunt-Crossley damping parameter are then implemented in the model of contact between the impactor and the windscreen. The model is validated by simulating the experimental subsystem tests under the same conditions and comparing the results of numerical simulations with the result of experimental tests.

Of particular interest was the estimated values of the Head Injury Criterion (HIC) [Versace (1971)] which is used to represent head injury risk. A good numerical model of contact between a head and a windscreen should give a consistent value of HIC. Thus, we compared values of HIC from experimental tests and from numerical simulations. The HIC is calculated using head acceleration with a CFC1000 filter according to the SAE J211/1 standard [Society of Automotive Engineers (1995)].

RESULTS

Video and acceleration data analysis

Two phases of acceleration followed by a complete deceleration can be distinguished in each of the acceleration-time characteristics (Figure 1). The first is relatively tight and can involve possible sudden decreases of acceleration. The second phase is larger. In the scenic case, an intermediate phase in which acceleration is null appears.

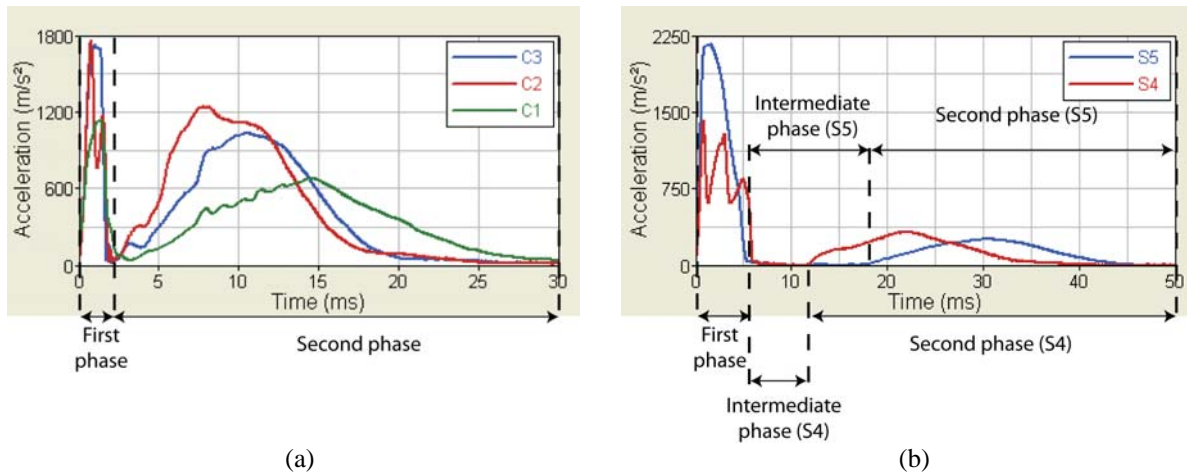


Figure 1 – Acceleration-time characteristics from Corolla (a) and Scenic (b) experimental tests

Regarding the Scenic windscreen tests, a sudden fracture is apparent on the video of the tests after a bending phase in the experimental test S5 whereas the fracture begins after a very short bending phase following the contact of the impactor in the other test, S4. Regarding all of the Corolla windscreen tests C1, C2 and C3, the fracture begins after a very short bending phase following the contact of the impactor. Table 2 summarizes the feature times of experimental tests from videos and acceleration data. Times to fracture noticed on videos correspond to the first sudden decreases of acceleration in acceleration-time data (Figure 2 and Figure 3).

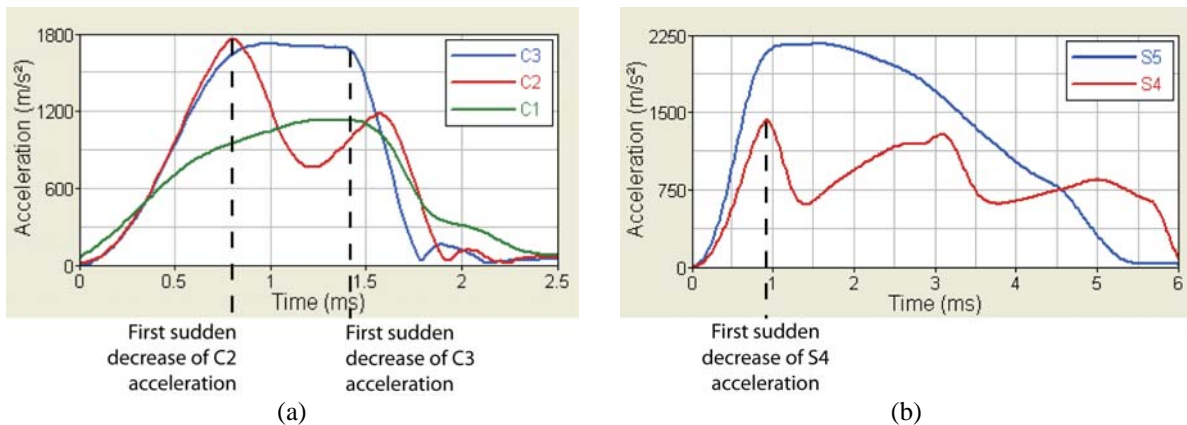


Figure 2 – First phase of acceleration-time characteristics from Corolla (a) and Scenic (b) experimental tests

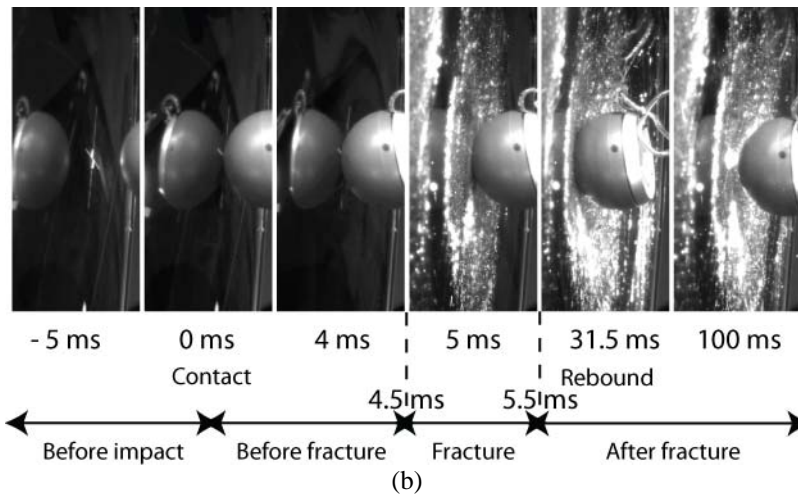
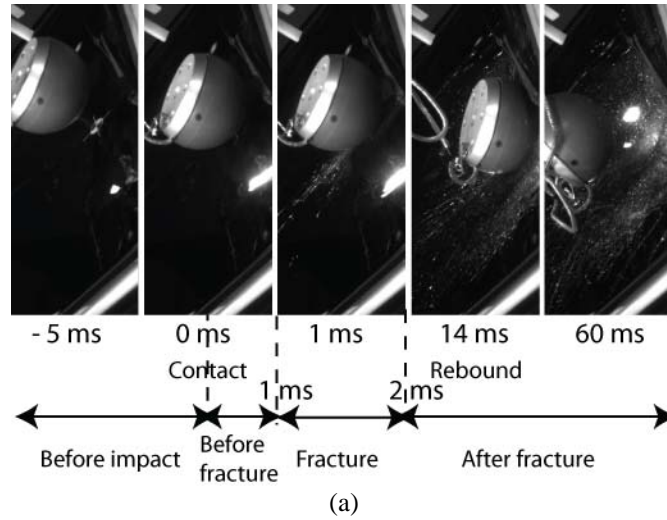


Figure 3 – Videos of experimental tests C3 with a very short bending phase before fracture (a) and S5 with a longer bending phase before fracture (b)

Test number	C1	C2	C3	S4	S5
First fracture (from video)	2	< 1	1	< 1	4.5
First sudden decrease of acceleration	*	0.8	1.4	0.9	*
Last fracture (from video)	3	2	2	6	5.5
End of first phase of acceleration data	2.5	2.25	2.2	6.1	5.5
Rebound (from video)	17	13	14	23	31.5
Rebound (from curves)	18.5	13.3	14.1	23.7	32.2

Table 2 – Feature times of experimental tests (in ms)

*: no real sudden decrease

Force-penetration characteristics

Figure 4 gives force-penetration characteristics from experimental tests. Dividing the force data by $[1 + c\dot{\delta}]$ produced the F_e -penetration characteristics shown in Figure 5 for a value of c

equal to $0.15 \text{ m}^{-1}\text{s}$. The three characteristics from experimental tests on Corolla are then similar but both of the characteristics from experimental tests on Scenic are dissimilar. Particularly, energy absorption corresponding to the area under the curve is really different in both of the scenic experimental tests.

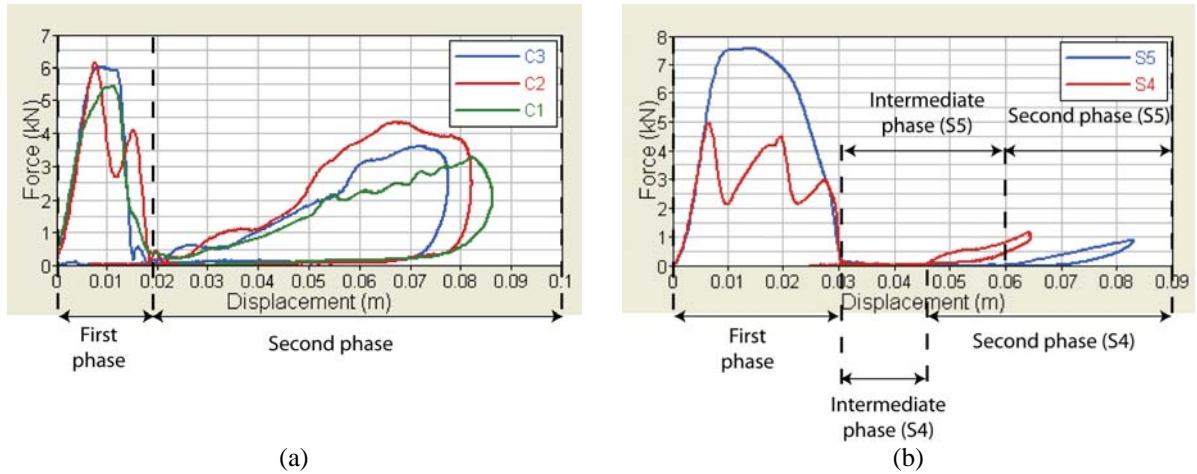


Figure 4 – Force-displacement characteristics from Corolla (a) and Scenic (b) experimental tests

Similarly to acceleration-time characteristics, two parts can be distinguished in each of the force-penetration characteristics. The first part corresponds to a loading phase followed by a complete unload with possible vertical sawtooth. The second part is a hysteresis curve with permanent deformation. In the scenic case, an intermediate part in which penetration increases whereas force is null appears.

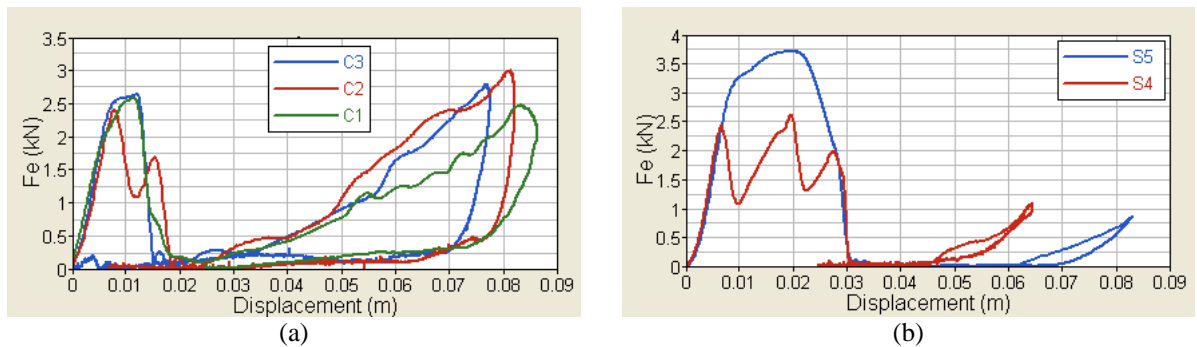


Figure 5 – Fe-displacement characteristics from Corolla (a) and Scenic (b) experimental tests

Implementation and validation of the model

A model of F_e -penetration characteristic was designed in order to fit to experimental data. Considering the similarities of the curves, a single model of characteristic was designed for the Corolla windscreen. On the other hand, two models of characteristic were designed for the Scenic windscreen corresponding to an old and a new windscreen.

The first part of the characteristic is modelled as a sine curve of which the area under the curve is equal to the area under the first part of the experimental curve in order to have the same dissipated energy. The loading and unloading phases of the hysteresis part of the curve are modelled under the form given by the Eq. (2). A hysteresis slope of the form given by the Eq. (3) is used to connect the loading curve at peak displacement with the unloading curve.

$$F_e = K(\delta - \delta_p)^n \quad (2)$$

$$F_e = K\delta \quad (3)$$

Subsystem tests were then simulated under the same conditions. Figure 6 shows the comparison between force-penetration characteristics from experimental tests and numerical simulations.

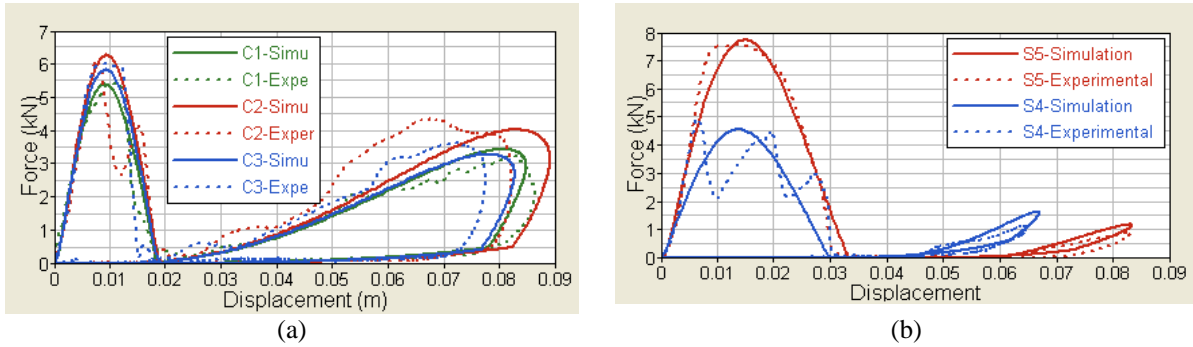


Figure 6 –Comparison of characteristics between experimental tests and numerical simulations from Corolla (a) and Scenic (b)

Table 3 gives a comparison between HIC values from experimental tests and numerical simulations.

Test number	C1	C2	C3	S4	S5
HIC from experimental data	270	953	647	410	1348
HIC from simulation	359	922	597	417	1586
Relative error	33 %	3%	8%	2%	18%

Table 3 – HIC value from experimental data and simulations

DISCUSSION

Impact behaviour

According to the feature times of experimental tests (Table 2), the first part of the contact characteristics corresponds to the bending of the windscreen from the beginning of contact up to the spreading of the fracture. Behaviour of windscreen is then probably determined by the glass, in conformity with [Timmel *et al.* (2007)]. The second part of the characteristics corresponds to the bending of windscreen once glass is broken. Interlayer plays then probably a dominant role in the behaviour of windscreen, in accordance with [Timmel *et al.* (2007)]. In the Scenic case, intermediate phase corresponds to a lack of contact between impactor and windscreen.

Tests on the Scenic and Corolla cannot be compared due to the different location of impact [Mizuno and Kajzer (2000)]. In the Scenic case, behaviour of fracture is really different between both of the tests. Windscreen state (new or old) seems to play a role on fracture mode in accordance with previous observations [International Organization of Motor Vehicle Manufacturers (2005)]. On the other hand weight of impactor does not seem to play a major role on behaviour.

Consistency of numerical models

Numerical models provide characteristics consistent with result from experiments, both in terms of local maximum and penetration. However, both of the models of Scenic windscreen are each based on only one test. As a consequence, more experimental tests are required in order to be able to validate these models.

HIC values from numerical simulations C2, C3 and S4 are close to values from respective experimental tests. Even if HIC values from numerical simulations C1 and S5 are less close to values from respective experimental tests, values are consistent and orders of magnitude are similar. Consequently, conclusions on head injuries are not biased in numerical simulations. Comparison of HIC values gives then an additional validation of the consistency of our model.

Study limits

Even if the numerical models seem to be consistent, they need to be corroborated with more experimental tests. We can indeed wonder if these numerical models are always consistent for lower and higher impact velocity. Particularly, what is the behaviour of impact with at very low velocity without a fracture? In the same way, is the second part of force-penetration characteristics (hysteresis) always consistent at very high velocity?

It could also be interesting to consider the possibility to adapt the models with the location of impact thanks to the results of [Mizuno and Kajzer (2000)].

CONCLUSION

This paper also confirms and completes behaviour analysis from the literature [*International Organization of Motor Vehicle Manufacturers (2005) ; Timmel et al. (2007)*]. Particularly, we noticed that the behaviour of a new windscreen differs from the behaviour of an old one. We also distinguished two main phases on force-displacement characteristics which respectively correspond to the glass and the interlayer mechanic behaviour.

Previous studies have dealt with modelling of impact on windscreen or explained fracture behaviour [*Flocker and Dharani (1997) ; International Organization of Motor Vehicle Manufacturers (2005) ; Mizuno and Kajzer (2000) ; Timmel et al. (2007)*]. Even if our multibody models of impact need additional validation with more experimental data, it takes into account for the rate-dependent damping effect and gives consistent results.

REFERENCES

- Anderson R.W.G., Long, A.D., Serre, T. (2009). "Phenomenological continuous contact–impact modelling for multibody simulations of pedestrian–vehicle contact interactions based on experimental data." *Nonlinear Dynamics (online)*.
- Anderson R.W.G., McLean, J., Dokko, Y. (2005). Determining accurate contact definitions in multi-body simulations for DOE-type reconstruction of head impacts in pedestrian accidents. 19th International Technical Conference on the Enhanced Safety of Vehicles. Washington, National Highway Traffic Safety Administration.
- EEVC Working Group 17 (2002). Report Improved Test Methods to Evaluate Pedestrian Protection Afforded by Passenger Cars.
- Flocker F., Dharani, L. (1997). "Modelling fracture in laminated architectural glass subject to low velocity impact." *Journal of Materials Science* **32**(10): 2587-2594.

- Glasson E., Basile, F., Cavallero, C., Bonnoit, J. (2000). A numerical analysis of the car front end module regarding pedestrian lower limb safety. London, England, Institution of Mechanical Engineers: 79-91.
- Hunt K., Crossley, F. (1975). "Coefficient of restitution interpreted as damping in vibroimpact." ASME Journal of Applied Mechanics **42**(2): 440-445.
- International Organization of Motor Vehicle Manufacturers (2005). Observation of different windscreen glass fracture modes during headform impactor tests. GTR Pedestrian Protection Informal Group Meeting. INF GR/PS/164., Geneva, Switzerland.
- JARI (2004). Generation of abnormal acceleration in headform impact test: causes and solutions. 7th Meeting INF GR / PS, Paris, France.
- Liu X.J., Yang, J.K., Lövsund, P. (2002). "A Study of Influences of Vehicle Speed and Front Structure on Pedestrian Impact Responses Using Mathematical Models." Traffic Injury Prevention **3**(1): 31 - 42.
- Longhitano D., Henary, B., Bhalla, K., Ivarsson, J., Crandall, J. (2005). "Influence of vehicle body type on pedestrian injury distribution." SAE transactions **114**(6): 2283-2288.
- Mizuno K., Kajzer, J. (2000). Head Injuries in Vehicle-pedestrian impact. SAE 2000 World Congress. Detroit, Michigan, SAE Technical Paper.
- Serre T., Masson, C., Perrin, C., Chalandon, S., Llari, M., Cavallero, C., Py, M., Cesari, D. (2006a). Pedestrian and Cyclist Accidents: A Comparative Study Using In-Depth Investigation, Multibody Simulation and Experimental Test. IRCOBI.
- Serre T., Masson, C., Perrin, C., Chalandon, S., Llari, M., Cavallero, C., Py, M., Cesari, D. (2006b). Real accidents involving vulnerable road users: in-depth investigation, numerical simulation and experimental reconstitution with PMHS. International Crashworthiness Conference.
- Society of Automotive Engineers (1995). Instrumentation for impact test. Part 1: Electronic instrumentation. **SAE J211/1**.
- Stammen J., Saul, R., Ko, B. (2001). Pedestrian head impact testing and PCDS reconstructions. 17th International Technical Conference on the Enhanced Safety of Vehicles (ESV).
- Timmel M., Kolling, S., Osterrieder, P., Du Bois, P. (2007). "A finite element model for impact simulation with laminated glass." International Journal of Impact Engineering **34**(8): 1465-1478.
- TNO Automotive (2001). Theory manual - Madymo V6.0.
- Van Rooij L., Bhalla, K., Meissner, M., Ivarsson, J., Crandall, J., Longhitano, D., Takahashi, Y., Dokko, Y., Kikuchi, Y. (2003). Pedestrian crash reconstruction using multi-body modeling with geometrically detailed, validated vehicle models and advanced pedestrian injury criteria 18th international conference on the Enhanced Safety of Vehicles (ESV).
- Versace J. (1971). A review of the severity index. 15th Stapp Car Crash Conference.



Session 2A

Biomedicine - Biomolecules

Mr Charles SAVOLDELLI

CHU Pasteur Nice + MINES ParisTech

CEMEF

France

csavoldelli@yahoo.fr



“Development of a Finite Element Model of the Temporomandibular Joint for Distraction Osteogenesis Studies”

Charles Savoldelli, Pierre-Olivier Bouchard, Yannick Tillier

Keywords: Finite Element model, Maxillofacial surgery, Distraction Osteoge

Summary:

Distraction osteogenesis is a surgical process used to reconstruct skeletal deformities and lengthen bones of the body. A corticotomy is used to fracture the bone into two segments, and the two bone ends of the bone are gradually moved apart during the distraction phase, allowing new bone to form in the gap. When the desired or possible length is reached, a consolidation phase follows in which the bone is allowed to keep healing. Distraction osteogenesis has the benefit of simultaneously increasing bone length and the volume of

surrounding soft tissues. Although distraction technology has been used mainly in the field of orthopedics, early results in humans indicated that the process can be applied in maxillofacial surgery to correct the majority of congenital craniofacial defects, as well as some facial injuries resulting from trauma. But it is much more difficult to accomplish in the face than in other areas of the body since bones must often be moved in three dimensions and small skeletal changes lead to large changes in the structure of the face.

Consequently it is of prime importance that bone movements be carefully planned before a device is

implanted, especially in the area of the temporomandibular joint which may be at the origin of chronic pain. This work aims at developing a full 3-D finite element software capable of simulating the entire process of maxillofacial distraction osteogenesis. It uses data from CT scans to create a segmented model of the patient's skull, and then computes stress and strain during and at the end of the distraction process.

FINITE ELEMENT SIMULATION OF HUMERAL INTRAMEDULLARY NAILING: CASE OF TORSION LOADING

Virginie ASTIER, Pierre-Jean ARNOUX, Lionel THOLLON, Frédéric MOURET, Christian BRUNET

Humeral shaft fractures are common injuries among various populations, from the young to the elderly. They account for approximately 3% of all fractures and 20% of humeral fractures (Christensen, 1967; Barsotti, 1990, Tytherleigh-Strong et al., 1998). These fractures occur under various loading situations, from sports trauma and traffic injuries to simple falls. For clinicians, humeral shaft fractures lead to certain complications. Non-union occurs in up to 10% of cases, radial nerve palsy occurs in 6 to 17% of cases and long-term impairment of the shoulder joint is frequent due to long periods of immobilization (Jupiter & van Deck, 1998; Templeman, 1998; Finkkila, 2004).

Also, severe fractures observed in high-speed traffic accidents require surgical management (Templeman, 1998).

Hence, to avoid rehabilitation complications or to manage severe injuries, surgical treatment is more largely used, although its efficiency (with 2 to 20% setbacks) is in question (Templeman, 1998).

Whatever the treatment, the rate of complications is globally the same, and the functional score and recovery time do not exhibit large differences. Intramedullary nailing is an intermediate solution. It is minimally invasive compared with other surgical interventions, with a mobilisation stage earlier than other treatments.

To investigate this fracture treatment, various biomechanical studies on mechanical tissue properties up to rehabilitation process were reported on. Experimental studies were performed in order to evaluate the torsion properties of the humerus, failure thresholds with and without nailing systems and local damages on the nail/bone interface.

To improve our understanding of the biomechanical properties of intact and fixed intramedullary humeral structures, numerical simulations can be useful tools to obtain data not available experimentally throughout the test chronology (from fracture simulation to healing process). With the objective of investigate nailing efficiency from a biomechanical viewpoint, the numerical simulation was used to investigate humerus torsional behaviour from intact bone structure to nailed humerus at various stage of the healing process.

Bone property and nail efficiency evaluations were obtained through the following three steps:

- Validation of the intact bone during a torsion test until the bone fracture.
- Simulation of reamed intramedullary nailing introduced by the antegrade approach and evaluation of the structural failure process.
- Evaluation of torsional mobilization of coupled bone implant structures for various stages of bone healing: haematoma, fibrous callus, woven bone and complete bone healing (mature bone).

To perform these tests, boundary conditions come from experimental studies: humerus is locked on one extremity and a constant torque is applied on the second extremity ($5^\circ/s$) (Schopfer et al., 1998).

Material properties for intact bone are reported in the following table:

		E (MPa)	ν	ρ (g/mm ³)	σ_y (MPa)	σ_{max} (MPa)	ϵ_{max} (%)	ϵ_{dam} (%)
Epiphysis (th 1-3 mm)	cortical	3500	0.3	0.6*10 ⁻³	71.5	83	2	
	spongious	250	0.4	0.1*10 ⁻³	3.6	5	1.5	1.5
Metaphysis (th 3-6 mm)	cortical	5000	0.3	0.6*10 ⁻³	100	115	3	
	spongious	350	0.3	0.1*10 ⁻³	5	7	1.61	1.5
Diaphysis	cortical	7700	0.3	0.6*10 ⁻³	110	135	4.5	

Table 1: *Mechanical properties of bone used for model definition (Astier et al., 2008)*
(with E: Young's modulus; ν : Poisson's ratio; σ_y : Failure plastic strain ; σ_{max} : Maximum stress;
 ϵ_{max} : Failure plastic strain ; ϵ_{dam} : critical strain value)

During healing process, materials properties of callus are modified (Christel et al., 1981):

	Approx. time	Callus thickness (mm)	Properties
1st: Haematoma	D+1	2	Weak properties
	D+6	2	
2nd: Fibrous callus	D+7 to 5 W	2	Improvement to 30% of intact values / high elasticity
3rd: Woven bone	> 6 W	3	Improvement to 70% of intact values
4th: Mature bone	>1 Y	3 to 5,5	100% of initial bone properties

Table 2: *Table of assumptions for the mechanical properties of callus during the healing process.(cart: cartilage; fib tissue: fibrous tissue)*

A typical standard nail was designed (comparable to those described in literature). This nail uses an anterograde implantation method after reaming, and is locked with screws (two proximal and one distal) to the bone structure

Picture 1 shows the test configuration.

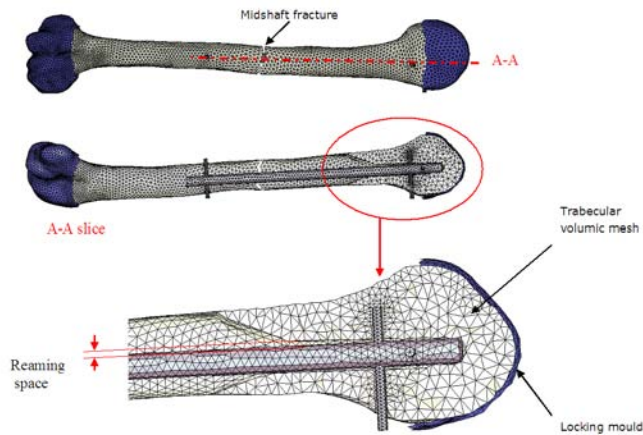


Figure 1: *Boundary conditions for nail insertion in the humerus model*

For the intact humerus, the evolution of the Von Mises stress distribution showed a spiroidal loading mode on the structure with the highest stress levels located on the proximal metaphysis (figure 2). Bone failure was observed for a torsion level of 22.53° with a torque curve in agreement with experimental results (Schopfer et al., 1998, Wan nar Wong et al, 2005, Strothman et al, 2000, Maher et al., 2007).

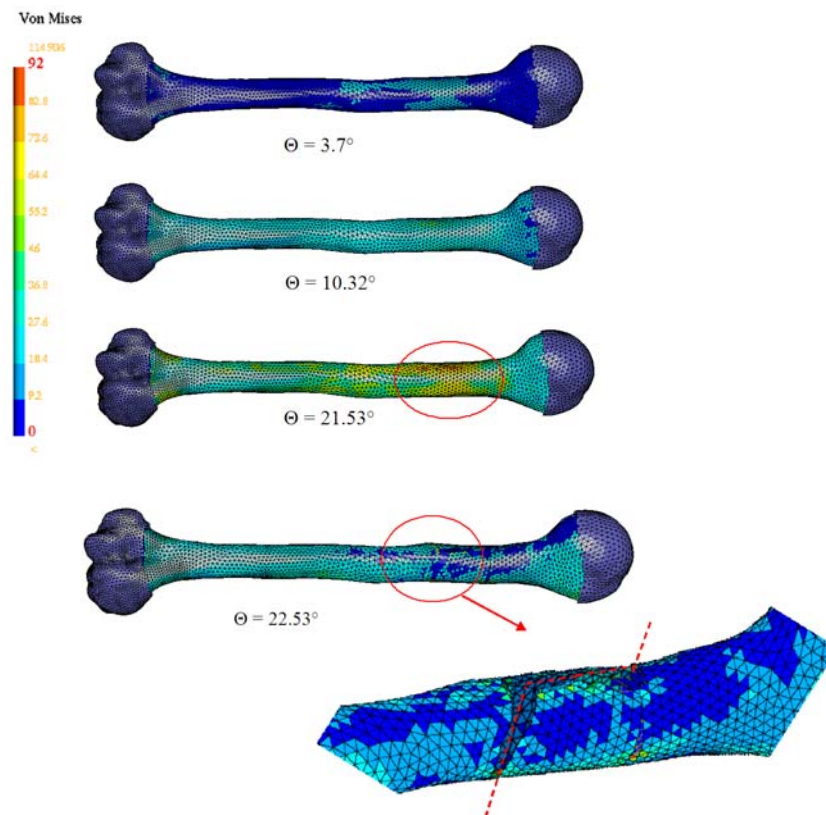


Figure 2: *Von Mises stress distribution on cortical bone during the torsion test*

In the case of implanted bone, load distribution is different because stresses were concentrated around the screws and led to damage and failure on the bone structures initiated on screw

insertion. Once the contact forces due to bone/screw interactions were fully active, the bone-implant system began to be recruited. Loads were then applied to the proximal bone structure through the nail component up to failure processes.

During healing process, the mechanical behaviour changes:

- For haematoma, failure was entirely located around the screws, as the previous test, with a few torque level;
- For fibrous callus, a failure on the callus component was associated with damage around screws (figure 3) for a torsion level more important.
- For the other two cases, the failure was located on the proximal third of the humerus, with a similar failure profile and type as those observed for intact bone. This injury is associated with damage around screws. The bone maturation seems to induce a more homogenous distribution of Von Mises stress in the overall bone structure. Additionally the torque level at failure is the same that those of intact bone.

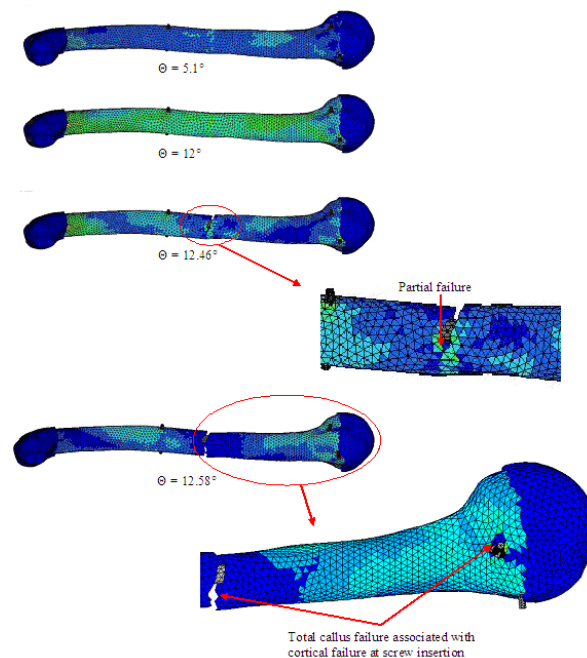


Figure 3: *Von Mises stress curve distribution and damage during the fibrous callus step*

Regarding the failure process and location, results are relevant with experimental and clinical data. The mechanical behaviour of bone/nail affects the fracture processes and the force distributions in the structure during bone rehabilitation with intramedullary nails.

The simulation demonstrated how screwing devices can have a strong influence on structural behaviour (with local damage) and consequently on the efficiency of the surgical technique.

The distribution of loads in the structure by the nail is different depending on the healing effects on callus, and this point could be used as an indicator of consolidation process efficiency:

- For the two first step of the healing process, due to the bending moment observed and the failure location on screws and callus (nail transmits loads but induce important damage), minimum mobility should be prescribed to the bone component.

- As soon as the callus recovers the majority of initial properties (for woven and mature bone), the torsion effect is mainly shared along the bone structure, that improves the torque at failure as for intact bone, complete structural mobilization could be allowed.

Taking model limitations into account, this study provides injury thresholds for humeral torsion depending on the stage of healing. It also suggests that structural mobilization should be promoted once the woven bone maturation process has started. Lastly, due to the risk of more severe failure with nailed structures, this study also suggests undertaking an investigation on evaluation of the potential effects of screw removal after complete restoration.

Bibliography

Astier, V., Thollon, L., Arnoux, P. J., Mouret, F. and Brunet, C., 2008, 'Development of a finite element model of the shoulder: application during a side impact', *International Journal of Crashworthiness*, 13:3, 301-312

Barsotti, J., and Dujardin, C., *Fractures de la diaphyse huméral, Guide pratique de traumatologie*, Masson, Paris (1990), p. 42

Christel, P., Cerf, G., Pilla, A., 1981, Time evolution of the mechanical properties of the callus of fresh fractures, *Annals of Biomedical Engineering*, Vol. 9, pp. 383-391.

Christensen, S., 1967, Humeral shaft fractures, operative and conservative treatment. *Acta Chir Scand.*; 133:455-460.

Flinkkilä, T., 2004, *Intramedullary nailing of humeral shaft fractures*, PhD thesis, University of Oulu, Finland, 2004

Jupiter, JB. & van Deck, M., 1998, Ununited humeral diaphysis. *J Shoulder Elbow Surg* 7: 644- 653

Maher, SA., Meyers, K., Borens, O., Suk, M., Grose, A., Wright, TM., Helfet, D., 2007, Biomechanical evaluation of an expandable nail for the fixation of midshaft fractures, *J Trauma*. 63(1):103-7.

Schopfer, A., Hearn, TC., Malisano, L., Powell, JN., Kellam, JF., 1994, Comparison of torsional strength of humeral intramedullary nailing: a cadaveric study, *J Orthop Trauma*. 8(5):414-21.

Strothman, D., Templeman, DC., Varecka, T., & Bechtold, J., 2000, Retrograde nailing of humeral shaft fractures: a biomechanical study of its effects on the strength of the distal humerus. *J Orthop Trauma* 14: 101–104.

Templeman, D., Schmidt, A., 2002, Management of humeral shaft fractures, <http://www.medscape.com/viewprogram/150>

Tytherleigh-Strong, G., Walls, N., McQueen, M., 1998, The epidemiology of humeral shaft fractures, *J Bone Joint Surg [Br]* ;80-B:249-53.

Wan Nar Wong, M., Hung Kei Chow, D., Chi Kei, L., 2005, Rotational stability of Seidel nail distal locking mechanism, *Injury, Int. J. Care Injured* 36, 1201—1205



Session 2A

Biomedicine - Biomolecules

Mr Dae Gon Woo

Yonsei University

Korea

dgwoo@cabe.yonsei.ac.kr

“Effect of Mandible Trabecular Bone Microstructure on Stress Distribution within Premolar Tooth and Dental Implant using micro-Finite Element Analysis”

Dae Gon Woo, Chang Soo Chon, Chi Hoon Kim, Ji Hyung Park, Dohyung Lim, Han Sung Kim

Keywords: Trabecular bone microstructure, Stress distribution, Premolar tooth, Dental implant, Finite element analysis

Summary:

The present study examined the effect of trabecular bone microstructure on stress distribution within a premolar tooth and a dental implant against mastication force by using finite element (FE) analysis. In the previous studies, trabecular bone was modeled with homogeneous material having low material properties because researchers had difficulty in describing the complex structure of the trabecular bone. However, these methods did not correlate well with the real trabecular bone and therefore there is a need for realistic models describing the detailed structure of the trabecular bone. In the present study, we considered various densities of trabecular bone microstructure on stress distribution within premolar tooth and implant. A mandibular specimen including a premolar was obtained from a cadaver (female, age 60) and scanned with high resolution microcomputed tomography (μ CT). Natural dental models reconstructed from μ CT images at the midsagittal plane of the tooth were converted into six different FE models to predict the mechanical stress/strain environment at the implant/bone interface. A commercial software (ANSYS, ANSYS Inc, USA) was used for FE analysis. The same load conditions and boundary conditions were enforced on all models. Stress distributions in each implant (or tooth) model were compared. The present study indicated that trabecular bone microstructure should be considered in FE analysis and implant design to produce reasonable results and thus long-term high success rates of dental implant surgery could be obtained.



Session 2A

Biomedicine - Biomolecules

Mr Tobias Heimann

Asclepios Project, INRIA Sophia Antipolis
France
tobias.heimann@inria.fr



“A Transversely Isotropic Hyperelastic Material for Real-Time FEM Simulations”

T. Heimann and H. Delingette

Keywords: Surgery Simulation, Finite Elements Method, Real-Time

Summary:

In the medical domain, training simulators which enable surgeons to practice interventions on virtual patients are receiving increasing attention. The finite elements method is a popular choice for modeling biological soft tissue, but due to the strict real-time requirement, the employed biomechanical models are often simplified.

In this paper, we present a real-time finite element model for fibrous biological materials as ligaments and tendons. The model includes anisotropy along the main fiber direction and non-linear stress-strain response as determined experimentally. In the constitutive equations, one invariant controls the incompressibility of the material, while all other invariants remain constant under pure volume changes. We derive stress and elasticity tensors for the special case of tetrahedral elements, exploiting the simple geometry for performance optimizations. A number of experiments on synthetic shapes shows the plausibility of the model and its advantages over isotropic and linear material models.

We aim to employ the presented model for ligaments of the knee joint and expect it to improve the accuracy in medical simulations, e.g. surgery trainers for knee ligament ruptures.

NOTCHING IN THE ANTERIOR FEMUR WITH USE OF FEMORAL STEM – FINITE ELEMENT STUDY

¹ Completo A., ¹Tavares N., ²Fonseca F., ¹Relvas C., ¹Ramos A¹., ¹Simões J¹.

¹University of Aveiro

²University of Coimbra

INTRODUCTION

The occurrence of distal femoral fracture after total knee arthroplasties (TKA) is approximately 1% with reported rates ranging from 0.3% to 2.5% [1]. Risk factors are osteopenia, osteoporosis, anterior femoral notching, chronic steroid therapy, rheumatoid arthritis, arthro-fibrosis, revision total knee arthroplasties and severe neurologic disorders [2,3]. Among the numerous factors associated with these fractures, osteopenia and femoral notching are implicated most often [2,3]. The prevalence of notching of the anterior femoral cortex in TKA has been reported to range from 3.5% to 26.9% [1,2,3]. Femoral notching occurs when a bone defect (notch) in the anterior femoral cortex occurs due to the bone cuts for the femoral component insertion. Excessive femoral component rotation in the antero-medial and antero-lateral can promote notching. Although some authors refer the significance of anterior femoral notching [4], stress concentrations created by anterior femoral cortex notching are of considerable importance because of possible association with supracondylar femur fractures when associated with osteopenia effects. In terms of biomechanical investigations, Lesh et al [4] used paired cadaveric femora to study full thickness cortical notches in the anterior distal femur. They found that notching significantly reduced the load to failure in both bending and torsional loading. Lesh et al [4] advocated that patients who sustain inadvertent notching should have additional protection at postoperative period, and consideration should be given to use of a femoral stem extension to bypass the stress-riser of the anterior notch. However, the use of prophylactic femoral stems intraoperatively is always more complex and expensive.

Within this study, a question concerning the structural aspects of the use of prophylactic femoral stems in cases of notching in the anterior femur was raised: What is the range of the notch size from which the use of a femoral stem can be useful for the reduction of fracture risk? We hypothesized that for small notch sizes the use of femoral stems does not decrease significantly the stress-raiser at the notch and the use of a prophylactic stem is unnecessary. In addition, we hypothesized that for largest notch size the use of femoral stem does not decrease enough the stress-raiser to prevent the risk of femur fracture and the use of a stem is ineffective. Thus, the aim of the present study was to determine the notching size for which the use of a prophylactic femoral stem is an advantage in the reduction of the risk of fracture. Finite element (FE) models were used in the study.

METHODS

Finite element models (Table_1) of the implanted femur were built from 3D models of 3rd generation of femur (left, mod. 3306 from Pacific Research Labs, Vashon Island, WA) made available in public domain (<http://biomech.me.unr.edu/hip.htm>). Femoral component and stem (125mm) of the P.F.C Sygma Modular Knee System (DePuy International, Inc) were replicated in these models. The implants surface models were created with a CAD modelling package (Catia, Dassault-Systèmes, France) after 3D digitalization with a 3-D laser scanner device (Roland LPX 250). Fifteen FE models were developed to simulate eight different notch depths (0, 1, 2, 3, 4, 5, 6 and 7mm) at 4 mm proximally of the femoral component with and without a femoral stem. The notch depths were considered in the analysis after the examination of 296 knee

radiographs (215 women and 81 men, with a mean age of 67 years) after TKA, including 36 knees (12%) with femoral notching (Figure 1).

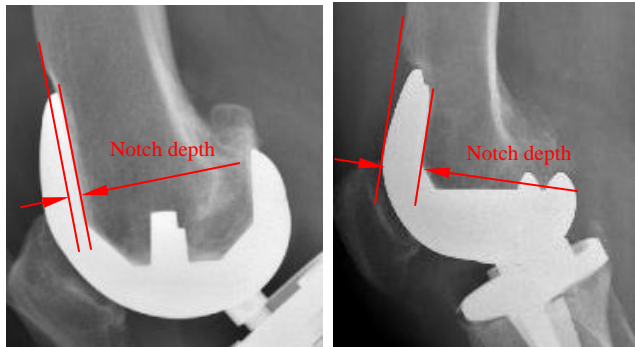
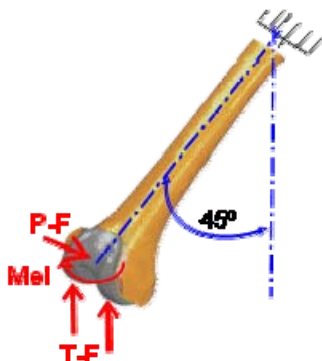


Figure 1 – Radiographs of replaced knees with anterior femoral notching.

In all models the notch radius was 0.7mm based on the standard saw used in the knee surgery. A close physiological load case was applied to assess the principal strain fields at the notch region for a femoral component with and without a stem.

Table 1: Forces and material proprieties of the FE models



Forces and moments applied		
T-F (Tibio-femoral force)	2900N	
P-F (Patella-femoral force)	1746N	
Med. (internal-external moment)	8Nm	
Material proprieties of FE models		
	Young modulus	Poisson ratio
Cancellous Bone	0.155 GPa	0.3
Cortical Bone	16.7 GPa	0.3
Stem - Ti-6Al-4F	110 GPa	0.3
Femoral component -Co-Cr-Mo	210 GPa	0.3
Bone cement	2.28 GPa	0.3

The values of the applied forces (Table 1) [5] correspond to “upstairs” activity with patella-femoral and tibio-femoral forces as well as an internal-external moment. The mesh

models were made using FE meshing software HyperMesh v8.0 (Altair Engineering, Troy, USA). Non-linear finite element analyses were performed with ABAQUS (6.7-1) for CATIA-V5 version 2.5 (Providence, RI, USA). The contact cement-implant and implant-bone were modeled using coefficients of friction of 0.25 and 0.3 respectively. The cement was considered rigidly bonded to bone. Before the creation of all FE mesh models a convergence analysis relatively to the maximum displacement of the FE model was assessed. The convergence rate of the maximum displacement for a mesh of more than 170 000 tetrahedral ten-node elements was less than 0.4%. The material properties simulated are in Table 1 and were assumed to be homogeneous, isotropic and linear elastic. Comparative analyses of the principal maximal and minimal strains patterns and peak values at the notch region for different notch depths with and without femoral stem were made. The principal strains were analyzed along the notch alignment between the medial and lateral sides.

RESULTS AND DISCUSSION

The strains in the femur cortex evidence that the increase of the notch depth increases the strains next to the bone cut (Figure 2) relatively to the femur without notch. The increase was more considerable for the minimal principal strains at the medial notch limit where the maximum increase was observed for the femur with a notch depth of 7 mm. A peak increase of the maximal principal strains was observed at the lateral side (at the notch limit). These strains augment were more important for notch depths greater than 4 mm. In addition, notch depths superior to 4 mm reduce the minimal principal strains at the anterior cortex along the notch distance. The effect of strain modification with the notch was reduced after overtake the mid distance of the medial and lateral femur sides for all notch depths.

The principal strains for the stemmed femoral component can be depicted of figure 3. The use of a femoral press-fit stem with 125mm of length reduces the peak values of the

minimal and maximal principal strains in all models relatively to the same stemless femoral notch depth model.

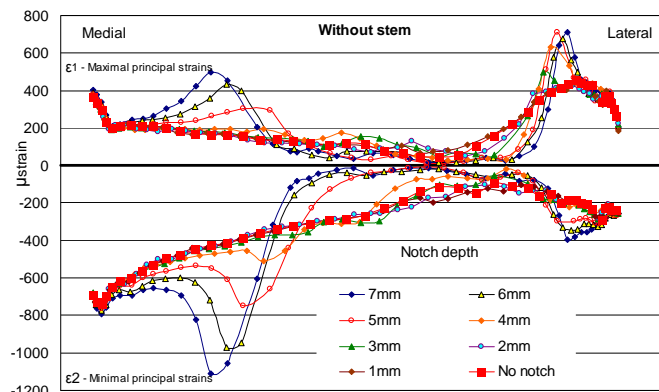


Figure 2 – Principal strains along the notch alignment between the medial and lateral side (stemless femoral component).

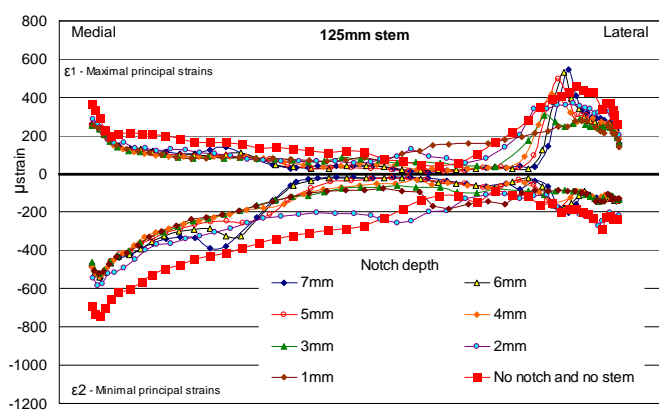


Figure 3 – Principal strains along the notch alignment between the medial and lateral side (stemmed femoral component).

At the medial notch region the peak strain values were inferior to the principal strain of the femur without notch, but at the lateral notch region the use of a stem does not reduce the peak of the maximal principal strains to magnitudes lower than the femur without notch. With exception of the peak strain regions the use of a femoral stem diminishes noticeably the principal strain at the notch region in the stemmed femur relatively to the stemless femur. The peak of the principal strain in the stemless femur for notch depth greater than 4 mm it's far of the fracture

limit strain to the cortical bone ($\pm 21000 \mu\text{strain}$). However this localized strain increase after TKA can modify the normal bone remodeling process and potentiate a latter fatigue fracture. The use of a femoral stem reduces the peak strains and reduces the risk of bone fatigue fracture at these regions. The use of a femoral stem also reduces the strains in the others bone regions that can promote a strain shielding effect and therefore osteopenia. As said previously, osteopenia and femoral notching are the most often reasons for femoral fracture.

CONCLUSIONS

In conclusion, the use of prophylactic stems for notch depths greater than 4 mm are helpful and should be considered in surgery in the cases where bone quality is good with no signs of osteopenia. In the cases of notch depth higher than 4 mm in patients with evident osteopenia signs, the use of stem should be avoided and after knee replacement it seems to be prudent to protect the patient of implant weight bearing.

REFERENCES

- [1] Aaron RK, Scott R. Supracondylar fracture of the femur after total knee arthroplasty. *Clin Orthop* 1987;219:136–9.
- [2] DiGioia 3rd AM, Rubash HE. Periprosthetic fractures of the femur after total knee arthroplasty. A literature review and treatment algorithm. *Clin Orthop* 1991;271:135–42.
- [3] Ritter MA, Thong AE, Keating ME, Faris PM, Meding JB, Berend ME, Pierson JL, Davis KE. The effect of femoral notching during total knee arthroplasty on the prevalence of postoperative femoral fractures and on clinical outcome. *J Bone Joint Surg Am* 2005;87:2411–4.
- [4] Lesh ML, Schneider DJ, Deol G, et al. The consequences of anterior femoral notching in total knee arthroplasty: a biomechanical study. *J Bone Joint Surg* 2000;82A:1096.
- [5] Matthews, L.S., Sonstegard DA, Henke JA., 1977. Load bearing characteristics of the patello-femoral joint. *Acta-Orthop-Scand*. 48(5), 511.

On liver modelling and simulation under trauma situations

C. CONTE*†, C. MASSON†, N. Cheyne† and P.J. ARNOUX†

† Laboratoire de Biomécanique Appliquée, INRETS/Université de la Méditerranée, Bd P. Dramard 13916 MARSEILLE Cedex 20, FRANCE

*Corresponding author Email: cecile.conte@inrets.fr

Abstract

Thoracic and abdominal organs are highly injured during crash situations leading to severe traumas with high morbidity. To prevent this, the definition of efficient safety devices should be based on a detailed knowledge of injury mechanisms and related injury criteria. In this sense, FE simulation coupled to experiment could be a valuable tool to provide a better understanding of internal organs behaviour. This preliminary study aims to improve FE model focussing on liver mechanical behaviour. It concerns the identification of structure mechanical properties up to the evaluation of damage occurrence. This work intends to build a methodology to implement the liver behaviour in a FEM that is robust enough to describe the biological, intrinsic and experimental variability. It is based on an ongoing experimental characterisation of the liver under quasi-static compression. A first set of model parameters, relevant with the sub injury level was first obtained. Then, the damage evaluation was performed through Von Mises levels analysis by comparison to the experimental tests including necropsies and histological structure analysis. Results highlights that damage was centred in the middle part of the right lobe. This let us complete understanding on injury mechanisms and clinical data of liver traumas.

Keywords: liver, FE simulation, inverse analysis, damage evaluation

1. Introduction

Thoracic and abdominal organs are usually simulated in finite elements models (FEM) of the human body using viscoelastic or hyperelastic behaviour laws [1, 2]. Experimental investigations of organs mechanical behaviour under compressive loadings follow two ways: the use of tissue samples to give a local information that must be analyzed considering border effects [3] or the whole structure behaviour evaluation [4]. This last method, at the organ level, must be coupled to an inverse analysis to improve identification process. This work aims to build a methodology to implement the liver behaviour in a FEM that is robust enough to describe the biological, intrinsic and experimental variability. It is based on an ongoing experimental characterisation of the liver under quasi-static compression and is a preliminary to the building of a model able to describe the damage of hepatic tissues.

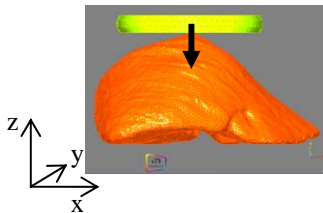


Figure 1. Rear to front compression of the liver

2. Methods

2.1. Setting of behavior law

The FEM was build from CT-scan data [5]. The Glisson's capsule, modelled using shell elements, is assumed as elastic. The parenchyme, meshed with tetra elements of characteristic length about 6 mm, was set hyperelastic with a Mooney-Rivlin law (Eq. 1 et 2). Both structures were assumed as homogeneous and isotropic.

$$W = C_{10}(I_1 - 3) + C_{01}(I_2 - 3) \quad \text{Eq. 1}$$

$$\text{with } \begin{cases} I_1 = \text{tr}(\underline{\underline{C}}) \\ I_2 = \frac{I_1^2 - \text{tr}(\underline{\underline{C}}^2)}{2} \end{cases} \quad \text{Eq. 2}$$

where W is the Helmholtz free energy function, I_1 et I_2 are the two first invariants of the Cauchy tensor $\underline{\underline{C}}$ and C_{10} et C_{01} are two parameters of the law expressed in MPa.

2.2. Inverse analysis method

Model parameters were quantified through experimental uniaxial compression tests in the rear to front direction at 0.001 m/s (Figure 1). The experimental corridor (black curves in Figure 2) was build from the first results of this campaign.

Factors	Min.	Max.	Direct influences	Coupled influences	
			Direct contrast	Second factor	Interaction contrast
Density d in g/mm^3	0.0005	0.0015	3	ν	4
				C_{10}	2
				C_{01}	1
Poisson coefficient ν	0.2	0.495	25	C_{10}	13
				C_{01}	13
Module C_{10} in MPa	0.001	0.1	31	C_{01}	5
Module C_{01} in MPa	0.001	0.1	35		

Table 1. Values and influences of the design factors: for each factor, minimal and maximal values are used for the exploration of responses space. Their influence, alone or in interaction with another factor, is computed using Eq. 4.

The identification methodology was based on an inverse analysis methodology which followed three steps:

Step 1: Space of potential responses exploration.

In order to define the set of parameters for the behaviour law the design of experiments methods was used. The sampling method chosen was a 2 levels complete factorial design [6] with 4 factors (parenchyma density d and Poisson's coefficient ν , C_{10} and C_{01}) (Table 1). The response of a given treatment was the evaluation function Y defined by Eq. 3. Y was the average of relative difference between the force needed to reach a displacement u_i in the treatment configuration $F_{treat}(u_i)$ and in a reference one $F_{ref}(u_i)$:

$$Y = \frac{1}{N} \sum_{i=1}^N \left| \frac{F_{treat}(u_i) - F_{ref}(u_i)}{F_{ref}(u_i)} \right| \quad \text{Eq. 3}$$

N is the number of points of the response curve. The reference configuration (grey curve in Figure 2) is: $d = 0.001 \text{ g/mm}^3$, $\nu = 0,495$, $C_{10} = 0.003 \text{ MPa}$ and $C_{01} = 0.011 \text{ MPa}$.

Step 2: Model optimisation using a NLPQL method [7] applied to the relevant set of parameters of step 1. The optimisation function definition was the same as for the evaluation function replacing the reference curve in Eq. 3 with a standard curve of the upper part of the corridor obtained during a

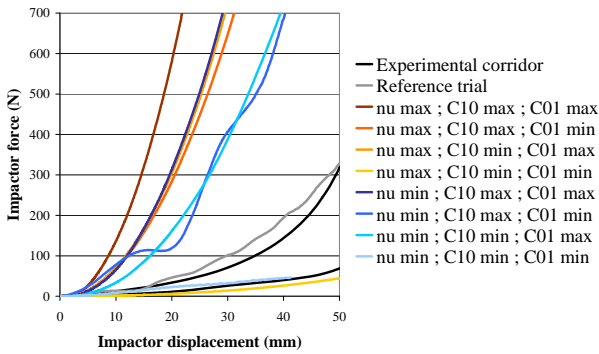


Figure 2. Responses of the influent treatments.

second experimental campaign. To attenuate geometrical differences between experimental and numerical livers, relative displacements defined by

$$(u_{i,rel} = \frac{u_i}{th_0}, th_0 \text{ being the liver initial thickness})$$

are used instead of effective displacements u_i .

Step 3: Robustness analysis of the optimised model. Effects of isolated and crossed variations of the influent parameters were investigated in the neighbourhood of their optimal value ($\pm 10\%$).

2.3. Damage observation

As a first step toward damage integration in the model, the areas of potential damage are computed using the optimised model and compared to those noticed during the experimental tests. At the moment, the maximal values of the Von Mises equivalent stress were used as a way to isolated stress concentration areas which could be associated to damage occurrence in first approximation.

3. Results

3.1. Inverse analysis

The mean evaluation function obtained for the 16 treatments of the step 1 was 462%. The model sensitivity to one parameter p was evaluated calculating the corresponding contrast:

$$c(p) = \sum_{i=1}^{N_{treat}} l_i Y_i \quad \text{Eq. 4}$$

where N_{treat} is the number of treatments performed for the design, Y_i is the computed evaluation function and l_i is the level of p for the treatment i (-1 if p is minimum and +1 if p is maximum)

p was considered as influent once its contrast reached 5 (Table 1). The model was then independent of the density (alone or interacting with another parameter). On the other hand, with the used behaviour law the model exhibited a high

sensitivity to ν , C_{10} and C_{01} with a high dispersion of the responses (Table 1 and Figure 2). The initial slope of curves increased with the modules and decreased with ν . Lastly, as C_{10} and C_{01} had a similar effect, their variation ranges were assumed as the same. Three configurations were then selected, giving the following variation ranges: C_{10} and C_{01} between 0.001 and 0.005 MPa and ν between 0.2 and 0.495.

Optimisation (step 2) is performed within these variation ranges on the three influent parameters. The final set of parameters was chosen on the bases of the optimisation process ($Y \leq 0.2$) and relevance with corridors data. After 25 runs of the NLPQL algorithm, the optimised set of parameters is: $\nu = 0.4$, $C_{10} = 0.005$ MPa and $C_{01} = 0.003$ MPa. For this set of parameters, the optimisation function scored 0.18, which represents a suitable deviation between experiment and simulation in the elastic phase of the compression process where damage does not occur yet (Figure 3). Moreover, the value of ν is consistent with the hypothesis of incompressibility currently assumed [8].

3.2. Damage observation

An approximate three-dimensional distribution of failure observed with experiments is given in the Figure 4. We can then isolate 5 cracks: 3 are independent and 2 are coupled and form the main crack. Their direction of propagation is the right-left axis of the liver (x-axis in Figure 1) and the crack plan is vertical (xz-plan in Figure 1). This result is consistent with the common assumption that forces controlling the failure are normal to the

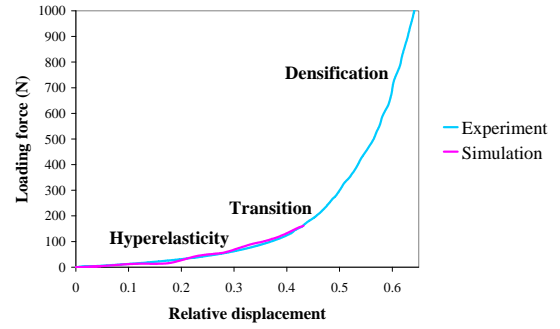


Figure 3. Response of the optimised model in the elastic phase of the compression.

loading direction and oriented from the centre to the surface of liver because of the organ spreading.

On simulation, the maximal Von Mises equivalent stress reached is 0.040 MPa. As a comparison, the critical stress in traction for liver is between 0.066 and 0.386 MPa [9] which confirms that the model reaches an acceptable stress order at the end of the elastic phase of the compression. At this level, the areas of potential damage (three higher levels of Von Mises stress) are roughly relevant with the experimental cracks (Figure 5) in term of location and direction. Failure is located only in the right lobe and is maximal near the hilum. However, in the simulation, the area is larger in the vertical direction (along the z-axis in Figure 1) and less extensive in the lateral one (along the x-axis in Figure 1). Notes the secondary cracks are not present with simulations. These results show that in first approximation the current model can be adapted to describe damage and failure of the liver.

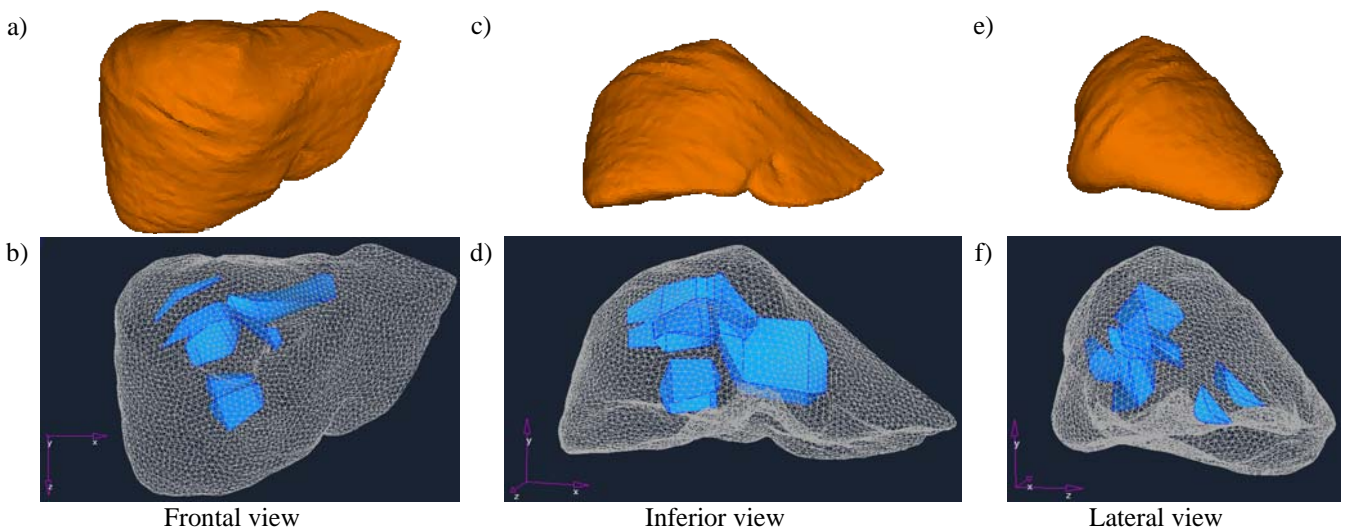


Figure 4. 3D localisation of experimental damage: a, c and e are visualisations of the external surface whereas b, d and f are internal visualisations of the liver in frontal, inferior and lateral view (respectively). The blue 3D-components stand for the surface of failure observed experimentally.

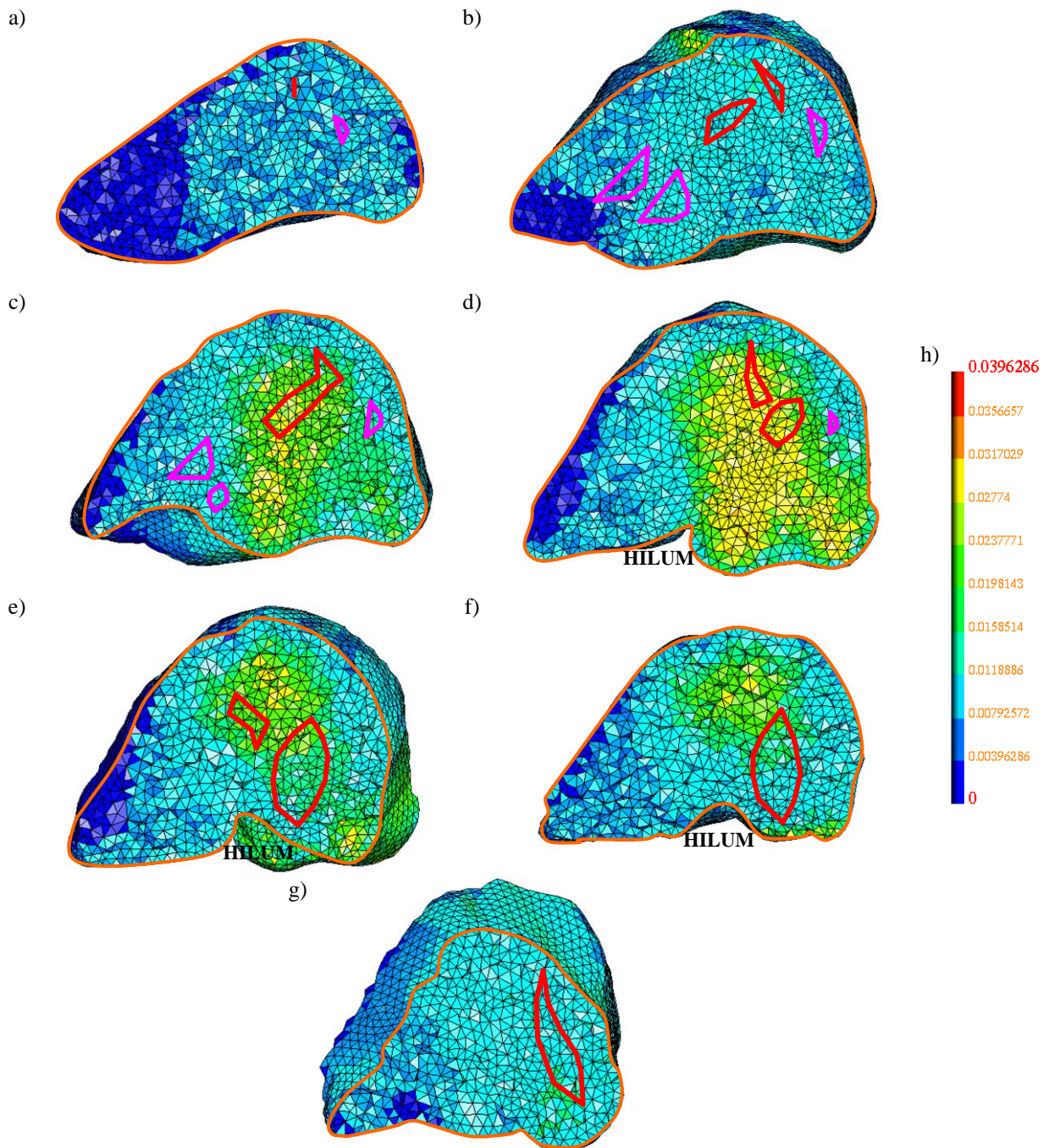


Figure 5. Comparison between maximal Von Mises equivalent stresses localisation after simulation and experimental failure areas: a, b, c, d, e, f and g show sections of the right lobe of the liver model by sagittal plans from right to left. Contours of the section are lined in orange, those of experimental cracks are lined in red for the main one and in pink for others. h gives the Von Mises equivalent stress levels in MPa.

4. Discussion and conclusion

This work describes an integrated approach coupling exploration, optimisation and robustness analysis. Applied to the liver, this approach was used to isolate the admissible set of influent parameters including their potential variations to fit a hyperelastic law. For the material behaviour, accuracy will be improved by adding viscous

component to describe strain rate effects [2]. For damage and failure integration, simulation results will best fit experimental observation by having a method to physically implement failure process in the model. By the way, a more complete description of the structure is necessary to improve description of the crack initiation and propagation. In particular, the main vascular structures which concentrate stresses and the global geometry which

is different from one liver to another must be taken into account. In a further step, the objective will be to determine relationship between the variation ranges of parameters and the biological variability of the experimental population. At least, this methodology will then be extended to more complex model such as hyper-viscoelastic model including damage and failure.

5. Bibliography

1. Carter, F.J., et al., *Measurements and modelling of the compliance of human and porcine organs*. Medical Image Analysis, 2001. **5**(4): p. 231-236.
2. Miller, K., *Constitutive modelling of abdominal organs*. Journal of Biomechanics, 2000. **33**(3): p. 367-373.
3. Chui, C., et al., *Transversely isotropic properties of porcine liver tissue: experiments and constitutive modelling*. Med Bio Eng Comput, 2007. **45**: p. 99-106.
4. Farshad, M., et al., *Material characterization of the pig kidney in relation with the biomechanical analysis of renal trauma*. Journal of Biomechanics, 1999. **32**(4): p. 417-425.
5. Labé, A., *Etude des mécanismes lésionnels de la région abdomino-pelvienne. Applications à la traumatologie virtuelle et à la sécurité routière.*, in *UMRT24 INRETS / Université de la Méditerranée*. 2008, Université de la Méditerranée Aix-Marseille II: Marseille.
6. Clément, B., *Plannification et analyse statistique d'expérience*. Document de cours, Ecole Polytechnique de Montréal, Département de mathématiques et de génie industriel, 2006.
7. Schittkowski, K., *NLPQL: A Fortran subroutine for solving constrained nonlinear programming problems*. Annals of Operations Research, 1985/86. **5**: p. 485-500.
8. Saraf, H., et al., *Mechanical properties of soft human tissues under dynamic loading*. Journal of Biomechanics, 2007. **40**(9): p. 1960-1967.
9. Stingl, J., et al., *Morphology and some biomechanical properties of human liver and spleen*. Surg Radiol Anat, 2002. **24**(5): p. 285-9.

Development of a Hyperelastic Finite Element Model to Simulate the Behavior of Complex Organs (Membrane and Underlying Tissues)

H. Daanouni, Y. Tillier, F. Bay

Mines ParisTech, CEMEF - Centre de Mise en Forme des Matériaux, CNRS UMR 7635, BP 207,

1 rue Claude Daunesse, 06904 Sophia Antipolis Cedex, France

Email: Hicham.daanouni@mines-paristech.fr; Yannick.tillier@mines-paristech.fr; Francois.Bay@mines-paristech.fr;

ABSTRACT:

Nowadays, modelling surgery of soft tissues appears to be a promising and helpful way of teaching and predicting surgical operations. This work aims at predicting the mechanical response of complex organs - composed by a thin membrane and underlying tissues - undergoing multiaxial loadings using a finite element code (VSurgeon3). This software is developed in our laboratory and is based on tetrahedron P1+/P1 elements and on a mixed pressure-velocity formulation.

The constitutive equations used for modelling the behaviour of the membrane and adjacent tissues are hyperelastic models. Three different models (neo-Hookean model, Mooney-Rivlin model and a third one with higher degree of non-linearity) have been implemented in VSurgeon3.

KEYWORDS: Hyperelastic materials, multibodies, large deformation

1 INTRODUCTION

Objectives of this work are to develop a finite element software (VSurgeon3) able to model an organ with all its deformable tissues (membrane and several constitutive elements) and surgeon procedures such as breast biopsy [1], prostate biopsy [2], cutting tasks [3] ...

The constitutive equations used for modelling the behaviour of the membrane and adjacent tissues are hyperelastic models. Three different models (Neo-Hookean [4] model, Mooney-Rivlin [5] model and a third one with higher degree of non-linearity [6]) have been implemented in VSurgeon3; these models were selected after a literature survey. Our choice went to simplest models with less parameters to identify.

VSurgeon3 is a finite element code developed in our laboratory and based on a mixed pressure-velocity formulation. The contact between the different structures of the organ and between the organ and tools is based on a master/slave algorithm [7]. The penalization method is used in order to impose the non-penetrability condition. Volumes of different organ parts are discretized with tetrahedron P1+/P1 elements [8].

Our numerical developments allow us to deal with several bodies, each of them being modelled using its own behaviour. The software can be run on parallel computers.

At each stage of our work, numerical developments have been validated by comparing computed results to analytical ones. The hyperelastic and multibodies version of the VSurgeon3 software obtained has been applied to one of the most popular surgical procedures used in clinical practice, namely the subcutaneous insertion of needles or catheters.

This method is largely used by surgeons, for instance during biopsies. During this procedure, surgeons are able to feel the different tissues depending on the force feedback they received from the needle. This work aims at simulating a needle insertion through an organ composed by different tissue layers (skin, fatty tissues and a more rigid body which can be representative of a tumour) and evaluating the total axial insertion force. This force is directly linked to tissues behaviours.

The implementation of a kill element method was necessary in order to enable the needle to penetrate the tissues.

In this paper, we shall first present a brief overview of the hyperelasticity theory. We shall then introduce the hyperelastic models selected for modelling soft tissues and the numerical developments that we have performed for introducing these models in our finite element software after developments validation, we shall conclude by presenting some needle insertion results.

2 MECANICAL FORMULATION

In this section, we present a brief overview of the hyperelastic materials and their main scientific aspects. We then present the three different hyperelastic models that we have implemented in our finite element software VSurgeon3.

2.1 HYPERELASTICITY

A hyperelastic material has a linear or non-linear behaviour with respect to strain, path-independent, and recovers completely from large deformation. In our case, we assume the material to be isotropic and nearly or purely incompressible.

The stress can be expressed in terms of an energy density function (W) that verifies [9]:

$$S = 2 \frac{\partial W}{\partial C} = 2 \sum_{i=1}^2 \frac{\partial W}{\partial I_i} \frac{\partial I_i}{\partial C} \quad (1)$$

S denotes the second Piola-Kirchhoff tensor, C the right Cauchy-Green strain tensor $C = F^T F$, $F = Grad x$ the deformation gradient. The energy function is expressed as a function of the invariants of C , $W = W(I_1, I_2)$ [9]. The invariants of the right Cauchy-Green tensor are given by $I_1 = tr(C)$, $I_2 = \frac{1}{2} [(tr(C))^2 - tr(C^2)]$ and $I_3 = \det(C) = 1$ (incompressibility hypothesis). More details can be found in [9, 10].

The Cauchy stress tensor σ is related to the second Piola-Kirchhoff S tensor by:

$$S = J F^{-1} \sigma^T (F^{-1}) \quad (2)$$

Where $J = \det F$.

From (1) and (2) we can deduce the Cauchy stress tensor expression:

$$\sigma = 2 \left[\frac{\partial W}{\partial I_1} B - \frac{\partial W}{\partial I_2} B^{-1} \right] - P' I = \sigma' - P' I \quad (3)$$

σ' is not the deviator stress tensor. B is the left Cauchy-Green strain tensor $B = FF^T$.

2.2 Contact analysis

Contact problems are highly non-linear because of the boundary conditions which are continuously

changing in the region of contact with deformation. Resolution of contact problems between a deformable body and a rigid body or between deformable bodies is based on a master/slave algorithm [7]. The penalization method is used in order to impose the non-penetrability condition. A total resolution is applied for all the bodies in contact. The same master/slave technique is used in order to solve the self-contact problems [7].

2.3 MODELS IMPLEMENTED

Several models are proposed in literature. A recent survey on hyperelastic models was made by VERRON and al [4]. They studied twenty different hyperelastic constitutive models suitable for rubber, from the Mooney-Rivlin (1940) one to the micro-sphere model (2004) in the incompressible case. For our study we have selected three models, the neo-Hookean model, the Mooney-Rivlin one and a third one with a higher degree of non-linearity – the Fung model [6].

The constitutive laws corresponding to the three models are listed in the table below.

Table 1: Constitutive equations

Model	Energy function W	σ'
Neo-Hookean	$W = c_1 (I_1 - 3)$	$\sigma' = 2 c_1 B$
Mooney-Rivlin	$W = c_1 (I_1 - 3) + c_2 (I_2 - 3)$	$\sigma' = 2c_1 B - 2c_2 B^{-1}$
Fung	$W = \frac{\mu}{2\gamma} (e^{\gamma(I_1-3)} - 1)$	$\sigma' = \mu (e^{\gamma(I_1-3)})B$

3 NUMERICAL RESOLUTION

In this section, we present a finite element approach for solving problem (4). The full or nearly full incompressibility constraint led us to use a mixed formulation in terms of velocity and pressure fields [4, 11].

A time and a space discretizations are used.

3.1 WEAK MIXED FORMULATION

In the case of a mixed formulation, for an incompressible hyperelastic material, the solution of the problem must satisfy the following system for any virtual (velocity, pressure) (v^* , p^*) couple:

$$\begin{cases} \int_{\Omega} s^{t+\Delta t}(v) : \varepsilon(v^*) - \int_{\partial\Omega} T^{t+\Delta t}(v) \cdot v^* - \int_{\Omega} p^{t+\Delta t} \operatorname{div}(v^*) - \int_{\Omega} \rho g \cdot v^* = 0 \\ \int_{\Omega} p^* \left(\operatorname{div}(v^*) + \frac{\det F' - 1}{\det F' \Delta t} \right) = 0 \end{cases} \quad (4)$$

System (4) is an incremental mixed formulation of the problem.

3.2 FINITE ELEMENT DISCRETIZATION

3.2.1 Time discretization

The unknown of problem (4) is the couple (displacement, pressure). For a time step Δt small enough, we can assume that velocity is constant during the time step Δt . We update the displacement field using an explicit integration scheme:

$$u^{t+\Delta t} = u^t + \Delta t.v^t \quad (5)$$

3.2.2 Space discretization

In VSurgeon3, we use a linear tetrahedral element with a bubble function for velocity interpolation. These elements are represented on figure 2. More details on this type of elements can be found in [8].

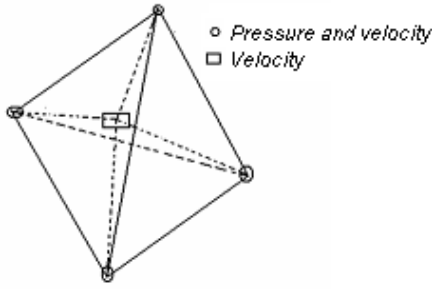


Figure 1: interpolation in mini-elements.

The discrete velocity v_h and pressure p_h fields are given by:

$$\begin{aligned} v_h &= v_h^l + v_h^b = \sum_{k=1}^{nbnoe} V_k N_k^l + \sum_{i=1}^{nbelv} V_i N_i^b \\ p_h &= \sum_{k=1}^{nbnoe} P_k N_k^l \end{aligned} \quad (6)$$

N^l , N^b are respectively linear and bubble functions.

3.3 Kill element method

In order to simulate the insertion of a needle into an organ, we need to suppress some elements in contact with the needle. A “kill element” method which is one of the easiest methods for modelling this technique has been used. A criterion, based on the maximal equivalent strain and set by the operator is introduced. At each simulation time step, the maximal equivalent strain is computed. When the value is higher than the criterion, the element contribution to the rigidity matrix is

suppressed i.e. it does no longer contribute to the mechanical calculation.

4 VALIDATION & APPLICATIONS

The aim of this section is to validate the implementation work presented before, and to show the ability of VSurgeon3 to model the behaviour of organs which might undergo large deformations during the needle penetration. First, some classical validation cases are presented, and then, a surgical application of our software is presented.

4.1 VALIDATION

In order to test the validity of the code, two cases are investigated, one with a single deformable body and another case with several deformable bodies.

4.1.1 Single deformable body

A uniaxial tension test of a cube quite popular in literature [3, 12] is considered. A 5 mm cube (figure 3a) is stretched over 20 mm. One advantage of this case is that we can easily determine the analytical solution. For example the analytical solution in the case of the Mooney-Rivlin model is given by:

$$\sigma_{zz} = 2C_1 \left[\frac{L^2}{L_0^2} - \frac{L_0}{L} \right] - 2C_2 \left[\frac{L_0^2}{L^2} - \frac{L}{L_0} \right] \quad (7)$$

Where C_1 and C_2 denote the material coefficients and L_0 the initial length of the cube.

The following figure shows the results of a simulation with VSurgeon3. The constitutive equation which was used is a Mooney-Rivlin one. A bilateral sticking contact is set between the cube and the upper and lower dies. The result obtained using VSurgeon3 is shown on Figure 2.

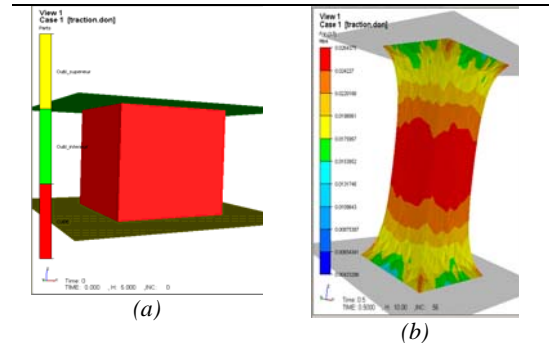


Figure 2: (a) Initial state of cube before stretching. (b) Computed Isovalues of Von Mises (VSurgeon3)

This computed result was compared to the analytical solution. As we can see on figure (3), both solutions are very close.

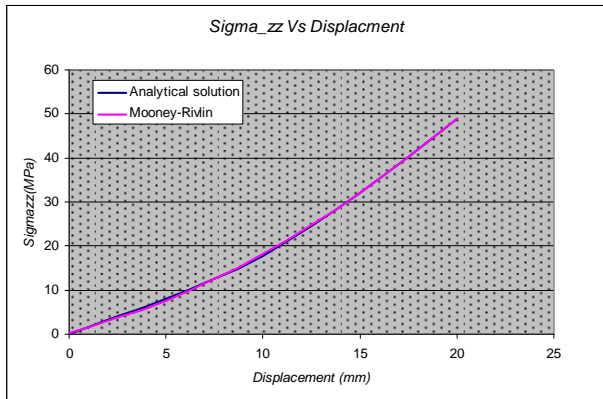
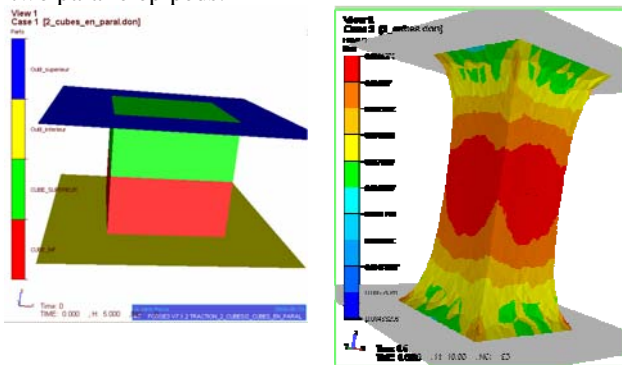


Figure 3: Comparison between VSurgeon3 results and analytical solution for the tension test

4.1.2 Several deformable bodies

Here, two parallelepipeds (2.5 x 5 mm) stuck together and forming a cube similar to the previous one are stretched. A bilateral sticking contact is set between deformable bodies and tools. The same behaviour as the one used for the single deformable body is applied to the two parallelepipeds.



a: Initial state of tow parallelepipeds before stretching *b*: After stretching

Figure 4: Isovalues of Von Mises

As it may be observed on figures 3b and 4b, results are quite similar in both cases. The small difference can be explained by the mesh design which is not exactly the same.

In a second stage, two different behaviours were assigned to each of the parallelepipeds. The less rigid parallelepiped (the lower one on Fig. 5) exhibits logically larger deformation.

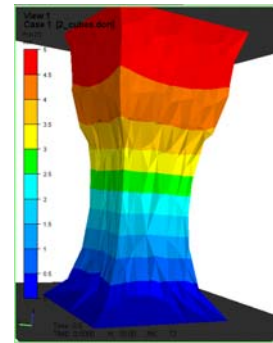


Figure 5: Displacement field

4.2 Needle insertion through an organ

Needle insertion through an organ has been chosen as application of our new software VSurgeon3, the following figure shows a model of kidney.

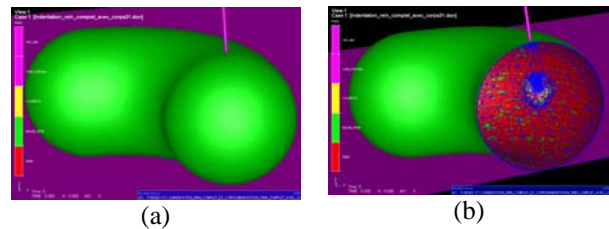


Figure 6: Model presentation, (a) Full model, (b) Model with a cut plan.

This model is composed by three different layers: a membrane (body A); tissue of the kidney (body B) and a third body (body C) which will be the target of the needle.

A bilateral sticking contact (no sliding is allowed between the different sub-tissues) is considered between the different deformable bodies. On the contrary, a sliding contact is considered between the needle and deformable bodies.

The constitutive equation chosen for this case is a neo-Hookean model, with $C_{1bodyC} = 10.C_{1bodyA}$ and $C_{1bodyC} = 100.C_{1bodyB}$. The value of C_1 is chosen arbitrarily. The needle has a constant velocity of 2mm/s in (-z) direction.

Due to the kill-element method used, the mesh size along the needle path must be as fine as possible as shown on the following figure.

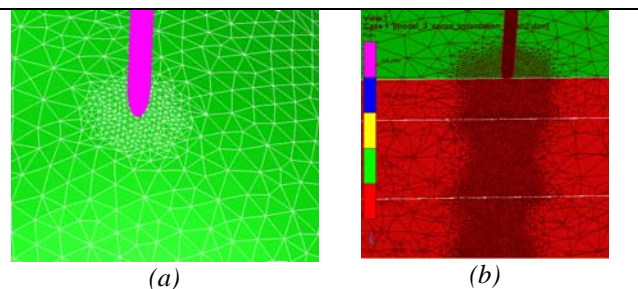


Figure 7: volume mesh

The maximum equivalent strain criterion used by the kill-element method was set to 1.5.

4.3 Results

Needle insertion simulation results are presented on figure 8.

One can see that elements which have an equivalent strain higher than 1.5 are killed and do not contribute to the mechanical calculation anymore.

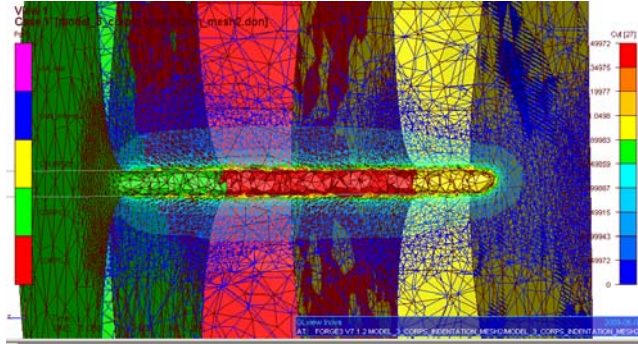


Figure 8: Needle insertion simulation results

Force profile were recorded on the needle and presented here as a function of the needle displacement.

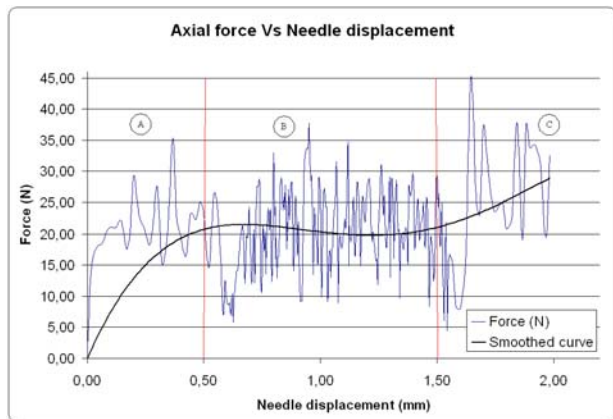


Figure 9: Force evolution vs needle displacement.

The force evolution is reflecting the different tissues behaviour: the force is increasing when the needle moves in the body A. When the needle tip is in contact with the second component of the kidney (ten times softer than body A), the force starts decreasing and then remains more or less constant when the needle is inside body B, which is homogeneous. The force starts to increase again when the needle reaches the body C (one hundred more rigid than body B).

5 Discussion

The contact conditions set between the needle and the deformable bodies is a sliding one; this means that the force relied to friction with the needle is null. Forces recorded during the needle penetration is thus only due to the material behaviours.

Curves on Fig. 9 are quite noisy. This can be explained by the kill element process. Forces are computed using an integration over the elements which are in contact with the needle (non deformable body). Each time the maximum equivalent strain criterion is reached on an element, it does not contribute to the mechanical calculation anymore and leads to a mis-calculation of the force until the needle becomes again in contact with a new one. The finer the mesh, the better the accuracy.

6 CONCLUSIONS

The aim of the present work was to develop a robust software able to predict the mechanical response of an organ with his several tissues to an external solicitation.

Three constitutive models were implemented in VSurgeon3 and validated. It is now possible to model complex organs with their sub-tissues. All numerical developments have been validated by comparing computed results to analytical ones. The contact between deformable bodies or between deformable bodies and tools can be managed using an accurate master/slave algorithm. In order to impose the non-penetrability condition, the penalization method was used.

The VSurgeon3 software was then applied to the simulation of a needle insertion trough a kidney. Results obtained show that the force measured by the needle is strictly depending on tissues behaviours.

This work will be extended to more complex and more realistic surgical procedures with correlation with experimental results.

REFERENCES

- [1] F. S. Azar, D. N. Metaxas, and M. D. Schanall, “A finite Element Model of the breast for predicting Mechanical Deformations during biopsy Procedures,” in Proceedings of the IEEE Workshop on mathematical Methods in Biomedical Image Analysis, pp. 38-45, 2000.
- [2] J. Zeng, C. Kaplan, J. Bauer, J. Xuan, I. A. Sesterhenn, J.H. Lynch, M. T. Freedman, and S. K. Mun, “Optimizing prostate needle biopsy through 3-D simulation,” in Proceedings of SPIE Medical Imaging, Feb 1998.
- [3] Tillier Y. et al., “Finite element modeling for soft tissue surgery based on linear and nonlinear elasticity behaviour”, Computer Aided Surgery, Volume 11, 2006(2),63 – 68
- [4] Marckmann G., Verron E., “Comparison of hyperelastic models for rubberlike materials”, Rubber Chemistry and Technology, 79(5), 835-858, 2006.
- [5] M. MOONEY. « A large theory of a large elastic deformation ». J. Appl. phys., Vol 11, pp. 582-592, 1940
- [6] Fung Y.C. “Elasticity of soft tissues in simple elongation” American Journal of physiology, 213, pp. 1532-1544.
- [7] P. Wriggers: *Computational Contact Mechanics*, (2002)
- [8] Coupez T., “Stable stabilized finite element for 3D forming calculation”. CEMEF. Rapport interne (1996).
- [9] M.F. Beatty « Topics in finite elasticity : hyperelasticity of rubber, elastomers, and biological tissues with examples” Trans. Sc. Rheol., Vol 7, pp. 391-410, 1987
- [10] J. Bonet, R. D. Wood.,– *Nonlinear continuum mechanics for finite element analysis / 1961*
- [11] Chenot J-L, Massoni E. “Finite element modelling and control of new metal forming processes” CEMEF; 2006
- [12] Agassant J.-F., Avenas P., Sergent J.-P., Vergnes B., Vincent M., “*La mise en forme des matières plastiques*”. Technique & Documentation. ISBN : 2-7430-0016-3. Editions Lavoisier (1996).



Session 2B

Biomechanics and Physiology

Mr. Pierre-Jacques Liotier

ISM, UMR 6233

France

pierre-jacques.LIOTIER@univmed.fr



“Spongy bone multicellular unit remodelling model; a physico-chemical approach”

Pierre-Jacques Liotier, Sylvie Wendlingmansuy, Jean-Marie Rossi and Patrick Chabrand

Keywords: bone adaptation; trabecular tissue; time dependent multi-physical model

Summary:

Bone tissue is continuously renewed by processes governed by basic multicellular units (BMU) composed of osteocytes, osteoclasts and osteoblasts submitted to mechanical loading. Osteocytes are known to be integrated mechanosensors that regulate the activation of osteoclasts and osteoblasts involved respectively in bone resorption and apposition. After collagenic tissues apposition, a mineralization process takes place which increases progressively the local effective stiffness. Several remodelling models have been developed at the cellular scale taking into account intercellular communication within BMUs related to local strain-energy. In order to better understand bone remodelling dysfunctions, we have adapted an existing model of bone remodelling at the trabecular scale and introduced time dependent physico-chemical models for each step of the remodelling process. The resorption and mineralization processes have been expressed considering respectively dissolution and cristallization of hydroapatite crytals. The resorption thus depends on the number of involved osteoclasts and on the chemical composition of surrounding system. Mineralization process is described as a cristallization in a metastable sursaturated solution on the collagen substrate. The mineralization rate is then the parameter controlling the stiffness of the span. The apposition process is expressed as a function of the number of involved osteoblasts and on their collagen production rate. The osteoclasts are progressively incapsulated in the collagen and become osteocytes. The osteblast number is thus expressed as a decreaseive function of the newly created osteocytes. Tests lead on several spans with different initial mineralization rate shows that the remodelling occurs when their stiffness reach a sufficient value depending on the mechanical loading. This result permits to remove the arbitrary apposition signal threshold required in previous models. Moreover, the results show bone remodelling turn over that is generally observed in bone renewing. The present model would offer new perspectives to analyze bone remodelling deseases and, new means to diagnosis.



Session 2B

Biomechanics and Physiology

Mr. Deepak Vashishth

Rensselaer Polytechnic Institute

USA

vashid@rpi.edu



“Cohesive Finite Element Approach to Determine Contribution of Bone Quality to Fracture Toughness”

S. Tang, Ani Ural and D. Vashishth

Keywords: finite element, bone, fracture

Summary:

Fragility fractures are a significant public health problem resulting in morbidity, mortality and substantial economic cost. To date, bone mineral density (BMD) is most commonly used clinical tool, however, recent evidence suggests that factors other than the loss of bone mass such as changes in the quality of bone material are of crucial importance to the understanding of fragility fractures. In this study we describe the development of a fracture mechanics based microCT cohesive finite element model to separate the contributions of cortical porosity from material level changes and show its adaptation to predict contribution of advanced glycation end-products (AGEs) towards bone fracture.

Three finite element meshes in the shape of compact tension specimens (E399-90) were generated for the purpose of this study. The 1st is a manually generated solid mesh containing no porosity; the other two were generated from a microCT scan from donors 19yo (1% porosity) and 81yo (5% porosity). The cohesive model employed an ascending and descending branch with a coupled representation of normal and shear crack displacements. The relationship between AGEs and energy release rate (G_c) as well as the extent of AGE increase in the model were within the physiological limits ranging up to 600% increase in AGEs.

With an increase in the percentage of AGEs, less load was required to propagate the crack to the same length, indicating a reduced ability of glycated bone to resist crack propagation. This behavior manifested itself as decreasing values of R-curve slope with an increase in AGE content. In contrast to the prorogation, increased AGE content had no effect on initiation toughness. In conclusion, this study validates a novel constitutive equation relating a biochemical measure of the bone matrix with a fracture behavior parameter, and confirms that physiological levels of AGE accumulation with age increase bone fragility.



Session 3A

Biomedicine - Biomolecule

Mr. Davy Willems

Materialise NV

Belgium

davy.willems@materialise.be



“Using FE simulations to optimize implant and medical device design”

Erik JH Boelen, MSc, PhD; Davy Willems

Keywords: CT/MRI, image processing, rapid product development, medical devices, custom design

Summary:

There is a growing trend towards personalization of medical care, as evidenced by the latest developments in multislice CT imaging and ultra-fast MR imaging, personalized treatment planning in a variety of surgical disciplines and the development of more suitable implantable devices. To support this trend, the role of the biomedical engineer becomes increasingly important, as the operating theater becomes more and more a technical environment. Hospitals need multidisciplinary teams for the development of diagnostic tools, implants and devices, computer assisted surgery and virtual process simulation processes.

Here, we will describe the use of 3D medical image information of individual patients as well as selected patient populations, combined with CAE tools and processes, in the rapid product development of custom and standard implantable devices. The combination of medical image information with CAE methods such as FEA or CFD and Forward Engineering allows the engineer to develop implantable devices faster and better; the design can be optimized according to the outcome of the simulation, using virtual instead of mechanical prototype testing. This will significantly reduce the time to market and is expected to become common practice in the near future, when CAE methods are valued and accepted by the medical community.

Case studies from leading biomedical research institutes as well as medical device manufacturers will be demonstrated for a variety of surgical fields such as orthopaedic, craniomaxillofacial and cardiac surgery.

NON-NEWTONIAN AND TRANSIENT EFFECTS ON THE WALL SHEAR STRESS WITHIN A STENTED ARTERY

Juan Mejia^{1,2}, Rosaire Mongrain^{1,2}, Richard Leask⁴, Olivier F. Bertrand³

¹Department of Mechanical Engineering, McGill University, Montreal, Quebec, Canada

²Montreal Heart Institute, Montreal, Quebec, Canada

³Quebec Heart Institute, Quebec City, Quebec, Canada

⁴Department of Chemical Engineering, McGill University, Montreal, Quebec, Canada

INTRODUCTION AND BACKGROUND

For the last few decades stents have played a central role in the treatment of arteriosclerosis. Although bare-metal stents (BMS) have significantly reduced levels of restenosis rates by 20 or 30% (Duraismamy et al. 2007), restenosis rates remain high at around 25% (Duraismamy et al. 2007). The introduction of drug-eluting stents have reduced restenosis rates even further (Gladius 2008), but are associated with high risk of late thrombosis (Hara et al. 2006).

Recent studies have focused on modeling the behavior of blood within a stented arterial segment, and particularly on the role of stent design on the wall shear stress distribution within a stented artery. However, most studies have assumed blood to be Newtonian and have therefore neglected the dependence of viscosity on shear strain rate (Duraismamy et al. 2007). Neglecting the non-Newtonian nature of blood has been shown to be a valid assumption in many cases, but a recent study by Bernard *et. al* showed that non-Newtonian effects can have a significant influence on the wall shear stress distribution within a steady-state model of a stented artery (Benard et al. 2006).

In this work four different simulations are carried out, corresponding to steady vs. transient and Newtonian vs. non-Newtonian models. The current purpose is to assess the effect of the steady-state and Newtonian assumptions on the resulting wall shear stress (WSS) obtained with state-of-the-art numerical tools. Results will be obtained using a fully three-dimensional geometry of a realistic stent. Important flow features, such as WSS and velocity fields will be compared qualitatively and quantitatively.

MATERIALS AND METHODS

The numerical model corresponds to three-dimensional non-compliant models of a stented artery. A realistic stent design corresponding to a Symbiotech stent (Symbiotech Medical Inc.) is used.

The three-dimensional fluid flow through a stent is solved numerically. The governing equations are solved with a commercial computational fluid dynamics (CFD) software package (ANSYS Inc.). A no-slip boundary condition is set at all walls, and the inlet boundary condition corresponds to a fully developed circular duct profile. For all time dependent simulations a Womersley number of 2.8, which corresponds to approximately 100 beats per minute, is used. The amplitude of the cardiac waveform is adjusted such that the time-averaged flow rate corresponds to a Reynolds number of 190, which corresponds to physiological data. For all steady state simulations the Reynolds number is set to 190 for the purpose of comparison. A normalized flow of the space-averaged duct velocity as a function of time is shown in Figure 1. For the Newtonian model density and viscosity are set to match physiological values (1.05 g/cm³ and 3.5 cP respectively). For the non-Newtonian model density remains the same and the viscosity of blood is modeled using the Carreau-Yasuda approximation (Chien et al. 1966):

$$\mu(\dot{\gamma}) = \mu_{\infty} + (\mu_0 - \mu_{\infty})(1 + (\lambda\dot{\gamma})^a)^b$$

where μ is the apparent viscosity, μ_{∞} is the viscosity at infinite shear rate, μ_0 is the viscosity at zero shear rate, λ is a time constant and a and b are two parameters linking the minimum and maximum viscosity thresholds. The values used for a , b , and λ are those used by Bernard *et al.* (Benard et al. 2006) to fit the experimental results obtained by Chien *et al.* (Benard et al. 2006).

Mesh independence is achieved by gradually increasing the number of elements in the models and comparing the resulting shear strain rate distributions. Mesh independent results are obtained using a

mesh containing a total of 1,357,000 nodes. A similar procedure was followed to ensure time-step independent results. Time-step independence was achieved using a time step with a duration of 0.18% of the cardiac cycle.

Results were obtained at every time-step (approximately 556 times per cycle), but for the sake of brevity only the results obtained at the end of the second cardiac cycle, and at instants A, B, and C are discussed here (Figure 1). Times A and C correspond to the instant in time when the instantaneous Reynolds number corresponds to a value of 190, while time B corresponds to the peak flow rate.

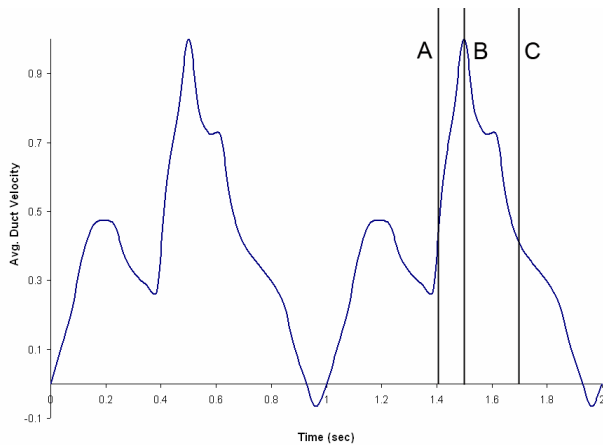


Figure 1 Normalized waveform

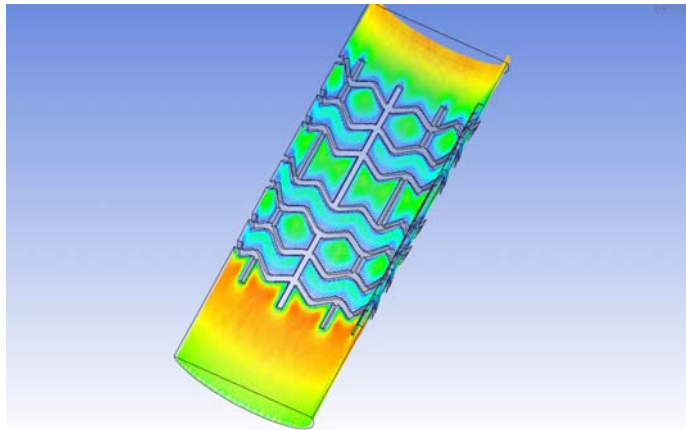


Figure 2 Velocity field at peak flow rate measured half-a-strut distance from the cellular wall

RESULTS

The overall flow pattern obtained for all models is comparable. Qualitatively, the presence of the stent within the arterial region causes an overall reduction of velocity in the region close to the wall, which in turn causes an acceleration of the core flow. As can be seen in Figure 2 velocity is lower adjacent to the struts, and it increases with distance from the struts. However, the velocity close to the wall never reaches the same levels within the stented region as those within the non-stented region.

Figure 3 shows a close-up of the WSS within the stented region for both the Newtonian and non-Newtonian models. It can be observed that the overall levels of WSS are higher for the non-Newtonian model

than for the Newtonian model. These results were obtained at the instant in time when the flow rate is at its peak value (instant B), which also corresponds to the highest overall WSS levels during the cardiac cycle for both models.

The results shown in Figure 4, Figure 5, Figure 6, and Figure 7 were all obtained by measuring the WSS along a polynomial line oriented in the streamwise direction and passing along the vessel wall and over the struts of the stent. In general, all models show similar WSS morphology. Spikes in WSS correspond to the location of the struts, while the region between spikes corresponds to the vessel wall directly exposed to the fluid. WSS levels increase with distance from the struts, but never reaches the same levels as those observed in the non-stented vessel.

Comparing the WSS obtained using a steady state model for the Newtonian and non-Newtonian models shows (Figure 4) that the WSS levels predicted by the steady non-Newtonian model is on average 65% higher. In addition, the morphology of the WSS between struts is markedly different, with the non-Newtonian model exhibiting more pronounced increases in WSS with distance from the struts.

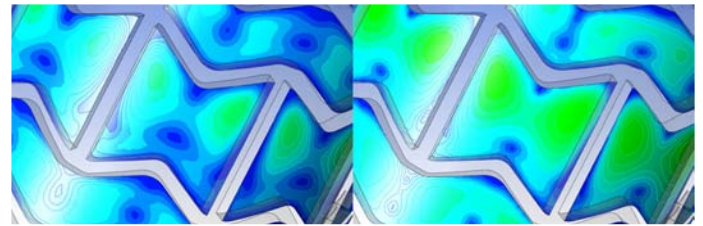


Figure 3 Wall shear stress at peak flow rate for the Newtonian (left) and non-Newtonian (right) models.

Figure 5, Figure 6, and Figure 7 show the WSS obtained, using a time dependent simulation, at instants A, B, and C, respectively. In general the wall shear stress is highest over the struts and lowest in the regions immediately adjacent to the struts. Wall shear stress distribution and levels were markedly different between the Newtonian and non-Newtonian models. Overall, the WSS was higher for the non-Newtonian model, but current results suggest that the discrepancy between the two models varies during the cardiac cycle. The percent difference between the two models was measured at three distinct times (marked as A, B, and C in Figure 1). The percent difference was, on average, 51%, 32%, and 72% for time A, B, and C, respectively.

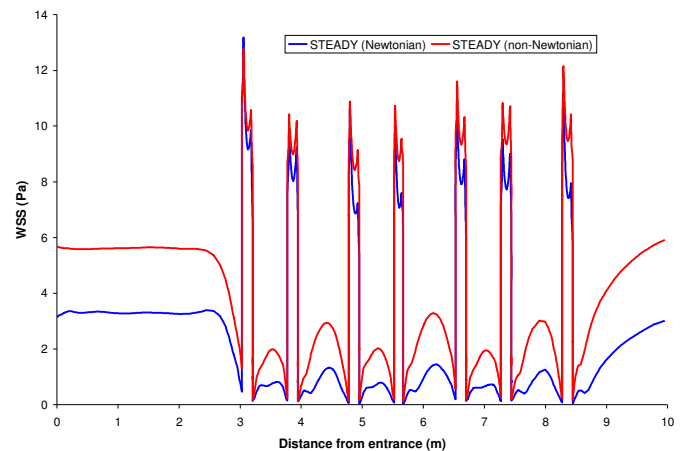


Figure 4 Shear stress along the stented wall obtained using time-independent models

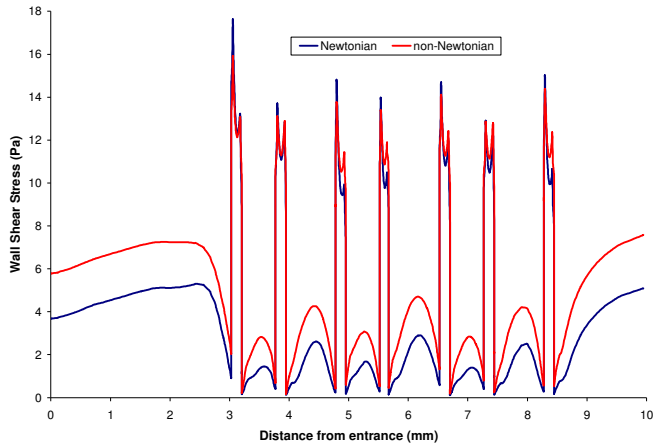


Figure 5 Shear stress along the stented wall at instant A

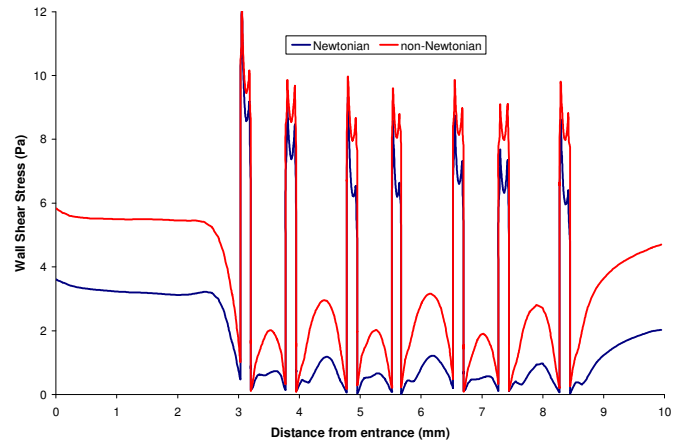


Figure 7 Shear stress along the stented wall at instant C

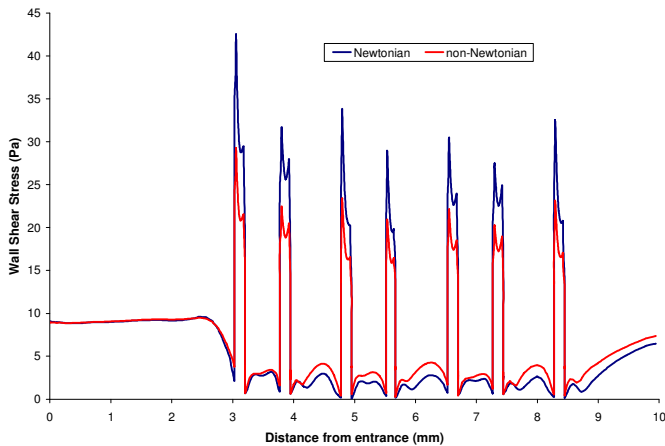


Figure 6 Shear stress along the stented wall at instant B

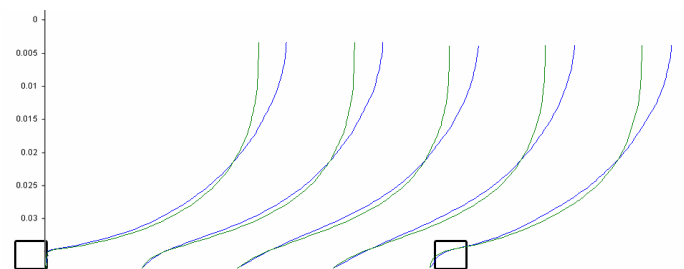


Figure 8 Velocity profiles within two adjacent struts (black squares) at instant C with the Newtonian (blue) and non-Newtonian (green) models.



Figure 9 Velocity profiles within two adjacent struts (black squares) at the end of the second cardiac cycle with the Newtonian (blue) and non-Newtonian (green) models.

Figure 8 and Figure 9 show velocity profiles measured perpendicular to the vessel wall and located between two adjacent struts along the streamwise direction. The velocity profiles shown in Figure 8 show similar morphology for both models, but a close inspection in the near-wall region shows that the slope close to the wall varies between the two models. On the other hand, the velocity profiles shown in Figure 9 are drastically different, revealing that for this particular time-step the non-Newtonian nature of blood plays a dominating role. Large recirculation regions are present in the Newtonian model while none are observed for the non-Newtonian model, as can be seen visually by comparing Figure 10 and Figure 11.

Additional differences between the two models are found when the total cellular area exposed to a WSS below 0.5 Pa is computed. A WSS of 0.5 Pa is generally regarded as the level below which neo-intima hyperplasia is promoted (Benard et al. 2006). Figure 12 shows the percent of the total area exposed to WSS below 0.5 Pa for both the Newtonian and non-Newtonian models, at instants A, B, and C. In every case the area exposed to critically low levels of WSS is significantly lower for the non-Newtonian model. Newtonian assumption may lead to an over prediction of the risk of restenosis within a stented arterial region.

	Instant A		Instant B		Instant C	
	Newtonian	non-Newtonian	Newtonian	non-Newtonian	Newtonian	non-Newtonian
Mean	0.8616	1.6495	0.3493	0.5922	0.3499	1.0725
Standard Deviation	0.5507	0.4107	0.4352	0.3700	0.5542	0.4725
Kurtosis	1.3780	3.1333	0.7830	1.4332	0.6151	2.1035

Table 1. Statistical moments measured between the two struts shown in Figure 10 at different time instants.

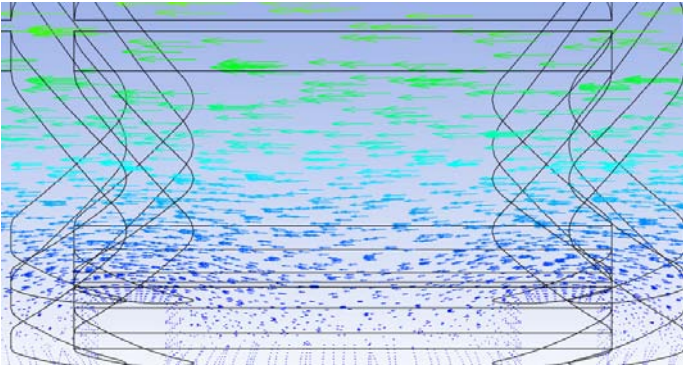


Figure 10 Velocity field within two adjacent struts at the end of the second cardiac cycle (Newtonian).

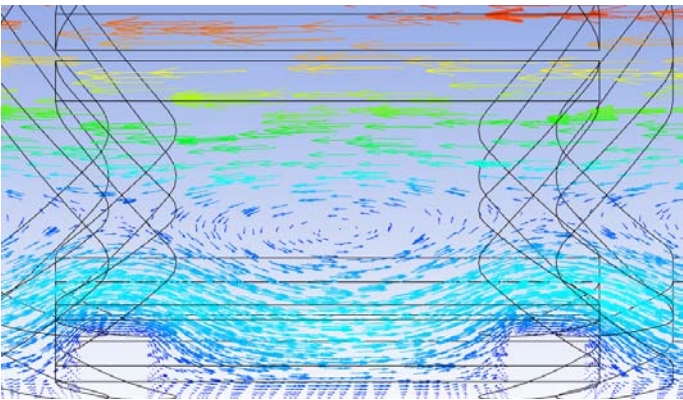


Figure 11 Velocity field within two adjacent struts at the end of the second cardiac cycle (non-Newtonian).

DISCUSSION

Numerical simulations of a stented arterial segment under pulsatile inlet conditions have been performed using both a Newtonian and non-Newtonian models. A transient non-Newtonian model, which more closely resembles the behavior of blood, has never, to the author's knowledge, been presented in the literature. Previous work comparing a steady state with a transient inlet condition using a Newtonian fluid assumption has shown that even if the instantaneous Reynolds number is matched the WSS predicted by the steady-state model is inaccurate (Mejia et al. 2008). Current results suggest that the combination of transient and non-Newtonian effects can have a dramatic effect on both the fluid characteristics and the resulting WSS to which the vessel's cellular wall is exposed to.

Following the idea used by Benard *et al.* and Gijssen *et al.* the characteristic viscosity of the non-Newtonian model has been calculated (Benard et al. 2006; Gijssen et al. 1999). Using average quantities the characteristic viscosity for the case presented here is approximately 0.005 Pa s, or approximately 1.45 times the Newtonian

viscosity (0.0035 Pa s). Current results suggest that the increase in viscosity due to the non-Newtonian nature of blood is enough to dampen the large recirculation regions presented in the Newtonian model (Figure 10 and Figure 11). In fact, the apparent viscosity increase yields a lower Reynolds number, which implies that the viscous dissipation is significantly more dominant for the non-Newtonian case.

In addition, the non-Newtonian effects also affect the WSS within the arterial segment. WSS levels are under predicted with a Newtonian model, which yields, as shown in Figure 12, an over prediction of cellular area exposed to critically low WSS. This result implies that engineering predictions of WSS, obtained using a Newtonian assumption and that were correlated with clinical observations of restenosis were inaccurate. Moreover, it signals to the fact that numerical simulations should model the non-Newtonian nature of blood, although it remains to be shown whether using a characteristic viscosity, as done by Benard *et al.*, is still valid even when dealing with a time dependent system (Benard et al. 2006).

A more robust method of comparing WSS distributions was presented by the authors elsewhere (Mejia et al. 2009). In brief, statistical moments were used to evaluate the value, variation, and overall flatness of the resulting WSS distribution corresponding to different strut designs. This method was used to compare the WSS corresponding to the velocity field shown in Figure 10 and Figure 11. The resulting statistical moments are recorded in Table 1. All values in Table 1 have been non-dimensionalized in the same way as described by Mejia *et al.* (Mejia et al. 2009). Overall the non-Newtonian model has a higher mean, a lower standard deviation, and a higher kurtosis. A higher kurtosis implies that the WSS distribution flatter for the non-Newtonian model, which in combination with a higher average and a lower standard deviation means the cellular area is constantly exposed to higher WSS levels, and therefore a more favorable WSS distribution. These results show the WSS predicted using a non-Newtonian model is closer to that found in a healthy unstented artery, and that a Newtonian model under predicts WSS levels by approximately a factor of 2.

During the cardiac cycle the smallest discrepancy between the Newtonian and non-Newtonian models was found at peak flow rate, which still corresponded to an average percent difference of approximately 32% in WSS levels. At every instant during the cardiac cycle the WSS obtained with the non-Newtonian model was higher in comparison. An inspection of the velocity profiles close to the wall shows that even though there is a difference in shear strain rate at the wall between both models, it is not large enough to account for the difference in WSS. Therefore, variations in viscosity play an important role in this type of flow.

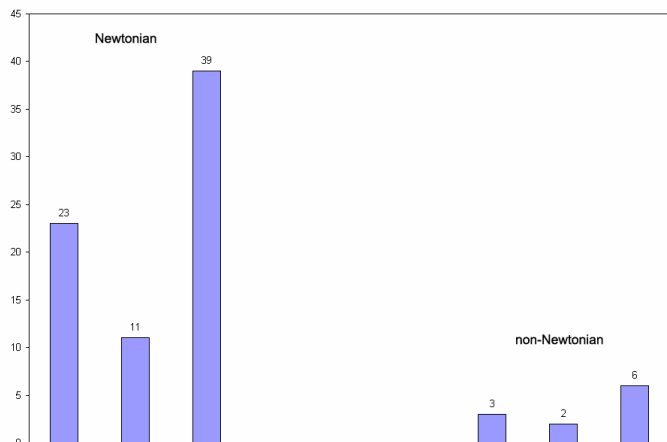


Figure 12 Percentage of total cellular area exposed to a wall shear stress below 0.5 Pa for both the Newtonian and non-Newtonian models. The bars represent, from left to right, instants A, B, and C.

CONCLUSIONS

The near-wall flow field within a stented arterial segment was investigated. Newtonian vs. non-Newtonian blood properties and steady vs. transient inlet conditions, within a three-dimensional and non-compliant model, were used. WSS levels differed significantly between Newtonian and non-Newtonian models as well as between steady and transient models. In all cases the WSS predicted by the non-Newtonian model was higher, but the discrepancy between both models was found to be time dependent. In addition, statistical moments were used to quantify the global difference in WSS distribution morphology between the Newtonian and non-Newtonian models. It was found that the Newtonian model under predicts WSS levels and yields WSS distributions with different morphology, which implies that a global correction factor might not be appropriate.

This work has shown that the non-Newtonian nature of blood affects the WSS distribution within a stented arterial segment considerably. In general, the WSS was always higher with the non-Newtonian model, which implies that the risk of restenosis can be significantly overestimated if the non-Newtonian nature of blood is neglected. The results presented in this work agree with those of Bernard *et al.* (Bernard *et al.* 2006). Unlike Bernard *et al.* a transient model has been used, which shows that the transient effects also affect the WSS in a non-Newtonian model. In fact, even when the instantaneous Reynolds number of a non-Newtonian model is matched the WSS distribution can significantly change depending on whether the fluid is accelerating or decelerating.

REFERENCES

Benard, N., Perrault, R., and Coisne, D. (2006). Computational Approach to Estimating the Effects of Blood Properties on Changes in Intra-stent Flow. *Annals of Biomedical Engineering*, V34(8), 1259-1271.

Chien, S., Usami, S., Taylor, H. M., Lundberg, J. L., and Gregersen, M. I. (1966). Effects of hematocrit and plasma proteins on human blood rheology at low shear rates. *J Appl Physiol*, 21(1), 81-7.

Duraiswamy, N., Schoepfoerster, R. T., Moreno, M. R., and Moore, J. E. (2007). Stented Artery Flow Patterns and Their Effects on the Artery Wall. *Annual Review of Fluid Mechanics*, 39(1), 357-382.

Gijsen, F. J., van de Vosse, F. N., and Janssen, J. D. (1999). The influence of the non-Newtonian properties of blood on the flow in large arteries: steady flow in a carotid bifurcation model. *Journal of biomechanics*, 32(6), 601-8.

Gladius, L. (2008). Materials, fluid dynamics, and solid mechanics aspects of coronary artery stents: A state-of-the-art review. *Journal of Biomedical Materials Research Part B: Applied Biomaterials*, 86B(2), 569-590.

Hara, H., Nakamura, M., Palmaz, J. C., and Schwartz, R. S. (2006). Role of stent design and coatings on restenosis and thrombosis. *Advanced Drug Delivery Reviews*, 58(3), 377-386.

Mejia, J., Mongrain, D. R., Leask, R., Rodes, J., and Bertrand, O. "The Significance of Flow Unsteadiness on the Near-Wall Flow of a Stented Artery." *4th European Congress for Medical and Biomedical Engineering*, Antwerp, Belgium.

Mejia, J., Mongrain, R., Ruzzeh, B., Leask, R., and Bertrand, O. F. (2009). Evaluation of the effect of stent strut profile on shear stress distribution using statistical moments. *Biomedical engineering online*, 8(1), 8.



Session 3A

Biomedicine - Biomolecule

Mr. Karel Vlasak

DEP Europe GmbH

Germany

Karel_v@depusa.com



“Parameterization and Optimization of Balloon Expandable Stent”

Karel Vlasak (1), Basant Sharma (2)

(1) DEP Europe GmbH, Stuttgart, Germany

(2) DEP Inc., Troy, Michigan, USA

Keywords: vascular stent, Finite element modeling

Summary:

Vascular stents are deployed in the blocked arteries to restore the passage of the blood flow. By acting as a mechanical scaffold, stenting is effective in preventing and treating coronary occlusion. The stent design activity aims at improved criteria like recoil and foreshortening.

Conventional design procedure wouldn't be able to tackle simultaneously the problems of recoil and foreshortening, and also it is quite time consuming. Whereas numerical simulations can be comfortably used to optimize stent design, allowing for consideration of competing solid mechanical concerns (recoil, foreshortening).

The paper discusses the use of such advanced technique to solve these problems. The paper would cover the essence of Finite Element Analysis, Parameterization and Optimization. Finite element modeling (FEM) is used to estimate stress distribution in the stent. Various parameters are identified for carrying out optimization. Different stent designs are generated using the morphing software available in the market. Optimization is carried out to identify best possible design.

TITLE

Subject-specific finite element model of a cementless femoral stem. A preliminary study.

AUTHORS

Valéry Barbour; Aurelien Courvoisier, M.D.; Michel Thourot; David Mitton, Ph.D.; Wafa Skalli, Ph.D.

Keywords:

Hip, Cementless, Finite Element, Subject-specific model, load transfer, Pressure measurements

ABSTRACT

Implants endurance as well as a good clinical tolerance depends on the recovery of a physiological stress distribution within bone after implantation. The purpose of the present work was to develop a subject-specific finite element model of a cementless stem to assess the immediate post-operative load transfer at the implant-bone interface. We developed an alternative technique using Force Sensing Resistors (FSR) to gather in vitro pressure values at this interface for a cementless implant. The stem was instrumented with six calibrated FSR bonded on each facet and then implanted in cadaver femur. A destructive compressive test was performed and FSR pressure values were recorded. The finite element models of the stem and the femur were meshed separately (Ansys 11.0) from the 3D model for the stem and from CT-Scan for the femur. The stem material properties were assumed to be an isotropic titanium alloy ($E= 110,000$ MPa and $\nu= 0.3$). A CT-based average elastic modulus of $10,239$ MPa was assigned to the femur ($\nu= 0.3$). Boundary conditions were applied according to the experimentation and implant-bone contact zones were obtained from EOS stereoradiographs (Biospace Med). The coefficient of friction used at the interface was 0.1 . 500 N load steps were simulated until obtaining the experimental failure load. The cartography of pressures obtained by the FEM corresponded to the local experimental variation. This model could allow optimizing new femoral cementless implants development and, by optimizing computing times and ergonomics, a preoperative help to choose the ideal stem supporting osteointegration and load transfer.

INTRODUCTION

Total hip replacement has proven to be a successful procedure. One of the complications of cemented femoral components is aseptic loosening that may result to a revision femoral arthroplasty. The main issue in femoral revision arthroplasty is to achieve a durable fixation despite the lack of appropriate femoral bone stock. Because of the poor durability of cemented fixation, cementless fixation has been widely used in revision (Engh, Ellis, et al., 2002; Paprosky and Burnett, 2002; Gosens and van Langelaan, 2005; Raman, Kamath, et al., 2005; Trikha, Singh, et al., 2005; Reikeras and Gunderson, 2006; Hamilton, Cashen, et al., 2007). The purpose of cementless fixation was initially to obtain bone ingrowth in order to fill the proximal femoral bone defect. The long term results reported in the literature show similar complications such as persistent thigh pain, stress-shielding and lack of ingrowth (Moreland and Moreno, 2001).

Evaluation of the implant-bone load transfer is a main concern in biomechanics of the implanted proximal femur. Few experimental studies on load transfer within the implant-bone interface have been described in the literature because of methodological difficulties (Sakai, Itoman, et al., 2006; Schneider, Kinast, et al., 1989). Many FE models of implanted cementless femoral stems suffer from absence of in vitro validation (Speirs, Heller, et al., 2007; Viceconti, Pancanti, et al., 2004; Weinans, Huiskes, et al., 1994; Namba, Keyak, et al., 1998). Validation of FE models of implanted femurs is usually based on the comparison of local strain measurements on the femur submitted to a static load to values obtained with the FE model in the same conditions. FE models of implanted femurs have been validated for cemented primary stems (Waide, Cristofolini, et al., 2003; Jeffers, Browne, et al., 2007; Completo, Fonseca, et al., 2007; Stolk, Verdonschot, et al., 2002; McNamara, Cristofolini, et al., 1997; Reggiani, Cristofolini, et al., 2007) and for cementless primary stems (Sakai, Itoman, et al., 2006; Reggiani, Cristofolini, et al., 2007) but none for cementless revision stems. Synthetic femurs have been commonly preferred to cadaveric specimens in order to decrease inter-specimen variability. Besides scientific considerations, inter-specimen variability is the day-to-day challenge of the orthopaedic surgeon. Subject-specific finite element models are necessary to combine accuracy of numeric investigations and clinical exigencies.

Thus, our aim was to develop a subject-specific finite element model of a cementless collared stem for femoral revision surgery to assess the immediate post-operative load transfer at the implant-femur interface in a femur with a Paprosky type II (Paprosky, Bradford, et al., 1994) bone defect configuration.

MATERIAL AND METHODS

1. Experimentation

A right femur from a 91 year-male cadaver was harvested fresh and stored at -20°C. The interval between death and harvesting was 90 days. The specimens were stored at 4°C before harvesting.

A long cementless collared femoral stem coated with hydroxyapatite was investigated (KAR; DePuy, France). Six force-sensing resistors (I.E.E. – FSR – 149) were bonded to the femoral stem subsequently coated with plastic adhesive to guarantee waterproof quality and permanent electrical continuity (Figure 1). The lead wires were laid in the grooves of the stem. Each FSR was calibrated before test for different load values. A relation between pressure and the output voltage was obtained. The in vitro insertion procedure was performed according to the protocol described for this type of stem. The cancellous bone was removed from the femoral cavity in order to create a type II of Paprosky bone defect classification. A transversal diaphyseal osteotomy was performed at 25 cm below the lesser trochanter. The femur was then potted in a steel box at 11° adduction and 4° of flexion. Destructive test was performed on the implanted femur with a loading machine (5500-R, Instron, Canton, MA, USA) at a constant displacement rate of 10 mm/min. Load was recorded via the load cell (Instron Load Cell 100 kN Static, Cat No 2518-201, Code 100, Instron, Canton, MA, USA) of the testing machine. Muscle forces were not simulated. During the destructive test, the event was filmed by means of two numeric cameras (Canon, Digital Video CamCorder MV901). FSR pressure values were recorded. Precise location of the stem and FSR sensors in the femur before and after fracture was obtained with stereoradiography system EOS (Biospace Med) on AP and lateral views.

2. Finite Element analysis

2.1. Solid model

2.1.1. The femur

The specimen was CT-Scanned immersed in water. The scanner setting was 140 kV, 206 mA, 17 s, spiral algorithm with a recalculated slice thickness of 1mm and a 512×512 pixel resolution. The dataset was calibrated using the European Spine Phantom(Kalender, 1992) assuming a linear relationship between Hounsfield Unit (HU) and bone density (Les, Keyak, et al., 1994)

CT datasets were segmented (Avizo 5.0, Mercury Computer Systems Inc., USA). Cancellous bone was not selected for the geometric model in order to obtain a type II Paprosky's configuration (Paprosky, Bradford, et al., 1994).

The precise location of the femoral neck osteotomy and the stem position and orientation in the femoral cavity were obtained from EOS stereo-radiographs and were spatially registered within EOS reference axis using Idef'X (Biospace Med).

Meshing was done under Ansys using 8 nodes-hexahedral elements (Solid 45). The femur was made of 1476 elements and 2295 nodes (Figure 2).

The isotropic and linear properties of the bone were considered. An average Young modulus was calculated using CT datasets. An average elastic modulus of 10,239 MPa was assigned to the femur. A Poisson ratio of 0.3 was assumed in all cases

2.1.2. The implant

The stem was meshed from the 3D model and adjusted in the femur using stereoradiographs. The neck and the distal part of the stem were meshed using 20 nodes hexahedrons (Solid 95). The collar was meshed using 20-node tetrahedrons (Solid 95). The stem model was made of 9836 hexahedrons (33862 nodes) and 23930 tetrahedrons (33514) (Figure 3). The material properties of the stem elements were assumed to be an isotropic titanium alloy with a Young Modulus of 110,000 MPa and a Poisson Ratio of 0.3. The stem was virtually impacted in the femur in order to fit the internal cortical at the first step by a self-developed program under Matlab.

2.2. Calculation

Boundary conditions were applied according to the experimental ones and implant-bone contact zones were obtained from EOS stereoradiographs. The distal part of the femur was bonded. The implant was loaded with a force applied to the centre of the prosthetic head at a direction and intensity identical to the experimentation (Figure 4).

The bone-implant contact and the contact between the distal slots were modelled using contact elements (Contact 174 and Target 170). The coefficient of friction used was 0.1 (Sakai, Itoman, et al., 2006) between the stem and the internal cortical.

A static calculation was conducted under Ansys 11.0 Classic. A first step with no load was applied in order to adjust contacts between solids and to suppress any nodes' interpenetrations. Then, 500 N load steps were applied until obtaining the experimental failure load (5500 N)

2.3. Measures

The deformed shapes of the femur and the stem, collar/ calcar contacts and the contact pressure at the bone interface were compared to the values measured experimentally.

RESULTS

Results refer to the loading step corresponding to the fracture obtained during the experimentation (5500 N).

1. Deformed Shape

The global displacement for the implant is about 14.82 mm and 6.57 mm for the femur. The collar is in contact with the calcar.

(Figure 5, Figure 6, Figure 7)

2. Effort – Displacement

The effort-displacement curve is quite linear until collar-calcar contact. After contact, effort increases at a constant displacement.

(Figure 8)

2.1. Contact areas on the stem

Contacts were mainly applied on the antero-lateral side and the intermediate medial part of the stem.

(Figure 9, Figure 10, Figure 11)

2.2. Contact areas on the bone

Contact pressure has reached 1.34 MPa in the zone located at the top of the FSR 3 and in lower part of the FSR 5.

(Figure 12, Figure 13, Figure 14)

The pressure-displacement curve increases until collar-calcar contact. A depression is then observed when contact occurred.

2.3. Von Mises Stress

The maximum Von Mises stress is obtained in visu on the implant and the femur with respectively 1252 MPa and 480 MPa. The value obtained on the femur is higher than the acceptable compression limit of the cortical bone (205 MPa).

(Figure 15, Figure 16, Figure 17, Figure 18)

DISCUSSION

The purpose of this preliminary study was to develop a patient-specific FE model of the proximal femur implanted with a cementless collared stem and to verify the accuracy with which this model predicts the bone–implant contact pressure.

Implanted femur FE models are generated through different modalities in the literature. Stem geometry is usually obtained from the 3D-model provided by the manufacturer. Femur geometry is either standardized for synthetic femur or obtained from CT-scan data. Implanted femur model geometry is therefore obtained after numeric implantation or from CT-scan of the in vitro or in vivo implanted femurs (Viceconti, Brusi, et al., 2006).

The concept of subject-specific models takes in account inter-individual variability which excludes synthetic bones utilization. Biomechanical properties of synthetic femurs have been validated but they do not represent the real biological response and the anatomic variability of natural femurs. In addition, FE models for medical use need to be validated in vitro which is not necessarily done for FE models described in the literature. In this study, a FE model was obtained from the CT-scan data of an intact femur and the stem geometry. A numerical implantation of the prosthesis was realized in accordance with the surgical procedure. The size and position of the prosthesis were guided by the in vitro experimentation data. Mechanical properties of the femur were implemented in the FE model using gray-scale-to-bone density relationship with a methodology previously described (Les, Keyak, et al., 1994; Duchemin, Bousson, et al., 2008).

In vitro experimentations on implanted proximal femur are commonly based on strain measurements with strain gauges bonded on the femur or embedded in the cement mantle. Primary fixation of cementless stems has been poorly investigated in vitro. Applying sensors within the implant-bone interface has not been achieved without damaging the femur structure, which could explain the low reproducibility of the measurements (Sakai, Itoman, et al., 2006; Schneider, Kinast, et al., 1989). Our measurements were achieved with respect to the femur structure with realistic implantation conditions. This is a unique experimental protocol using FSR sensors within the implant-bone interface. FSR has provided tangible data on local contact pressures. Their low profile has allowed their implantation but their small active area has limited the surface of measurement. However, they enabled comparison with the FE models. The idea of pressure-sensitive films developed by Sakai et al for a wider surface of measurement was seducing but technically impossible without bisecting the femur.

Primary fixation of the implant in the femur cavity greatly influences the load transfer and location of maximum stress areas in the femur and in the implant. Primary fixation depends

on the stem position in the femur, which belongs to its geometry and the anatomic variations of the femurs. Stress-shielding is defined by the absence of load transfer in the proximal part of the femur after implantation of a femoral stem which contributes to bone resorption and subsequently to aseptic loosening (Huiskes, Weinans, et al., 1992; Decking, Puhl, et al., 2006). Femurs were deliberately set in a type II bone defect configuration so the proximal part of the femur was contact free. The long cementless stem studied here is typically indicated in this type of moderate proximal bone loss. Here, the femurs were all *a priori* subjected to stress-shielding. The FE model confirmed the absence of contact within the proximal part of the femur throughout loading (Figure 17, Figure 18).

Patterns of stress repartition for cementless implants have been modeled in FE (Speirs, Heller, et al., 2007; Viceconti, Brusi, et al., 2006; Crowninshield, Maloney, et al., 2004). FE models on cementless femoral implants which assume the implant fully bonded are not realistic before bone remodeling (Speirs, Heller, et al., 2007; McNamara, Cristofolini, et al., 1997). In this study, the proximal femoral metaphysis was always contact free which match the desired type II configuration. Stereoradiographs interpretation showed a great inter-individual variability of the contact zones repartition. The distal anterior and medial sides of the stem are contact free after implantation. The press-fit diaphyseal primary fixation is therefore not homogeneous but the stem is cantilevered between three points.

The cartography of pressures obtained by the FE model corresponds to the local experimental variation. The zero value obtained by the FSR 3 seemed incoherent and let suggest a failure of the sensor. The FE model that shows an important contact in the zone of this sensor confirmed this failure.

Penetration of the implant in the femur induces a compression of the bone with values of stresses higher than the resistance at rupture of the cortical bone in compression (205 MPa). Thus, the femur is compressed and micro cracks appeared on the internal cortical.

The zone of maximum stress on the femur well appears on the FE model in the zone of rupture of the femur during the experimentation.

The fracture started alongside the internal cortical before the contact of the flange. Once the contact established, the growth of a second peak of stress on the calcar induced the propagation of a crack between these two points.

(Figure 19, Figure 20)

The maximum stress on the implant was measured on the level of the slots. The long slot closed whereas the small one did not move as well from a radiographic point of view as on the FE model. The loading produced important residual stresses around the slots. The tested stem was then tested following fatigue standard (ISO 7206-4: 2002). In that condition, the

stem could not hold and the long slot broke after 55000 cycles at 330 daN in fatigue whereas a new implant carries out 10 million cycles without rupture at this level.

The effort-displacement curve obtained numerically presented slopes at the origin and after contact of the collar similar (80%) to those of the experimentation. However, on the experimental curve a plastic stage not visualized on the digital model was observed. That comes from the fact that the model did not use an elastoplastic material for the femur. Otherwise, elements having a constraint higher than working stress in compression (205 MPa for the cortical bone) would have plasticized.

(Figure 21)

Values obtained by FSR have confirmed radiographic interpretations and has allowed evaluating the FE model. Zones without contact (FSR 1, 2 and 5) were lightly charged during experimentation and also in the FE model.

FSR 3 and 4 were gradually put in load with the sinking of the stem. A great variability in contact pressures was observed within the same femur at the same load time. These experimental values obtained during a test with rupture do not correspond to a clinical situation where bone bridges are created between the implant and the internal cortical. The variability of the amplitudes and the distribution of the pressures within the interface bone-implant corroborate the results of Sakai et al. (Sakai, Itoman, et al., 2006). FSR values have to be carefully interpreted (Hall, Desmoulin, et al., 2008).

(Figure 22)

The sinking of the stem has allowed a contact of the collar with the calcar. The pressure has decreased on FSR 4 during the experimentation but also on the numerical results in the zone located at the top of FSR 3. The influence of the flange was already analyzed in FE studies and would allow an increase in the transfer of charge (Mandell, Carter, et al., 2004). The results obtained here bring tangible numerical data on the influence of the collar and the modification of the distribution of pressures that the FE model confirms. The calcar becomes an additional zone of load transfer, which allows the pressure decrease on the distal zones. Intuitively, this transfer of charge on the proximal femur could improve bone ingrowth but clinical studies did not show this discounted effect (Meding, Ritter, et al., 1997). Moreover, obtaining a contact between the collar and the calcar at the impaction of a cementless stem seems difficult (Meding, Ritter, et al., 1997).

(Figure 23, Figure 14)

The objective of this preliminary study was to improve comprehension load transfer within the bone-implant interface by creating a subject-specific FE model of the established femur. The experimentation has allowed bringing quantitative information on contact pressures between

the implant and the femur thanks to an innovating method. These measurements were obtained under realistic conditions by respecting the integrity of the structure of the femur. Data from sensors combined with the study of EOS radiographies had allowed correlating calculations in finite elements. Results underline great variability inter and intra-individual of the distribution of contact pressures in the studied configuration. These results can explain the interindividual variance of bone ingrowth after the implantation of cementless femoral stems. The FE model will have to be simulated for all experiments to be validated. It will thus make possible to better apprehend the load transfer at the bone-implant interface. The modification of the geometrical parameters and material of the prosthesis within the model should allow optimizing the performances of the implant. This model could thus become an essential base in the development of new femoral implants of a more important longevity. It could, moreover, by optimizing the computing times and ergonomics, become a preoperative help for surgeons in order to choose the ideal stem supporting osteointegration and load transfer.

Acknowledgments

Paediatric radiology department – Trousseau Hospital. Pierre et Marie Curie University Paris 6.

Anatomy Laboratory – René Descartes University. Paris 5

REFERENCES

- C. A. Engh, Jr., T. J. Ellis, L. M. Koralewicz, J. P. McAuley and C. A. Engh, Sr., 2002, Extensively porous-coated femoral revision for severe femoral bone loss: minimum 10-year follow-up, *J Arthroplasty* 17 (8), 955-960.
- W. G. Paprosky and R. S. Burnett, 2002, Extensively porous-coated femoral stems in revision hip arthroplasty: rationale and results, *Am J Orthop* 31 (8), 471-474.
- T. Gosens and E. J. van Langelaan, 2005, Clinical and radiological outcome of hydroxyapatite-coated femoral stem in revision hip arthroplasty, *Int Orthop* 29 (4), 219-223.
- R. Raman, R. P. Kamath, A. Parikh and P. D. Angus, 2005, Revision of cemented hip arthroplasty using a hydroxyapatite-ceramic-coated femoral component, *J Bone Joint Surg Br* 87 (8), 1061-1067.
- S. P. Trikha, S. Singh, O. W. Raynham, J. C. Lewis, P. A. Mitchell and A. J. Edge, 2005, Hydroxyapatite-ceramic-coated femoral stems in revision hip surgery, *J Bone Joint Surg Br* 87 (8), 1055-1060.
- O. Reikeras and R. B. Gunderson, 2006, Excellent results with femoral revision surgery using an extensively hydroxyapatite-coated stem: 59 patients followed for 10-16 years, *Acta Orthop* 77 (1), 98-103.
- W. G. Hamilton, D. V. Cashen, H. Ho, R. H. Hopper, Jr. and C. A. Engh, 2007, Extensively porous-coated stems for femoral revision: a choice for all seasons, *J Arthroplasty* 22 (4 Suppl 1), 106-110.
- J. R. Moreland and M. A. Moreno, 2001, Cementless femoral revision arthroplasty of the hip: minimum 5 years followup, *Clin Orthop Relat Res* (393), 194-201.
- R. Sakai, M. Itoman and K. Mabuchi, 2006, Assessments of different kinds of stems by experiments and FEM analysis: appropriate stress distribution on a hip prosthesis, *Clin Biomech (Bristol, Avon)* 21 (8), 826-833.
- E. Schneider, C. Kinast, J. Eulenberger, D. Wyder, G. Eskilsson and S. M. Perren, 1989, A comparative study of the initial stability of cementless hip prostheses, *Clin Orthop Relat Res* (248), 200-209.
- A. D. Speirs, M. O. Heller, W. R. Taylor, G. N. Duda and C. Perka, 2007, Influence of changes in stem positioning on femoral loading after THR using a short-stemmed hip implant, *Clin Biomech (Bristol, Avon)* 22 (4), 431-439.
- M. Viceconti, A. Pancanti, M. Dotti, F. Traina and L. Cristofolini, 2004, Effect of the initial implant fitting on the predicted secondary stability of a cementless stem, *Med Biol Eng Comput* 42 (2), 222-229.
- H. Weinans, R. Huiskes and H. J. Grootenboer, 1994, Effects of fit and bonding characteristics of femoral stems on adaptive bone remodeling, *J Biomech Eng* 116 (4), 393-400.
- R. S. Namba, J. H. Keyak, A. S. Kim, L. P. Vu and H. B. Skinner, 1998, Cementless implant composition and femoral stress. A finite element analysis, *Clin Orthop Relat Res* (347), 261-267.
- V. Waide, L. Cristofolini, J. Stolk, N. Verdonschot and A. Toni, 2003, Experimental investigation of bone remodelling using composite femurs, *Clin Biomech (Bristol, Avon)* 18 (6), 523-536.
- J. R. Jeffers, M. Browne, A. B. Lennon, P. J. Prendergast and M. Taylor, 2007, Cement mantle fatigue failure in total hip replacement: experimental and computational testing, *J Biomech* 40 (7), 1525-1533.
- A. Completo, F. Fonseca and J. A. Simoes, 2007, Experimental validation of intact and implanted distal femur finite element models, *J Biomech* 40 (11), 2467-2476.
- J. Stolk, N. Verdonschot, L. Cristofolini, A. Toni and R. Huiskes, 2002, Finite element and experimental models of cemented hip joint reconstructions can produce similar bone and cement strains in pre-clinical tests, *J Biomech* 35 (4), 499-510.
- B. P. McNamara, L. Cristofolini, A. Toni and D. Taylor, 1997, Relationship between bone-prosthesis bonding and load transfer in total hip reconstruction, *J Biomech* 30 (6), 621-630.

- B. Reggiani, L. Cristofolini, E. Varini and M. Viceconti, 2007, Predicting the subject-specific primary stability of cementless implants during pre-operative planning: preliminary validation of subject-specific finite-element models, *J Biomech* 40 (11), 2552-2558.
- W. G. Paprosky, M. S. Bradford and T. I. Younger, 1994, Classification of bone defects in failed prostheses, *Chir Organi Mov* 79 (4), 285-291.
- W. A. Kalender, 1992, A phantom for standardization and quality control in spinal bone mineral measurements by QCT and DXA: design considerations and specifications, *Med Phys* 19 (3), 583-586.
- C. M. Les, J. H. Keyak, S. M. Stover, K. T. Taylor and A. J. Kaneps, 1994, Estimation of material properties in the equine metacarpus with use of quantitative computed tomography, *J Orthop Res* 12 (6), 822-833.
- M. Viceconti, G. Brusi, A. Pancanti and L. Cristofolini, 2006, Primary stability of an anatomical cementless hip stem: a statistical analysis, *J Biomech* 39 (7), 1169-1179.
- L. Duchemin, V. Bousson, C. Raossanaly, C. Bergot, J. D. Laredo, W. Skalli and D. Mitton, 2008, Prediction of mechanical properties of cortical bone by quantitative computed tomography, *Med Eng Phys* 30 (3), 321-328.
- R. Huiskes, H. Weinans and B. van Rietbergen, 1992, The relationship between stress shielding and bone resorption around total hip stems and the effects of flexible materials, *Clin Orthop Relat Res* (274), 124-134.
- R. Decking, W. Puhl, U. Simon and L. E. Claes, 2006, Changes in strain distribution of loaded proximal femora caused by different types of cementless femoral stems, *Clin Biomech (Bristol, Avon)* 21 (5), 495-501.
- R. D. Crowninshield, W. J. Maloney, D. H. Wentz and D. L. Levine, 2004, The role of proximal femoral support in stress development within hip prostheses, *Clin Orthop Relat Res* (420), 176-180.
- R. S. Hall, G. T. Desmoulin and T. E. Milner, 2008, A technique for conditioning and calibrating force-sensing resistors for repeatable and reliable measurement of compressive force, *J Biomech* 41 (16), 3492-3495.
- J. A. Mandell, D. R. Carter, S. B. Goodman, D. J. Schurman and G. S. Beaupre, 2004, A conical-collared intramedullary stem can improve stress transfer and limit micromotion, *Clin Biomech (Bristol, Avon)* 19 (7), 695-703.
- J. B. Meding, M. A. Ritter, E. M. Keating and P. M. Faris, 1997, Comparison of collared and collarless femoral components in primary uncemented total hip arthroplasty, *J Arthroplasty* 12 (3), 273-280.

Figure 1

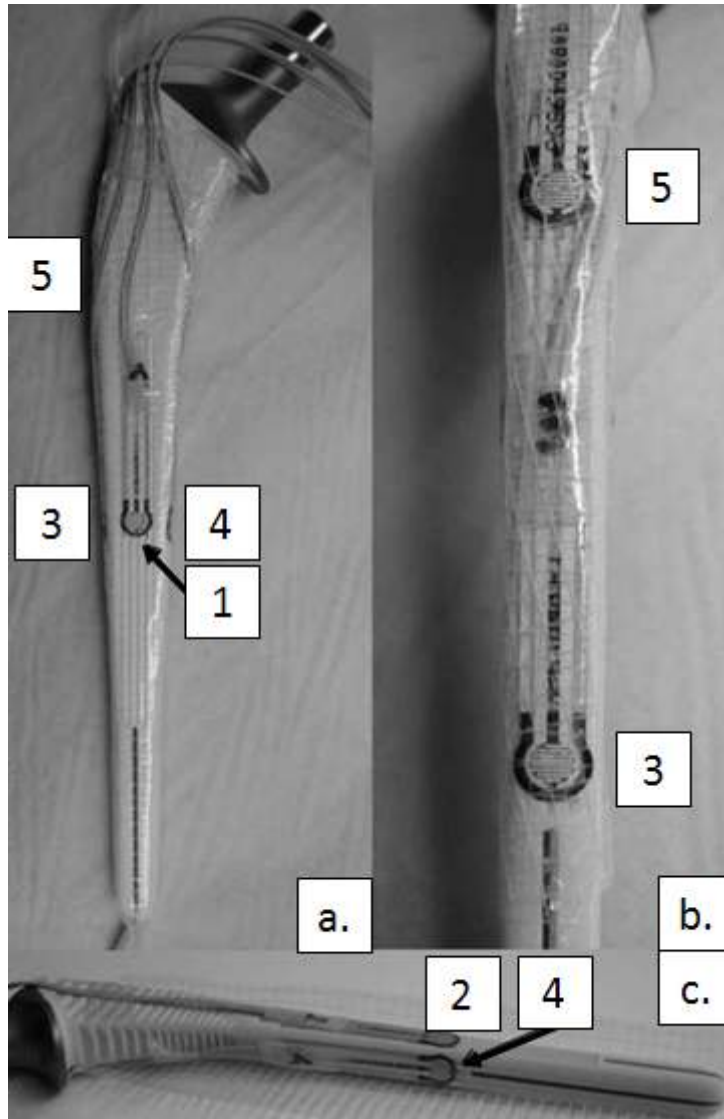


Figure 2

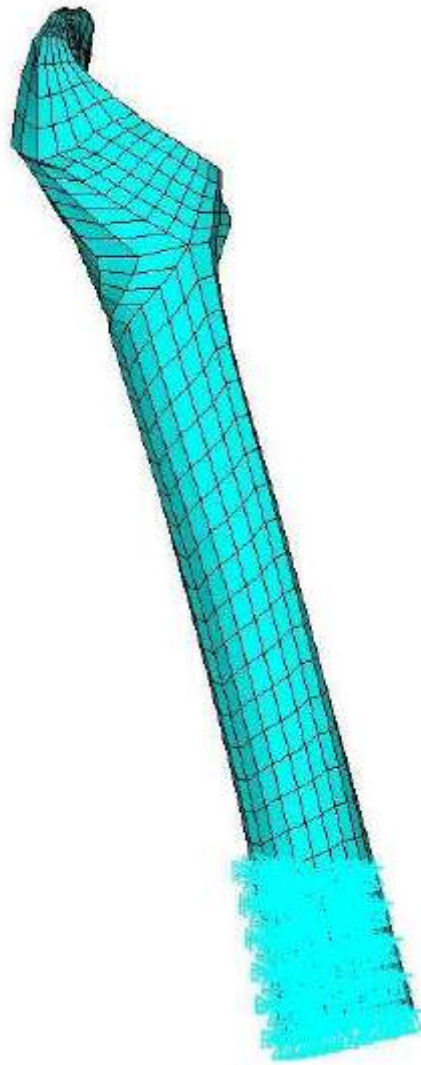


Figure 3

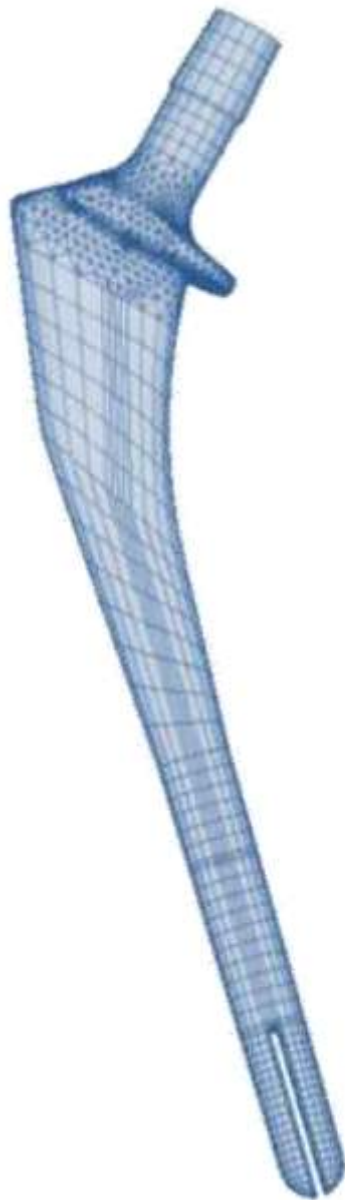


Figure 4

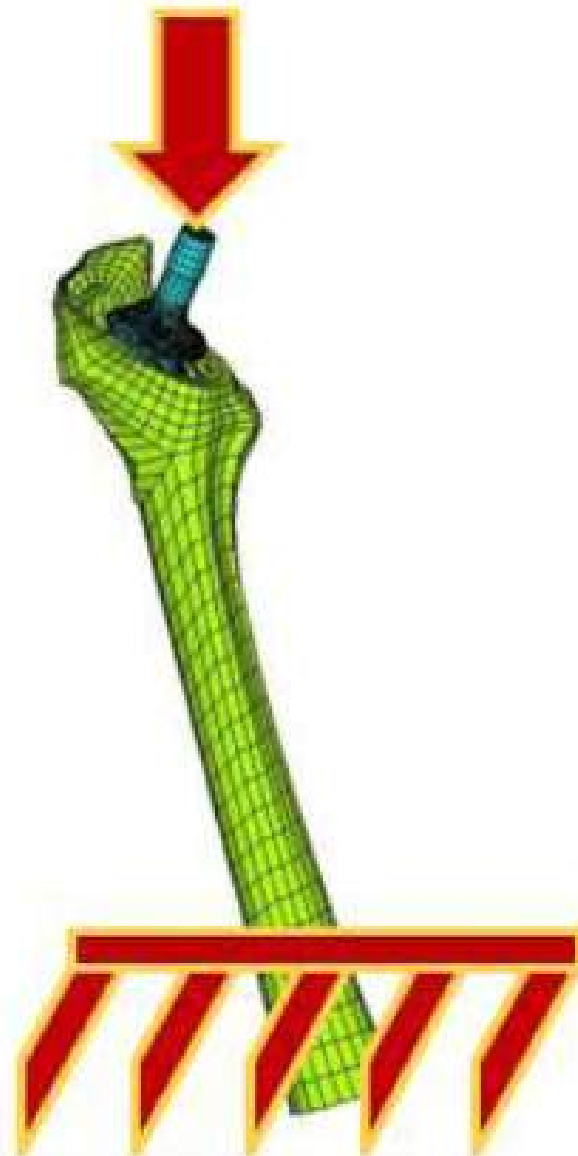


Figure 5

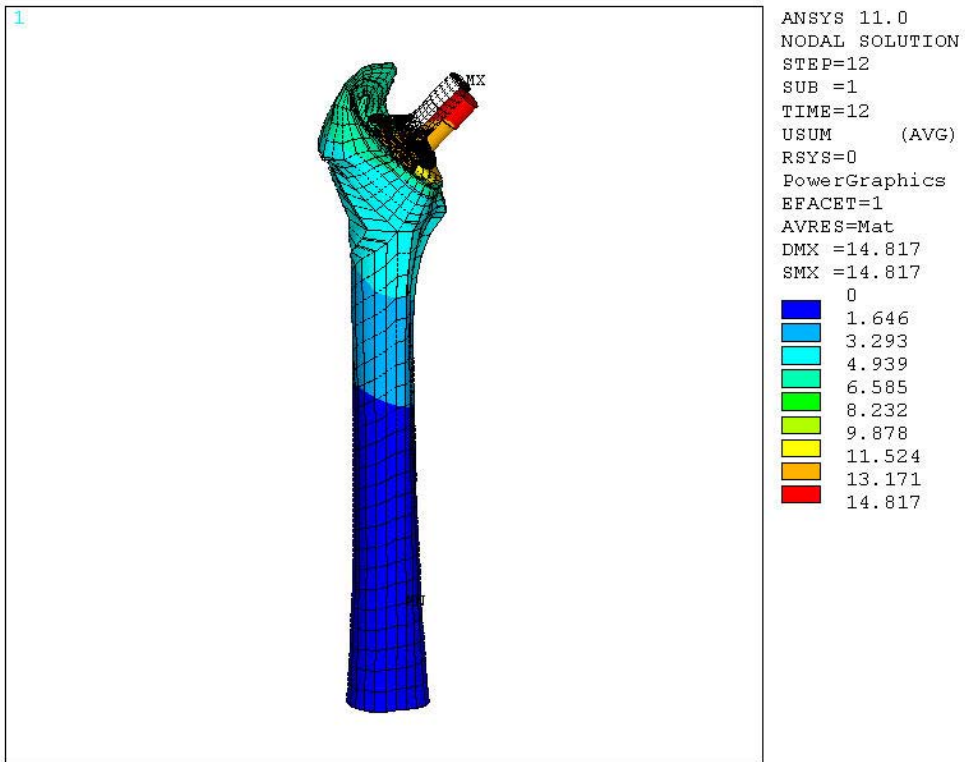


Figure 6

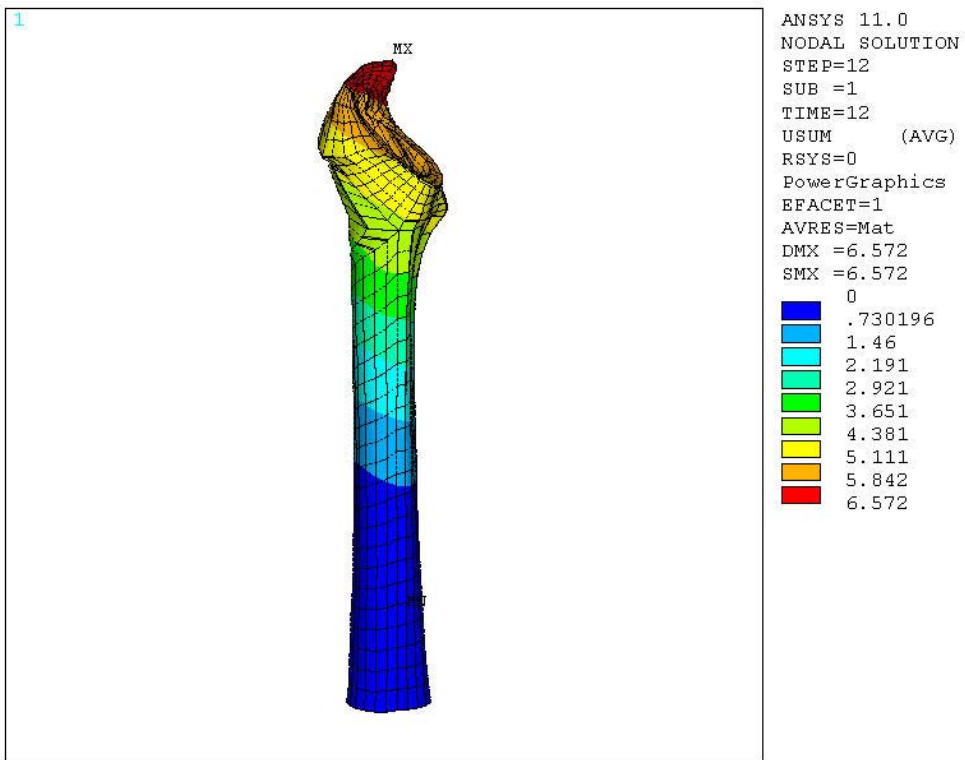


Figure 7

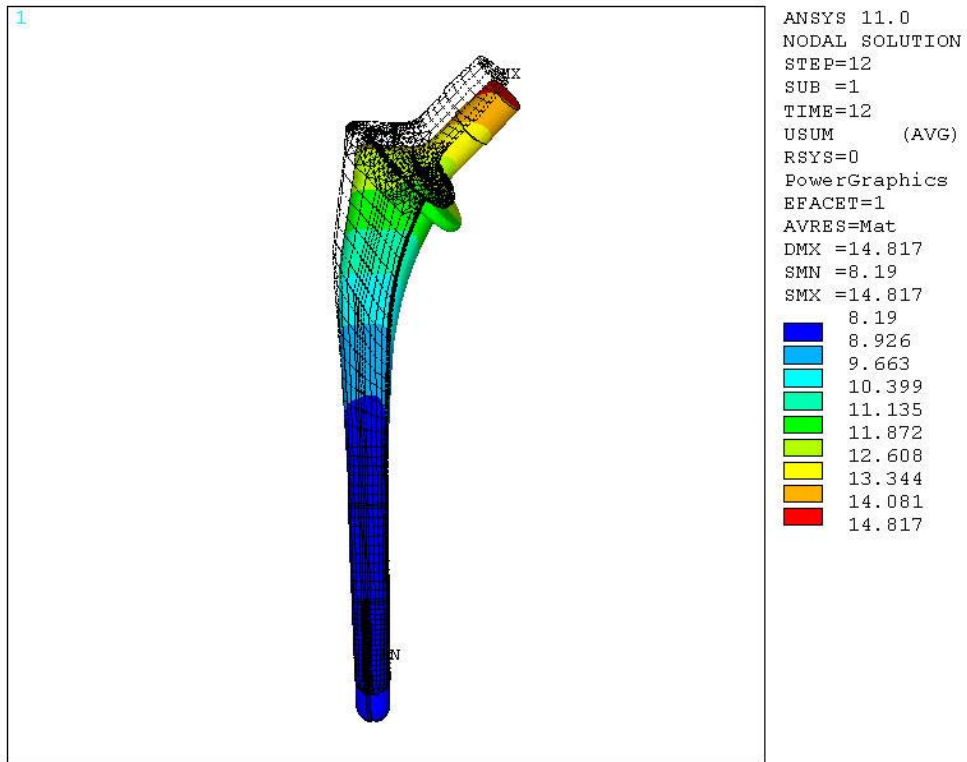


Figure 8

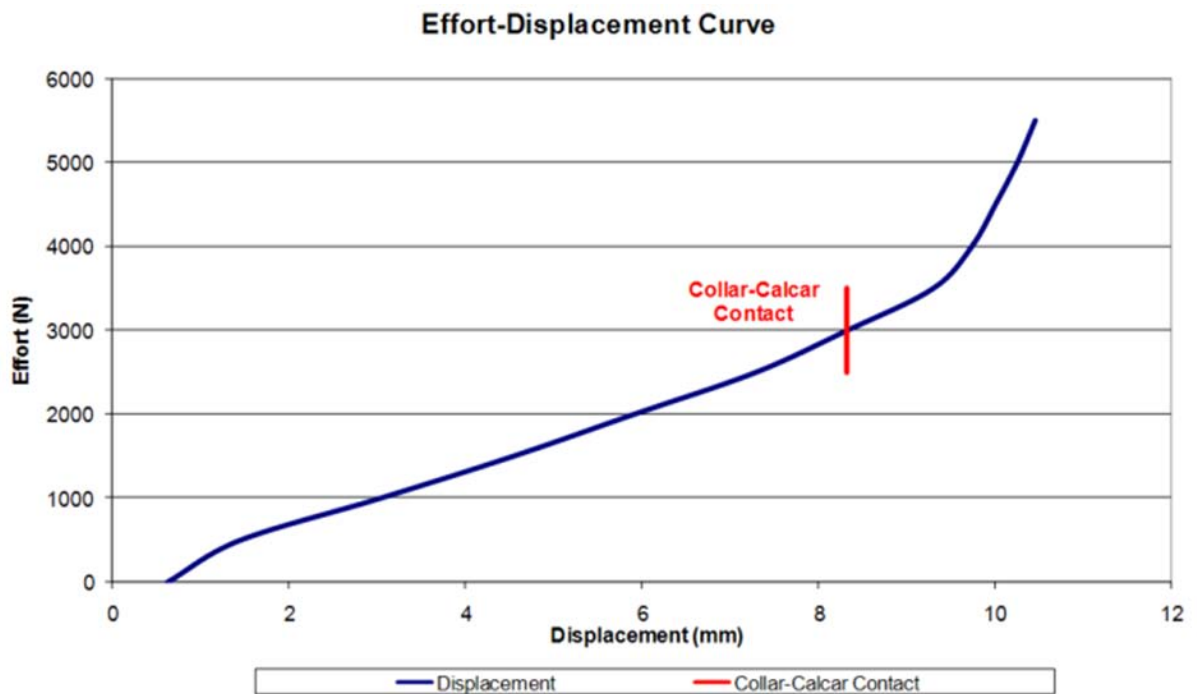
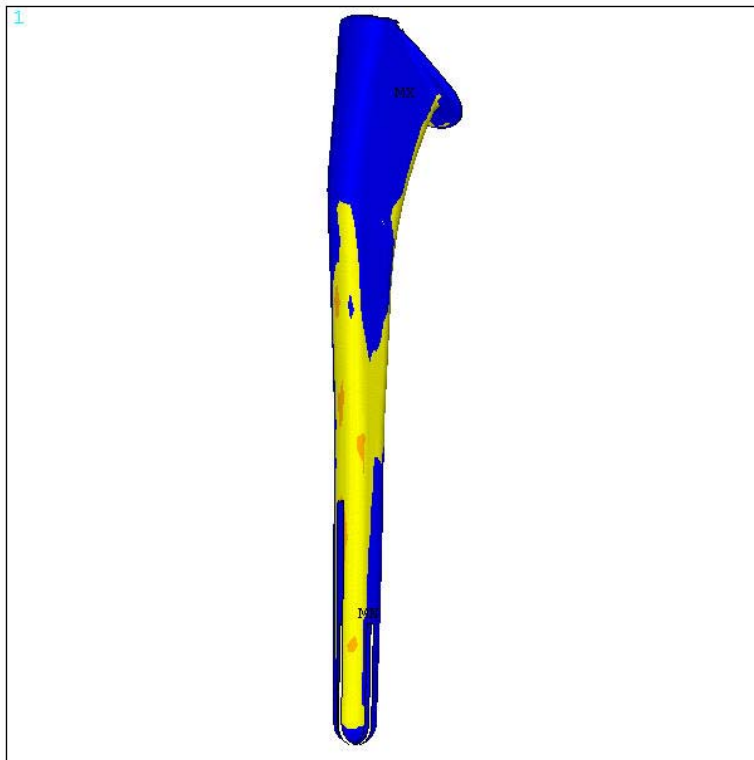


Figure 9

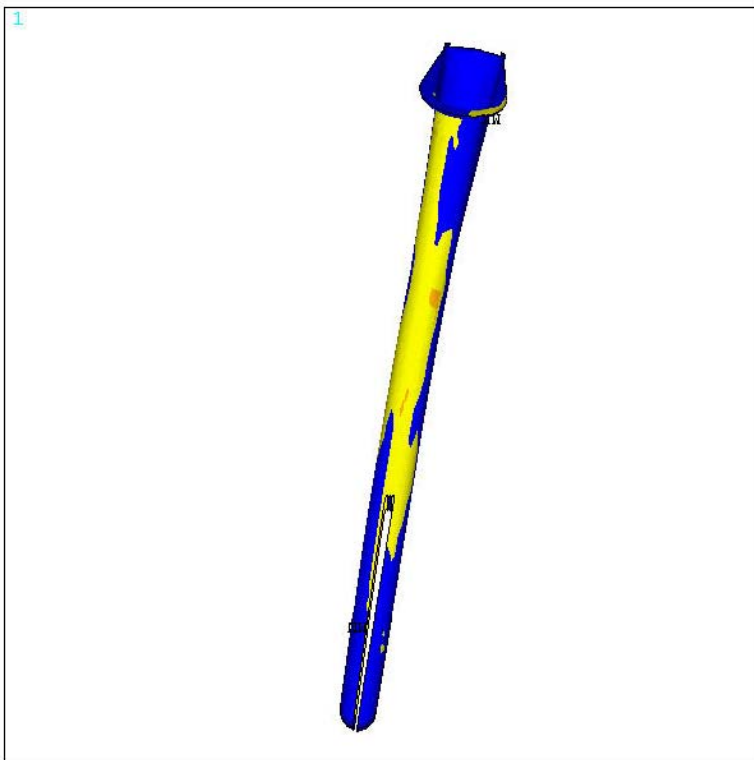


ANSYS 11.0
NODAL SOLUTION
STEP=12
SUB =1
TIME=12
CONTSTAT (AVG)
RSYS=0
PowerGraphics
EFACET=1
AVRES=Mat
DMX =13.481
SMX =2.2

XV =.740958
YV =-.655979
ZV =-.143778
*DIST=93.145
*XF =37.986
*YF =-30.182
*ZF =228.342
A-ZS=-115.728
Z-BUFFER

FarOpen
NearContact
Sliding

Figure 10



ANSYS 11.0
NODAL SOLUTION
STEP=12
SUB =1
TIME=12
CONTSTAT (AVG)
RSYS=0
PowerGraphics
EFACET=1
AVRES=Mat
DMX =13.481
SMX =2.2

FarOpen
NearContact
Sliding

Figure 11

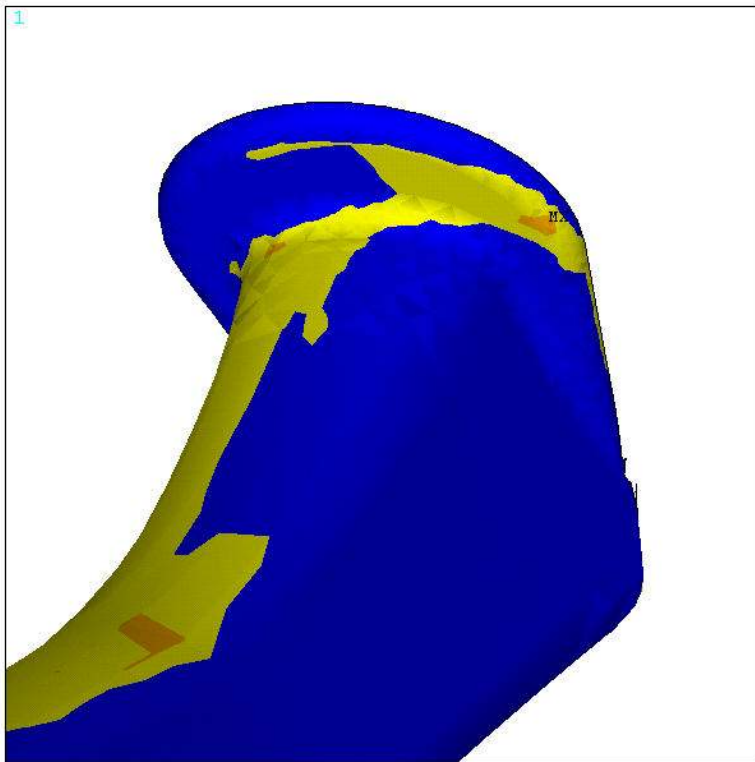


Figure 12

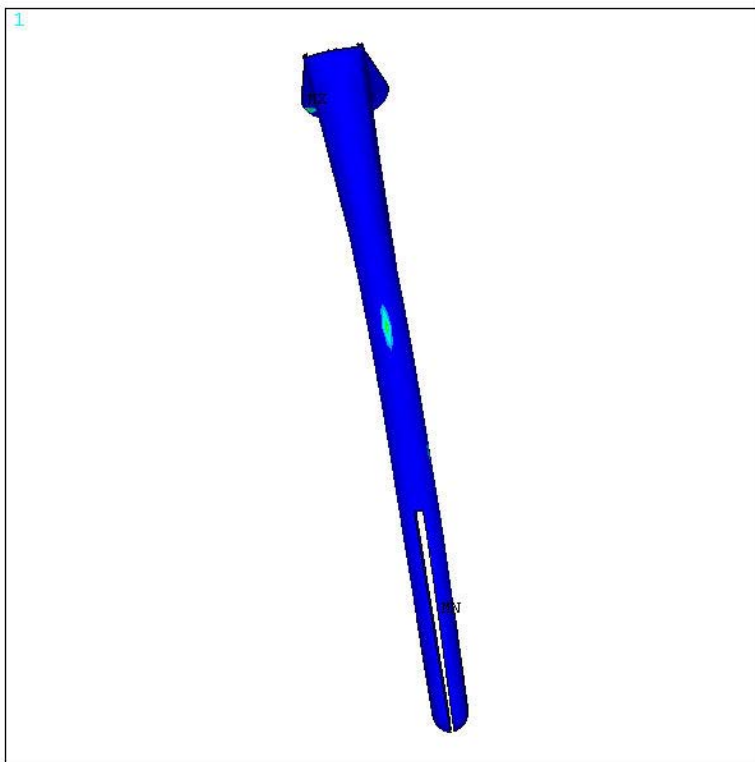


Figure 13

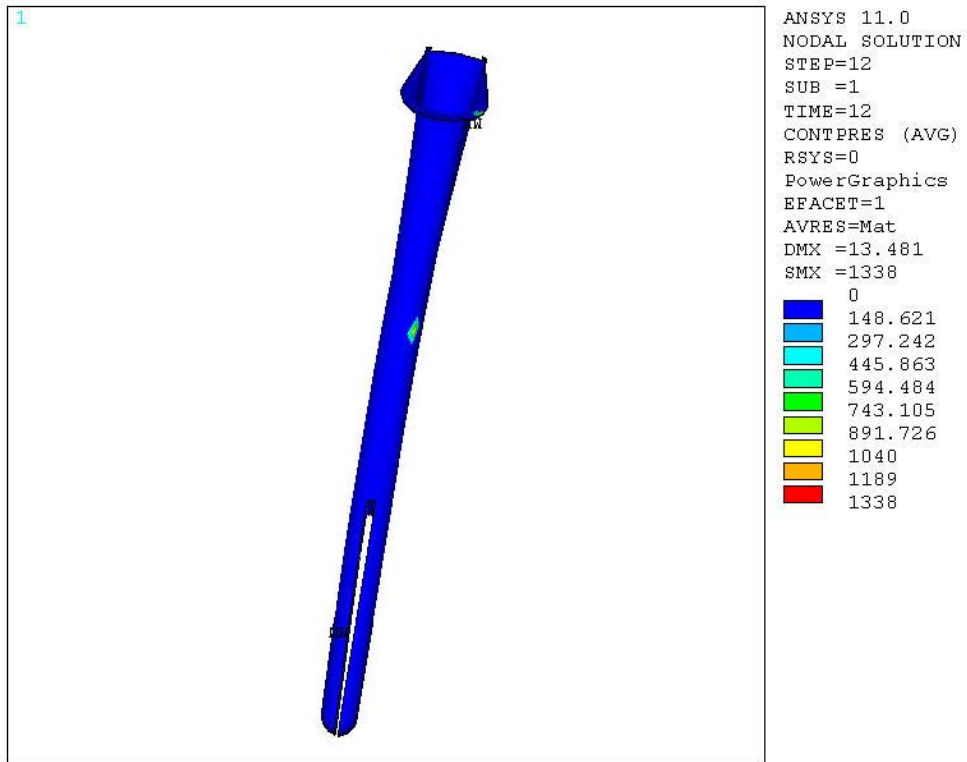


Figure 14

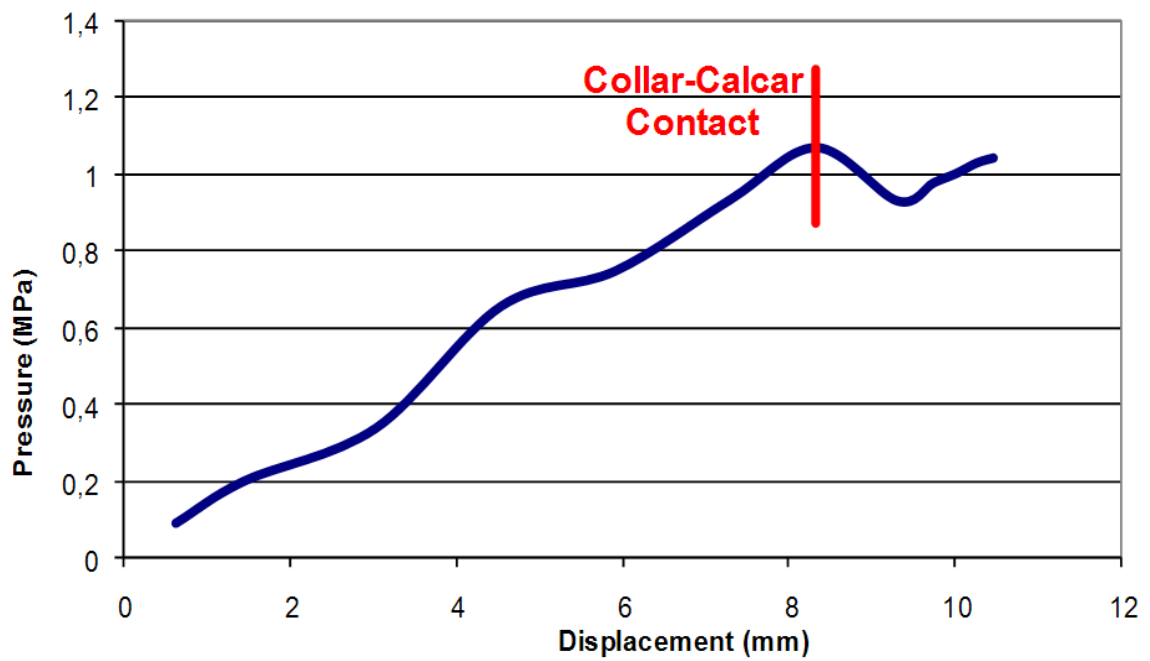


Figure 15

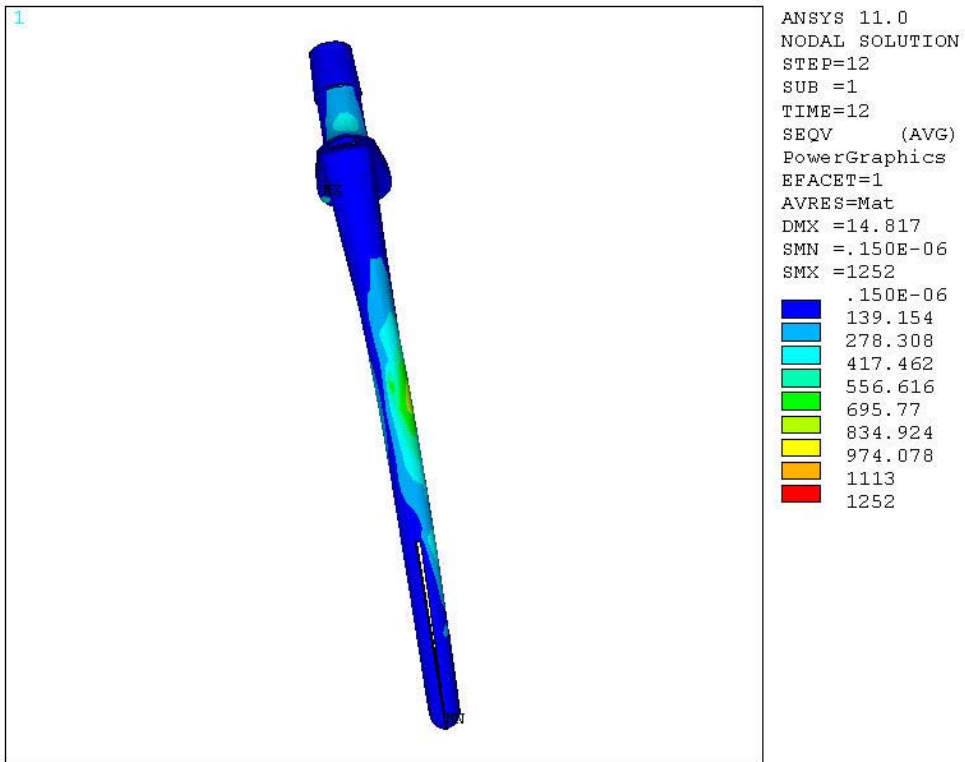


Figure 16

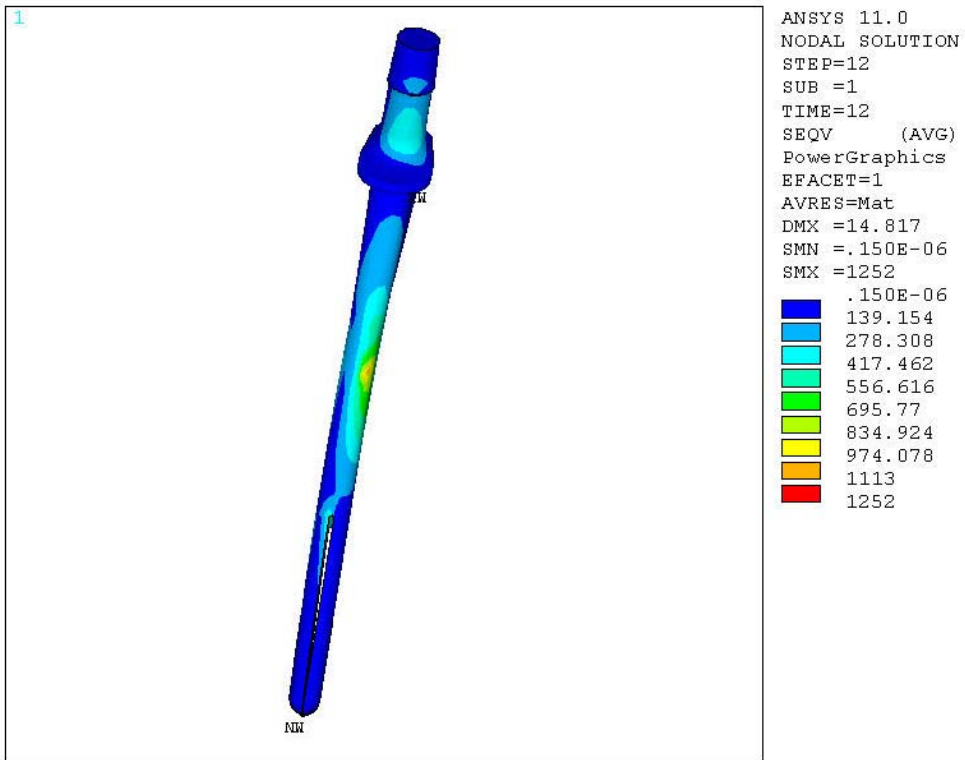


Figure 17

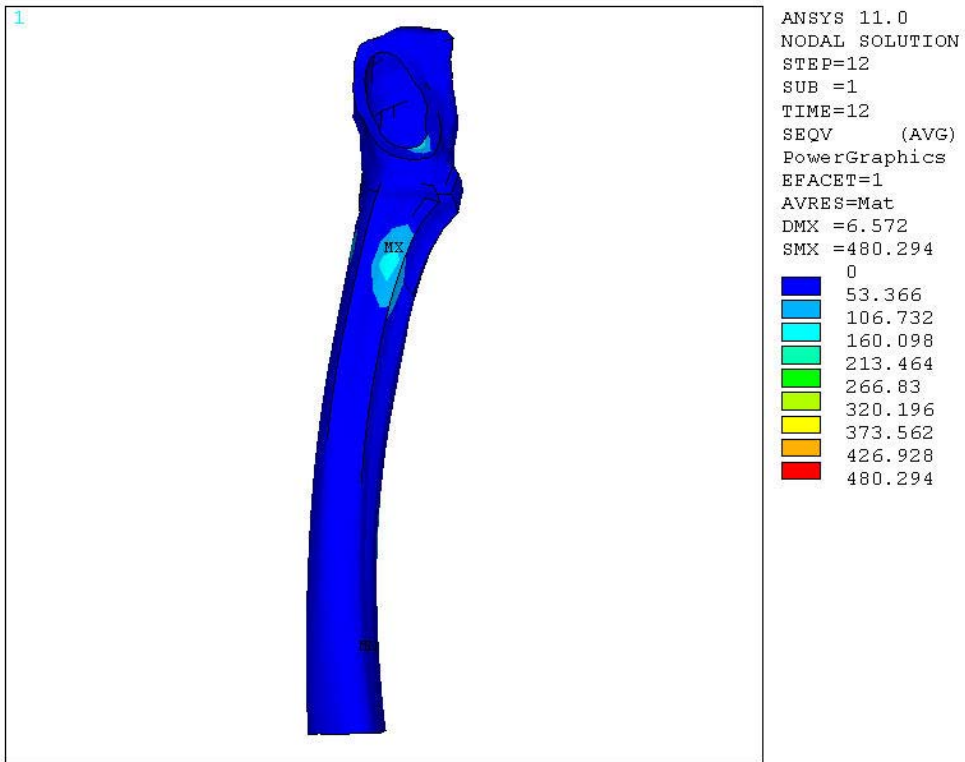


Figure 18

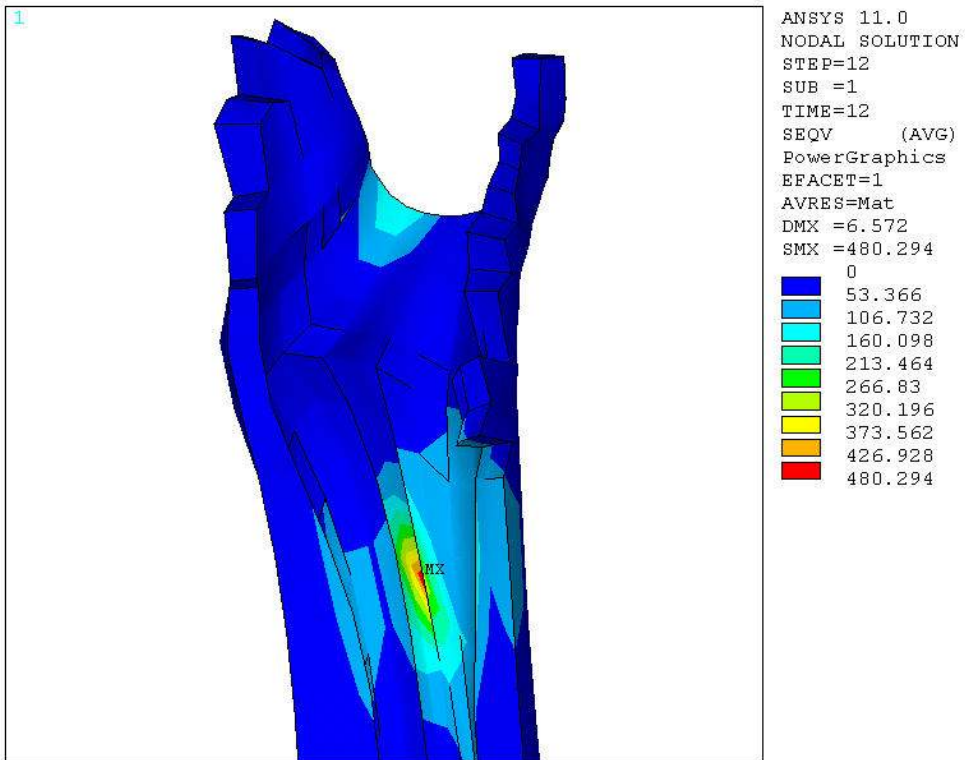


Figure 19

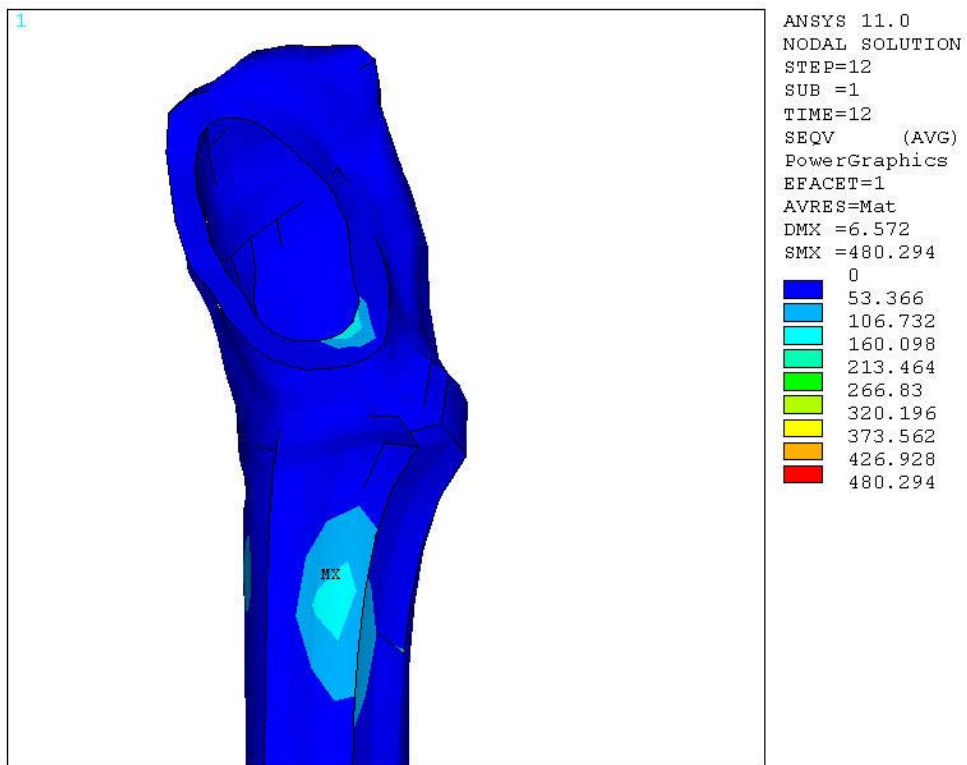


Figure 20

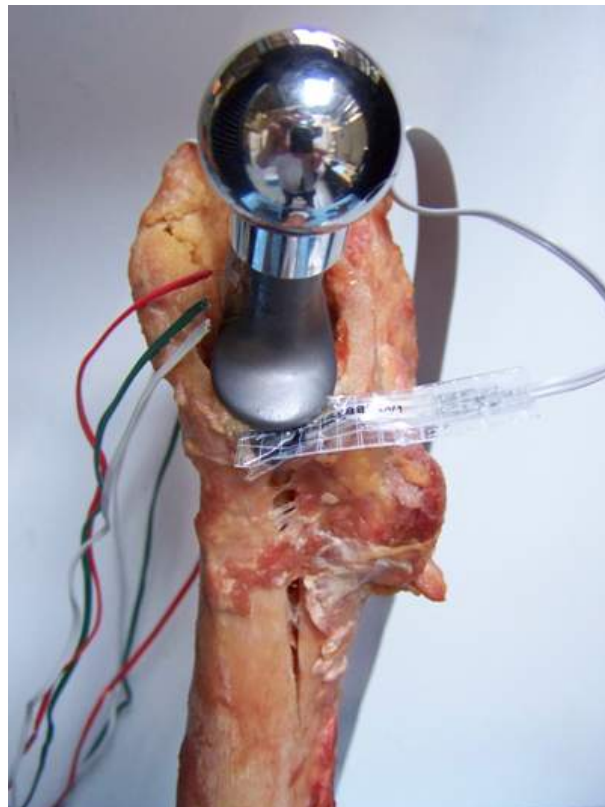


Figure 21

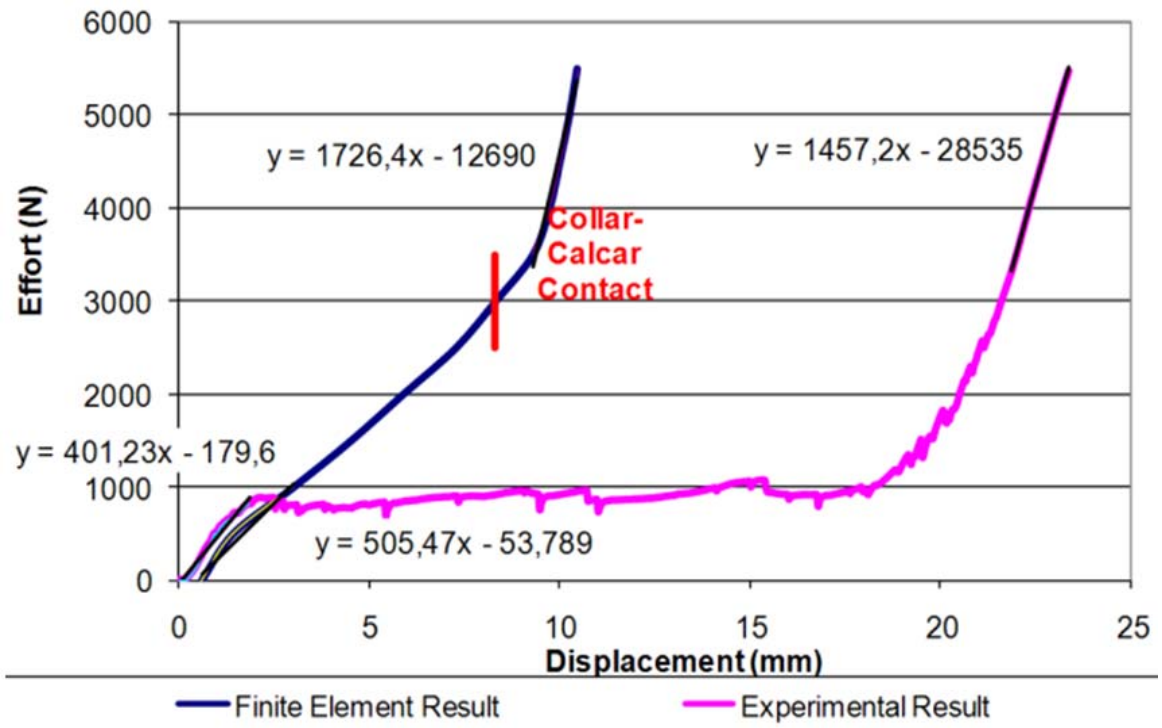


Figure 22

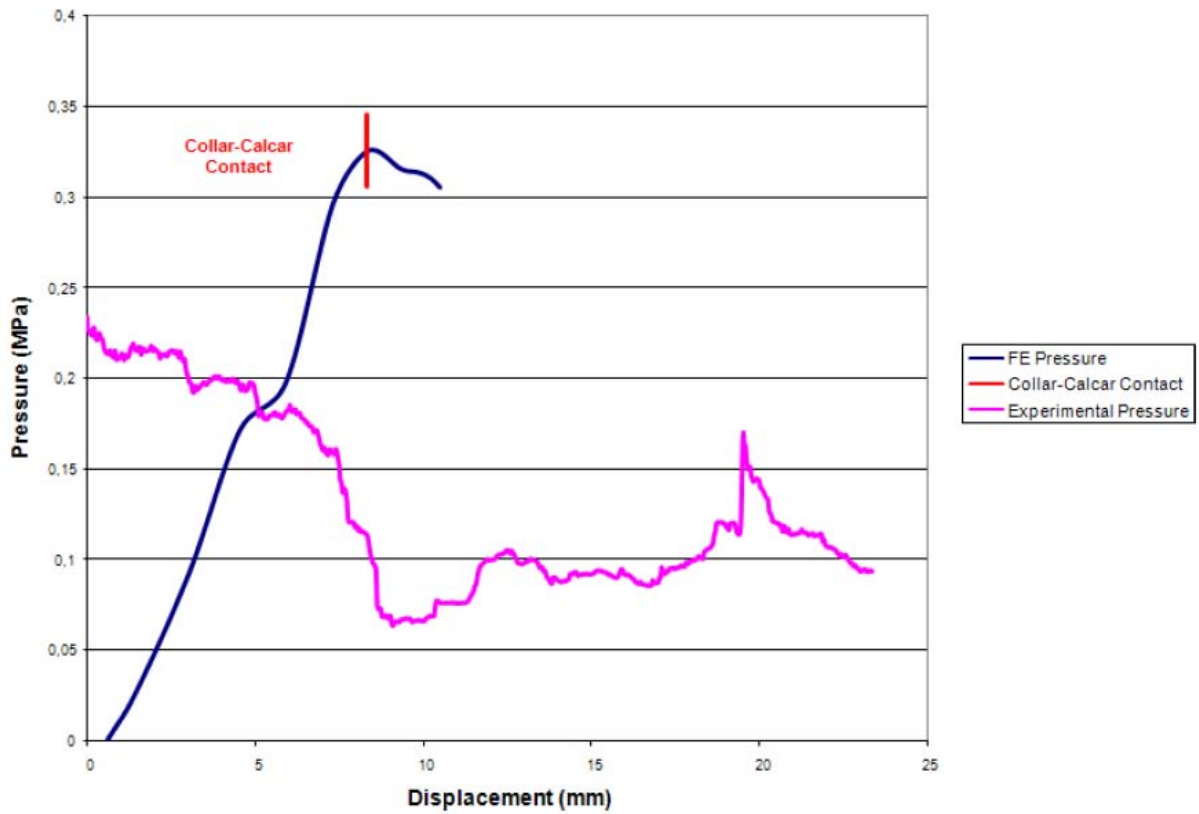
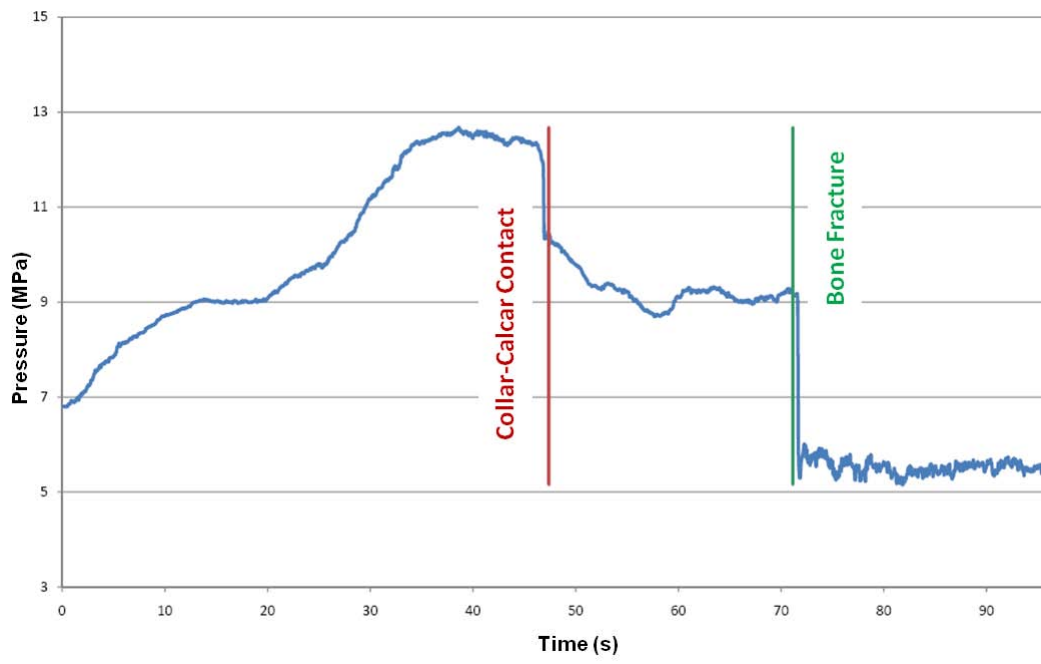


Figure 23





Session 3A

Biomedicine - Biomolecule

Miss Yekta Aminkashani

islamic azad university

Iran

yak4453@yahoo.com



“Modeling the appropriate sleep system and the spine of the patients who suffer from ankylosingspondilitis, designing and excluding the mattress stiffness cartography according to their sex and body shape.”

Y. Amin Kashani (1), N. Fatouree (2), K. Leilnahari (1)

(1) Islamic Azad University, Science & Research branch, Tehran, Iran

(2) Faculty of Biomedical Engineering Amirkabir - University of Technology (Tehran Polytechnic)

Keywords: Ankylosing Spondylitis, stiffness cartography

Summary:

Ankylosing spondylitis, or AS, is a form of arthritis that primarily affects the spine, although other joints can become involved. It causes inflammation of the spinal joints (vertebrae) that can lead to severe, chronic pain and discomfort especially in sleep time so it could reduce their sleep quality. In the most advanced cases (but not in all cases), this inflammation can lead to new bone formation on the spine, causing the spine to fuse in a fixed, immobile position, sometimes creating a forward-stooped posture. In the most usual sleep system, we have the same stiffness through their mattress materials. Recent studies show that this type of sleep system is not suitable even for a healthy person and it is recommended to design a suitable sleep system for every one due to their body shape and sex type. In addition, for these types of vertebral column's malformation, sleep systems show their importance on the patient comfort during their sleep. In this article, we are trying to design and model a suitable sleep system (mattress + base + head cushion) for patients who suffer from AS, and the first goal is to give them this opportunity to have more comfort and less pain when they are sleeping. In addition, modeling of their spine is included in this research. This model has different stiffness through the surface and it is depend on the best posture of sleep for these people. In addition, the effect of this designed sleep system on the deviation of vertebral column in different stages of the disease is compared with the effect of a model with the same stiffness through the surface. It is examined to see whether the designed model can be used to prevent the progress of the disease or not. The designing and achieving the appropriate cartography for the AS patients is considered as well. The sleep system model is designed according to sex, body shape and the stage of the progress of the disease in different people, and its effect on the stage of deviation of vertebral column after using it is compared with the time before using it. In doing this research, the modeling software ADAMS and LIFEMODE are used, which are the modeling of healthy person, the patient person with different stages of the disease, and the common and designed sleep systems. The variables considered in this research are as follow: - Unnatural deviation because of the disease - The amount of its improvement when putting the model patient on the modeled system - the deviation of vertebral column of the patient when using the old sleep system (mattress) with the same stiffness - the possibility of its extension to similar diseases of the vertebral column and its deviation



Session 3A

Biomedicine - Biomolecule

Dr. M. Moatamedi
Cranfield University
UK

m.moatamedi@cranfield.ac.uk



“Multiphysics Modelling of Aorta Implementing a Physiologically Realistic Material Model”

M. Moatamedi & K. Kayvantash

Keywords: aorta, blood vessels, impact, modelling, multiphysics

Summary:

In recent years there have been numerous attempts to accurately model phenomena that occur in the cardiovascular system of the human body. Problems of the cardiovascular system are commonly associated with low survival rates, thus attracting great interest. One specific area of concern is mechanism by which the aorta suffers heavy damage during automotive impacts. A large number of fatalities could be prevented annually with the design of new safety systems arising from a proper understanding of these mechanisms. It is well known that such injuries are a result of complex interactions between the vessels, the blood they carry and other parts of the body. As such they can only be accurately modelled using advanced multiphysics approach.

This research examines a number of material models for use in aortic impact problems, using the Arbitrary Lagrangian Eulerian (ALE) approach to simulate the interaction between the fluid (blood) and the structure (aorta) which aspires towards the development of a layered orthotropic blood vessel model.

SIMULATION-BASED CHARACTERIZATION OF STENOTIC VESSELS

V. Pazos

McGill University, Department of Mechanical Engineering,
Montreal Heart Institute, Research Center, 5000 Belanger East, Montreal QC H1T 1C8, Canada,
valerie.pazos@mail.mcgill.ca

R. Mongrain

McGill University, Department of Mechanical Engineering, MacDonald Building, 817 Sherbrooke
Street West, Montreal QC H3A 2K6, Canada
Montreal Heart Institute, Research Center, 5000 Belanger East, Montreal QC H1T 1C8, Canada,
rosaire.mongrain@mcgill.ca

J.C. Tardif

Montreal Heart Institute, Research Center, 5000 Belanger East, Montreal QC H1T 1C8, jc.tardif@icm-mhi.org

ABSTRACT

Clinical studies on lipid-lowering therapy have shown that changing the composition, and consequently the mechanical properties, of lipid pools, reduced significantly the risk of cardiac events associated with plaque rupture. However, knowledge about the mechanical properties of the human atherosclerotic lesion remains limited due to the difficulty of the experiments. The present work aims to assess the feasibility of characterizing a lipid pool embedded in the wall of a pressurized vessel using finite element simulations. Finite element simulations of inflation experiments are used together with non-linear least-squares algorithm to estimate the material model parameters of the wall and of the inclusion. An optimal fit of the simulated experiment and the real experiment is sought with the parameter estimation algorithm. The method was first tested on a single-layer PVA cryogel stenotic vessel, and then applied on a double-layer PVA cryogel stenotic vessel with a lipid inclusion.

Keywords: *arteries, plaque, finite element, hyperelastic, inflation*

1. INTRODUCTION

Cardiovascular diseases accounted for about 30% of all deaths, in the world [1] and among these deaths 40% were due to coronary artery disease. In coronary artery disease, atherosclerosis narrows the arteries supplying blood to the heart muscle, increasing the risk of a myocardial infarction. The rupture of the atherosclerotic plaque remains highly unpredictable and the underlying rupture mechanisms are still unclear [2]. Structural analysis of atherosclerotic arteries has suggested that plaque rupture is associated with stress concentrations and these stresses are highly dependent on the geometry and mechanical properties of the cap and lipid pool. Clinical studies [3] have shown that changing the composition, and consequently the mechanical properties [4], of lipid pools, using lipid-lowering therapy, reduced significantly the risk of cardiac events associated with plaque rupture. However, knowledge about the mechanical properties of the human atherosclerotic lesion remains limited. There are relatively few studies about the mechanical properties of human atherosclerotic arteries [5] and fewer about the mechanical testing of lipid pools due to the technical challenge on such experiments.

Methods based on iterative finite element simulations have been proposed to evaluate the elastic or hyperelastic parameters of biological soft tissues [6-10]. Some of them have the potential to be applied in-vivo [7, 9, 11]. The principle is to optimize the material model parameters of a finite element model by comparing the results of iterative simulations with the corresponding experimental data. The present work aims to assess the feasibility of identifying the material model parameters for the wall and for the lipid pool, using inflation experiment and non-linear least squares optimization of finite element simulations.

2. MATERIAL AND METHODS

2.1. Experimental data acquisition and processing

The in-vitro experimental data used for characterization was obtained by inflating axially prestretched specimens with hydrostatic pressures while acquiring US images with a 40MHz intravascular ultrasound transducer. IVUS images and pressure data were registered based on respective timers. Both were synchronized before acquisition.

The specimens were PVA cryogel-based asymmetric vessels that mimic stenotic coronary arteries with or without a lipid inclusion. Samples of the materials used for the mock artery wall were tested in uniaxial and biaxial tension to obtain reference data to compare with the estimates.

A semi-automated segmentation application was developed in Matlab to determine the boundaries of each component of the vessel. The automated part of the segmentation consisted in applying an edge detection using edge function of the MATLAB image processing toolbox and extracting the inner and outer points. The operator then removed the outliers. For the boundaries between the two gel layers and for the inclusion boundaries, the segmentation was made by the operator. Each contour was modeled using B-Splines [12].

2.2. Optimization framework

The optimization is performed with the nonlinear least-squares technique implemented in the *lsqnonlin* function of the MATLAB Optimization Toolbox (R7, Mathworks Inc.) and interfaced with finite element simulation in COMSOL (v3.4 with Structural Mechanics Module, COMSOL Inc.). Only the structural mechanics of the problem was considered. The material models have to be chosen according to a priori knowledge of the mechanical behaviour of the target tissues.

For given sections, 2-D quasi-static simulations were run for different pressure values corresponding to the experimental acquisitions. The distance between the simulated data and the experimental data was measured by the objective function, which consists of the squared differences between simulated and experimentally determined 1) circumferences, for each considered pressure values and each contour, 2) 5th, 50th and 95th percentiles of the thickness for each considered pressure values and each wall layer, and 3) thickness of the pool, for sections with lipid pool. The optimization algorithm searches for an optimal set of material parameters in order to minimize the objective function.

Evaluation of the method was performed by predicting the material behaviour in uniaxial and biaxial tensile test with parameters obtained from the inflation tests. The predicted tensile behaviour was then compared with actual tensile tests. The goodness of the prediction was defined with the value R^2 and visual analysis. R^2 is computed from the sum of the squares of the distances of the experimental points to the predicted curve (SSR) normalized to the sum of the square of the distances of the points from a horizontal line through the mean of all stress values (SST).

$$R^2 = 1 - \frac{SSR}{SST}$$

3. RESULTS

3.1. Single-layer stenotic mock artery

First, a single layer stenotic vessel in PVA cryogel (figure 1) has been used to test the algorithm. The nominal diameter of the lumen is of 3 mm, with a narrowing of 25% in cross-sectional area. The nominal wall thickness is of 1 mm.

Figure 2 shows the prediction obtained using one section near the peak stenosis, a two-term strain energy function $W = C_{10}(I_1-3) + C_{11}(I_1-3)(I_2-3)$, where C_{10} and C_{11} are material constants, I_1 and I_2 the first and second invariants and the Cauchy-Green deformation tensor, and simulated pressures of 3.4 and 6.7 kPa (25 and 80 mmHg).

A good agreement between the predicted and the measured data was observed for stretch up to 1.3 ($R^2 = 0.961$ for uniaxial tension and $R^2 = 0.992$ for biaxial tension). The prediction in biaxial tension remained good for stretch range of [1 1.6] ($R^2 = 0.928$).

3.2. Double-layer stenotic mock artery with lipid pool

The method was extended to characterize a double-layer PVA cryogel stenotic vessel with a lipid inclusion (figure 3). The nominal thickness of the inner layer is of 0.4 mm and 0.6 mm for the inner and outer gel layers respectively).

Each gel layer was modeled with two-terms Mooney-Rilvin models, same as previously, and neoHookean model was chosen for the inclusion. A first optimization was run with at a cross-sectional site with no inclusion, to obtain estimates for the 4 material model parameters of the gel layers. Based on this estimates as initial guess, a second optimization was run with a section near the peak stenosis to estimate the 5 material model parameters of the gel layers and of the lipid inclusion. Figures 4 and 5 show the prediction obtained for the inner and outer gel layer, respectively. For both gel layers, a good agreement was obtained between the predicted and experimental tension in the stretch range [1 1.3] ($R^2= 0.940$ in uniaxial and $R^2= 0.991$ in biaxial tension for the inner layer, and $R^2= 0.692$ in uniaxial and $R^2= 0.975$ in biaxial tension for the outer layer). The residuals being small, the estimate for the inclusion can be assumed to be good in that range of deformation.

4. CONCLUSIONS

Finite element simulations of inflation experiments were used together with non-linear least-squares optimization to estimate the material model parameters of the mock arteries. The objective function was defined based on deformed contours rather than strain estimation. It implied no assumption on small displacements.

Evaluation on mock arteries showed that the parameter estimation based on inflation experiments provide similar results as biaxial tension of the isolated tissue, with the difference that the lipid inclusion can hardly be tested when isolated because of its consistency.

REFERENCES

1. *World Health Report 2003: Shaping the future*, World Health Organization,(2003).
2. Richardson P.D. Biomechanics of plaque rupture: progress, problems, and new frontiers. *Annals of Biomedical Engineering*. **30**(4) (2002) 524-36.
3. Baigent C., Keech A., Kearney P.M., et al. Efficacy and safety of cholesterol-lowering treatment: prospective meta-analysis of data from 90,056 participants in 14 randomised trials of statins. *Lancet*; **366**(9493) (2005) 1267-78. Epub 2005 Sep 27.
4. Loree H.M., Tobias B.J., Gibson L.J., Kamm R.D., Small D.M., Lee R.T. Mechanical properties of model atherosclerotic lesion lipid pools. *Arteriosclerosis and Thrombosis*. **14**(2) (1994) 230-34.
5. Holzapfel G.A., Sommer G., Regitnig P. Anisotropic mechanical properties of tissue components in human atherosclerotic plaques. *Journal of Biomechanical Engineering*. **126**(5) (2004) 657-65.
6. Chandran K.B., Mun J.H., Choi K.K., et al. A method for in-vivo analysis for regional arterial wall material property alterations with atherosclerosis: preliminary results. *Med. Eng. Phys.*; **25**(4) (2003) 289-98.
7. Kauer M., Vuskovic V., Dual J., Szekely G., Bajka M. Inverse finite element characterization of soft tissues. *Medical Image Analysis*. **6**(3) (2002) 275-87.
8. Moulton M.J., Creswell L.L., Actis R.L., et al. An inverse approach to determining myocardial material properties. *Journal Of Biomechanics*. **28**(8) (1995) 935-48.
9. Remme E.W., Hunter P.J., Smiseth O., et al. Development of an in vivo method for determining material properties of passive myocardium. *Journal of Biomechanics*. **37**(5) (2004) 669-78.
10. Einstein D.R., Freed A.D., Stander N., Fata B., Vesely I. Inverse parameter fitting of biological tissues: A response surface approach. *Ann. Biomed. Eng.*; **33**(12) (Dec 2005) 1819-30.
11. Chandran K.B., Mun J.H., Choi K.K., et al. A method for in-vivo analysis for regional arterial wall material property alterations with atherosclerosis: preliminary results. *Medical Engineering and Physics*. **25**(4) (2003) 289-98.
12. Piegl L., Tiller W. *The NURBS Book*. Vol XIV. 2nd ed, New York: Springer-Verlag; (1997).

List of figures

Figure 1. Single-layer stenotic vessel made of PVA cryogel.

Geometry reconstructed from IVUS pullback acquisition

Figure 2. Experimental and predicted stress-stretch curves for uniaxial and biaxial tension

Figure 3. Double-layer PVA cryogel stenotic vessel with a lipid inclusion.

Geometry reconstructed from IVUS pullback acquisition

Figure 4. Experimental and predicted stress-stretch curves for uniaxial and biaxial tension of the inner layer material

Figure 5. Experimental and predicted stress-stretch curves for uniaxial and biaxial tension of the outer layer material

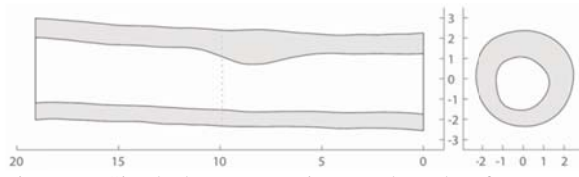


Figure 6. Single-layer stenotic vessel made of PVA cryogel. Geometry reconstructed from IVUS pullback acquisition

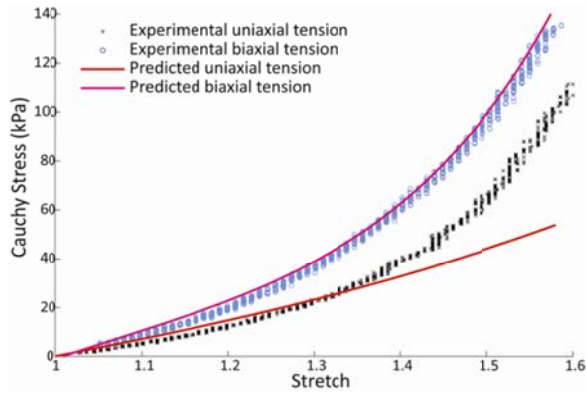


Figure 7. Experimental and predicted stress-stretch curves for uniaxial and biaxial tension

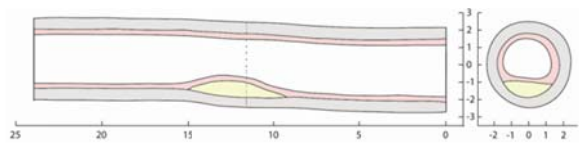


Figure 8. Double-layer PVA cryogel stenotic vessel with a lipid inclusion. Geometry reconstructed from IVUS pullback acquisition

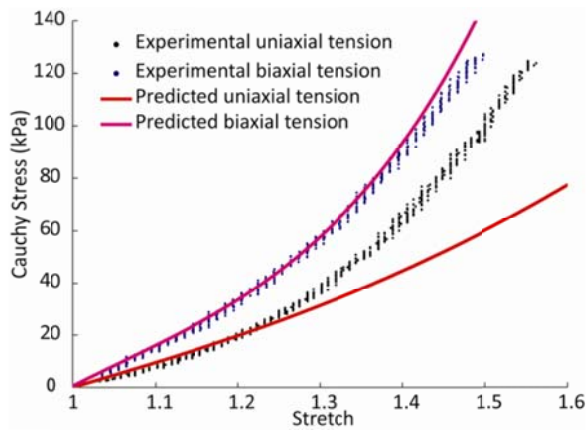


Figure 9. Experimental and predicted stress-stretch curves for uniaxial and biaxial tension of the inner layer material

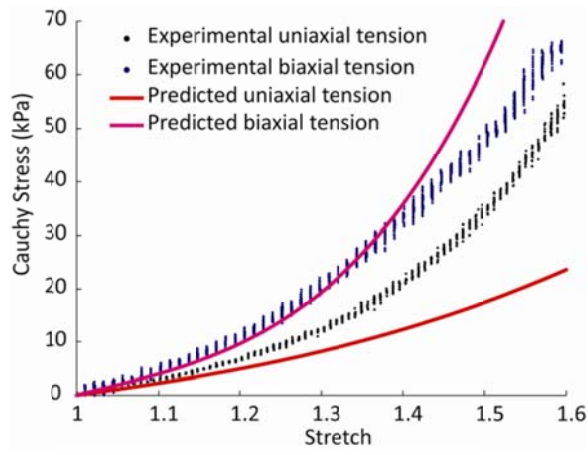


Figure 10. Experimental and predicted stress-stretch curves for uniaxial and biaxial tension of the outer layer material



Session 3A

Biomedicine - Biomolecule

Mr. Eric Wagnac
Ecole Polytechnique de Montreal
Canada
eric.wagnac@polymtl.ca



“Load rate effects on thoracolumbar spine injuries: a finite element investigation in dynamic compression”

E. Wagnac, P.J. Arnoux, A. Garo, C.E. Aubin

Keywords: Thoracolumbar spine, finite element analysis, dynamic load rate, spinal injuries

Summary:

Objective: To investigate how dynamic load rate in compression affects the risk of fractures and soft tissue injuries in the thoracolumbar (TL) spine.

Background: In vitro experiments showed that compressive fracture patterns and locations in the TL spine were sensitive to the load rate. A better understanding of the biomechanical characteristics of the spine is required to improve injury prevention and treatments. Methods: A detailed finite element model of the thoracolumbar spine (T12, L1 and L2 vertebrae, the associated intervertebral discs (IVDs) and spinal ligaments) was used to simulate spinal lesions at load rates of 0.01, 0.1, 0.2 and 1 m/s. The bone structure was modeled using a symmetric elasto-plastic material law (Johnson-Cook) that incorporates strain rate dependency. Fractures were simulated using a mesh elimination method based on elongated plastic strain threshold (Kimpara et al., 2006). The IVDs' components (annulus and nucleus) and the ligaments were respectively governed by hyperelastic (Mooney-Rivlin) and viscoelastic (generalized Maxwell-Kelvin-Voigt) material laws while the fibers were modeled using a non-linear elastic material (El-Rich et al., 2009). Hyperelastic parameters of the IVDs' components were related to the load rate through an analytic function based on the experiments of Kemper et al. (2007). Ultimate stress and strain levels were interpreted to analyze the damage occurrence of soft tissues. Results: Preliminary results showed that the peak load increases with the load rate, while the displacement to failure decreases. Quasi-static load rate resulted in endplate fractures while vertebral body fractures appeared at higher load rates. Peak intradiscal pressure and annulus fiber stress were also markedly affected by the load rate.

Conclusion: The risk of spinal injuries is strongly affected by the load rate. Higher load rates in dynamic compression reduces the safety margin of spinal components. Such finding could lead to the development of new failure criterions of the TL spine based on the impact speed.

Developing a method to simulate injury mechanisms in motorcycle crashes

Symeonidis I.¹, Kavadarli G.¹, Brenna C.¹, Zhao Z.¹, Fraga F.², van Roij L.², Schuller E.¹, Peldschus S.¹

(1. Institute of Legal Medicine, Ludwig Maximilian University, Munich, Germany, 2. Netherlands' Organization for Applied Scientific Research TNO Automotive, Eindhoven, Netherlands)

ioannis.symeonidis@med.uni-muenchen.de

Institut für Rechtsmedizin der Universität München,

Nußbaumstr. 26,

80336 München,

Tel: +49 (89) 2180 - 73 368 - Fax: +49 (89) 2180 - 73 009

Keywords: *motorcycle; injuries; FE model; motion capture; electromyography*

1. Introduction

Every year, road traffic related accidents claim an estimated 40,000 lives and injure 1,600,000 citizens in Europe [APSN 2004]. Motorcyclists' casualties are estimated somewhere between 1/6 and 1/8 of total road fatalities [COST 2001] and it is clear that the corresponding research effort and budget are not allocated in proportion with the relevance of motorcycles within the road safety context. Existing motorcycle-related experimental trials are very limited in number and generally very specific in goals [ISO 2005]. Because motorcyclists' posture and movement significantly influence the global system's behaviour (motorcycle + rider), experiments with volunteers are necessary to study body posture and reactions during riding, therefore improving and validating computational models. This study aims at the development of a method for the simulation of injury mechanisms in motorcycle crashes by the application of new experimental results.

From the Hurt report [HURT 1981], a motorcycle safety study conducted in the United States, analysing 900 motorcycle accidents, derive that at 36.3% of the accidents the motorcyclists used the brake, at 8.4% they only swerved, at 20.9% they combined brake and swerve and at 31.9% no action was performed. According to the MAIDS report [ACEM 2009] that analyzed 921 accidents and 923 exposure cases, emerges that the 49.3 % of the motorcyclists performed a braking, the 16.2% a swerve manoeuvre and only 26.9% involved in the accident did not attempt a collision avoidance manoeuvre. Further 90% of all risks to the motorcyclists, both vehicular and environmental, were in front of them prior to the accident, so if the motorcyclists had the required skill, motorcycle manoeuvrability and time they could react to the danger with a manoeuvre. From these two studies we can conclude that braking and swerving is a very common manoeuvre performed in pre-crash situations from motorcyclists and only in 1/3 of the cases the motorcyclist's posture is the same as the initial normal riding posture. Additionally these manoeuvres are resulting in an out- of- position (OOP) posture of the motorcyclist, since the motorcycle control involves not only steering but also the displacement of the motorcyclist's centre of mass (COM) from the normal riding posture.

Due to the wide variety of the possible motorcyclist's posture before the impact, the simulation of motorcycle accidents is complicated. To simplify the analysis the crash simulation can be separated in two phases a pre-crash phase analyzed with a multi-body model and then by using the output kinematics as input the crash phase can be analyzed with a detailed finite element human model which can predict injuries.

2. Materials and methods

In more detail, the motorcyclist's posture during riding is influenced from the three following factors:

- the anthropometric characteristics of the motorcyclist
- the type of motorcycle he is using,
- the manoeuvre he is performing

The following analysis and experiments were performed to study the influence of these factors.

2.1. Type of motorcycle

There are many different types of motorcycles available in the market. This variability on the motorcycle type is producing different postures to the motorcyclists. To explore this influence a short study was performed on the geometrical dimensions of different types of motorcycles. A sample of 30 different motorcycle models was analyzed using side view digital photographs and a method based in photogrammetry. The motorcycle models were all the models available in the German market from a single manufacturer. The motorcycles were grouped according to their style in different categories. The selection of the categories was according to the MAIDS report [ACEM 2009]. The selected geometrical characteristics, important for this study were the handlebar, the footrests and the seating point on the saddle.

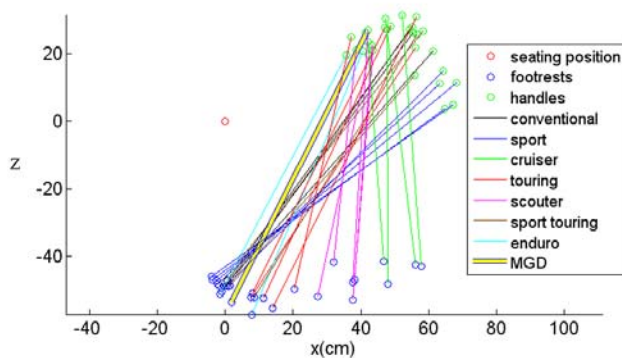


Figure 1 Geometry difference of motorcycle types

Two motorcycle types that are popular between the motorcyclists and with geometry that envelopes the geometry of the other types were used for the experiments, that are described briefly below, a sport motorcycle (blue) and a touring motorcycle (red).

2.2. Manoeuvres and posture

For the kinematics and posture analysis of the swerving and braking manoeuvre two experiments were performed using an optoelectronic motion capture device.

In the swerving experiment [BRE 2008] the motion of five volunteers was captured on two immobilized motorcycles, one sport and one touring. The volunteers were asked to take a comfortable riding position and move as fast as possible, on one side of the motorcycle and then to the other side. This experiment was performed to study in detail the posture of the motorcyclists on different motorcycles and the maximum values of the swerving kinematics (displacement, velocity, acceleration) of the motorcyclist in repeatable controlled laboratory

conditions. The overall volunteer's COM maximum lateral translation during swerving on the touring motorcycle was measured 28cm and on the sport 19cm.



Figure 2 Swerve motion on sport motorcycle

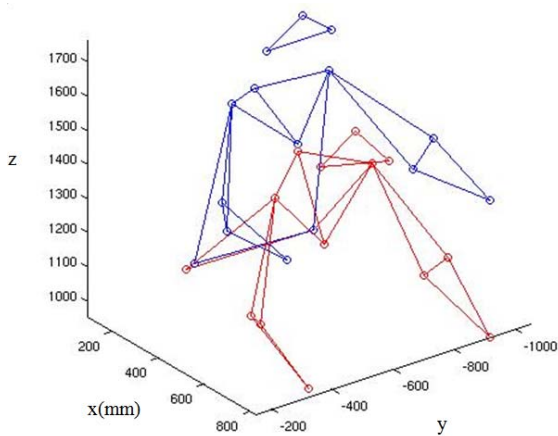


Figure 3 Upper body posture on sport (red) and touring (blue) motorcycle

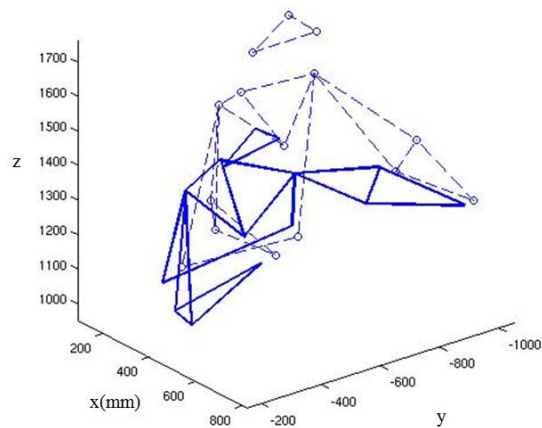


Figure 4 Swerve motion on the touring motorcycle (bold blue)

In the braking experiment [SYM 2008] the motion and muscle activity - using an electromyography device (EMG) - of eight volunteers was captured during simulated braking of a touring motorcycle. A device was constructed that can reproduce the geometry of the rider- motorcycle interface of most types of motorcycles (MGD). The MGD was mounted on a moving sled. The volunteers were asked to take a comfortable riding position on the MGD and to brake when they decided; a brake placed on the right side of the handle bar was

triggering the experiment. When the trigger was activated the sled would move backward -the volunteer was facing forward - with a stable acceleration comparable to braking, thus simulating the deceleration that a motorcyclist is experiencing during braking. Care was taken for the visual and auditory perception of the volunteers. The activity of the arm and neck muscles was also captured so body bracing and the stabilization of the head during braking can be studied. The overall volunteer's head forward translation during braking was measured 26cm and for the sternum 19cm.

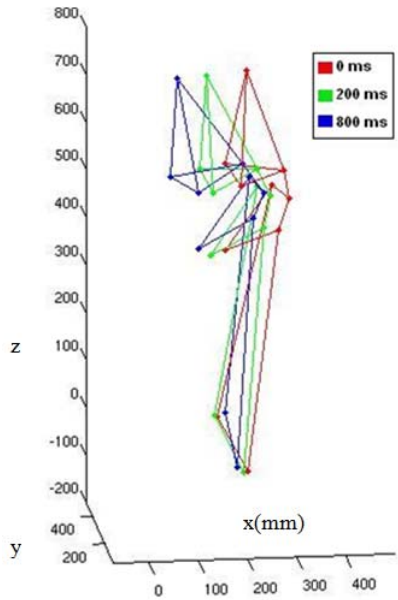


Figure 5 Forward upper body displacement relative to the sled during braking

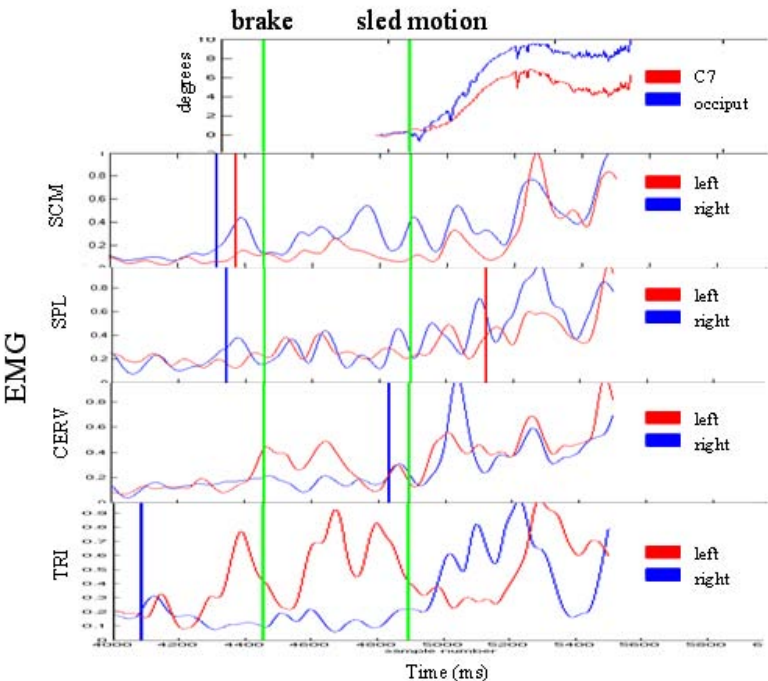


Figure 6 Synchronized EMG and head kinematics

2.3. Pre-crash phase

A motorcycle accident is not only the crash but it is a process that starts earlier in time when the motorcyclist starts to perform the avoidance manoeuvre. Additionally the motorcycle accidents involve complicated kinematics and many degrees of freedom for the motorcyclist's motion. For the previous reasons and because of the high computational costs of the finite element analysis, the pre-crash phase can be more efficiently studied with multi-body dynamics models. The MADYMO facet human model coupled with the detailed head and neck [HOR 2002] is used for this reason. MADYMO also provides a model of a touring motorcycle, which's trajectory can be prescribed and controlled by parameters of torque on the handlebar, front /rear brake and engine.

The human model has detailed facet geometry for the detection of contact with other objects but it continues to be a fast calculating multi-body model. The model is validated concerning the kinematics and accelerations for various impacts for car occupant safety. Each spinal segment is connected with sensors and joint actuators and control feedback methods can be implemented. The spine is already validated against volunteer impactor tests and rollover experiments [CAP 2007].

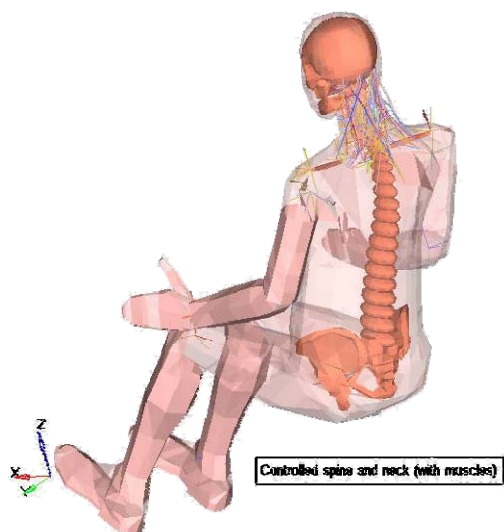


Figure 7 MADYMO facet human model coupled with detailed neck

The detailed neck model includes the neck muscles and allows their individual activation at different activation states. Further a controller is being developed that can activate single muscles in order the motorcyclists head to follow a strategy (e.g. to maintain the head upright during braking) [FRA 2009]. This controller will be validated with the kinematic and EMG results of the braking experiment.



Figure 8 Simulation of braking with active stabilizing neck.

2.4. Crash phase

For the crash phase of the accident the finite element model HUMOS2 (human model for safety 2) model will be used. The HUMOS2 numerical model consists of 84000 elements and 60000 nodes. More than 500 material descriptions have mostly been developed on an experimental basis. The loading of the model in the validation aimed at reproducing conditions that are typical for a car occupants as for instance shown in [MER 2006] for lateral loading of the thorax. From the validation with impact directions in several body axes a potential applicability to other loading configurations can be derived.

2.4.1. Positioning tools

HUMOS2 model has also positioning tools developed in different pre-processors that allow the placement of the model at different car-seats. These tools are very fast and useful for small rearticulations where the mesh deformation is not very high. Instead for large changes in the posture local remeshing of some flesh parts and skin is required. Finally the new posture after the rearticulations can be stored in a database for further use.

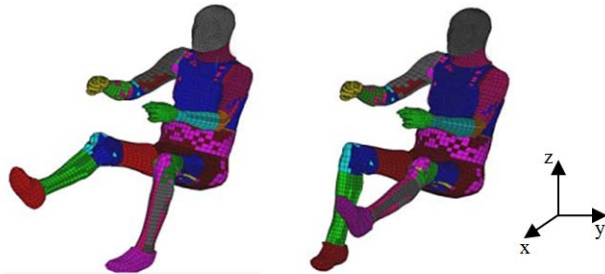


Figure 9 HUMOS2 car-occupant positioning [VER 2006]

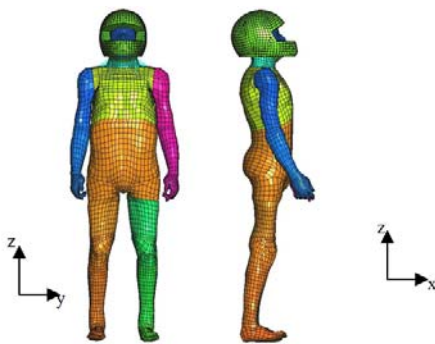


Figure 10 HUMOS2 pedestrian model fitted with helmet

The positioning tools also extend the application of HUMOS from car-occupant to pedestrian model with the change of posture from sitting to standing. These two models (pedestrian and car occupant) were further used with the introduction of a helmet as a motorcyclist's model after the separation of his motorcycle, for impact simulation with roadside furniture (road safety barriers, signs) [PEL 2007]; in this way allowing the use of a single common numerical

human model for simulation of many different accident configurations.

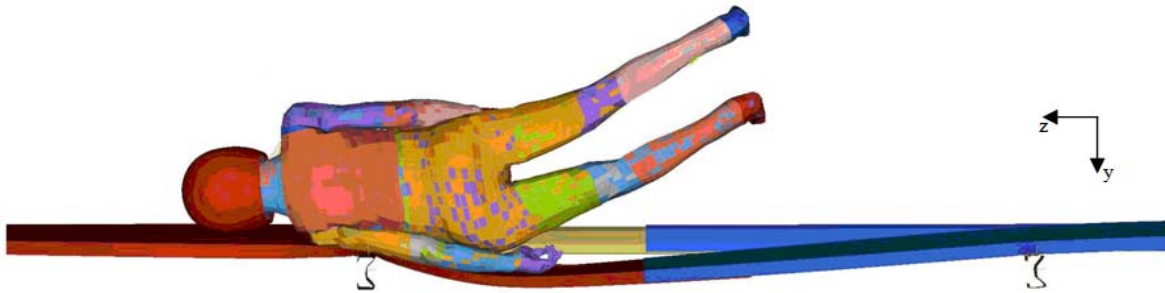


Figure 11 Simulation for the study of public domain barrier design safety, investigating thorax and head injury [ZHA 2008]

With the kinematic data from the presented experiments we are aiming at the development of more postures for HUMOS2 model for motorcycle simulations, with the rider on the motorcycle. Further, the analyzed EMG data, from the braking experiment, can also be used to preactivate HUMOS2 neck muscles for the head stabilization in case of a simulation of braking before an accident and to introduce a bracing action for the rest of the body.

3. Conclusions and Discussion

A method to simulate accidents with motorcycles with the application of results from volunteer tests was presented. This method extends the applications of HUMOS2 model for motorcycle accidents, with the human model on the motorcycle.

A limitation of the presented method is that it cannot predict the complicated kinematics of the motorcyclist if he falls down from the motorcycle before the impact or if he loses control without another involving vehicle, even though there are studies toward this direction [COS 2005]

This method can have application on the following fields:

- the effectiveness of already available protective devices by the simulation of reconstructed accidents where these devices were used from the motorcyclists.
- the potential effectiveness of prototype protective devices by the simulation of injuries on reconstructed real accidents with the use of these devices.
- global validation of human models on real world impact situations based on a sufficient number of real-world accidents.
- detailed accident reconstruction tool with kinematics related to the inflicted injury.

4. Acknowledge

This research was mostly funded by the MYMOSA (MotorcYcle and MOtorcyclist Safety) training network, a Marie Curie action of the 6th research framework program of the EU. The authors want to thank Prof. Schneider of the University of Federal Armed Forces, Munich, for providing the measuring devices for the experiments and Mr. Andreas Born for his assistance in technical issues. Finally, we want to thank Prof. Marco Pierini from University of Florence for his support.

5. References

ACEM, 2004. *MAIDS In-depth investigation of accidents involving powered two wheelers*. Association of European Motorcycle Manufacturers (ACEM), Brussels, Belgium.

APSN (Directive of the European Vehicle Passive Safety Network), 2004. *Roadmap of future automotive passive safety technology development*, Amsterdam, The Netherlands.

Brenna C., 2008, *MYMOSA – Towards a virtual motorcycle rider for realistic simulations of motorcycle manoeuvres*, Proceedings of the 7th International Motorcycle Conference, Cologne, Germany.

Cappon H., 2007, *Computational Human Model with Stabilizing Spine: a Step Towards Active Safety*, SAE World Congress & Exhibition, Detroit, MI, USA.

Cossalter, V., 2005, *Exploratory Study of the Dynamic Behaviour of Motorcycle-Rider During Incipient Fall Events*, 19th International Technical Conference on the Enhanced Safety of Vehicles Conference (ESV), Washington D.C., USA.

COST 327, 2001. *Motorcycle Safety Helmets, Final Report of the Action*, European Communities, Belgium.

Fraga F., 2009, *Development and preliminary validation of a motorcycle rider model with focus on head and neck biofidelity, recurring to line element muscle models and feedback control*, 21th International Technical Conference on the Enhanced Safety of Vehicles Conference (ESV), Stuttgart, Germany.

Horst M. van der, 2002, *Human head neck response in frontal, lateral and rear end impact loading – modeling and validation*, PhD Thesis, Eindhoven University of Technology, The Netherlands.

HURT. H.H. 1981, *Motorcycle accident cause factors and identification of countermeasures* volume i: technical report for NHTSA, California, USA.

ISO 13232-3:2005, 2005. *Motorcycles, Test and analysis procedures for research evaluation of rider crash protective devices fitted to motorcycles – Part 3: Motorcyclist anthropometric impact dummy (MATD)*.

Merten K. von, 2006, *Using HUMOS2 model for the reconstruction of accidents with thoracical injuries*, Journal of Biomechanics 39, s1 p165.

Peldschus S., 2007, *Technical bases for the development of a test standard for impacts of powered two-wheelers on roadside barriers*, 20th International Technical Conference on the Enhanced Safety of Vehicles Conference (ESV), Lyon, France.

Symeonidis I., 2008, *Laboratory set-up for the analysis of motorcyclists' behaviour during deceleration*, The 6th Int. Forum of Automotive Traffic Safety (INFATS), Xiamen, China.

Verriest J.P., 2006, *Development of whole body human models for virtual testing in HUMOS2 and APROSYS*, Workshop Virtual Testing in Regulations, Delft, The Netherlands.

Zhao Z., 2008, Master thesis *Development of a FE model of a roadside safety barrier for the simulation of motorcyclists' impacts*, Technical University Munich, Germany.



Session 4

Impact Biomechanics

Mr. Jean-Sébastien RAUL
(picture Prof. Willinger)
IMFS – University of Strasbourg

France
js.raul@unistra.fr



“Numerical modelling of the shaken baby syndrome”

Raul JS, Roth S, Willinger R.

Keywords: shaken baby, finite element model, child

Summary:

The “shaken baby syndrome” is the leading cause of death or serious neurological injury resulting from child abuse. Injuries that characterize the shaken baby syndrome are subdural haemorrhage and retinal haemorrhage. For the past 20 years, child head injury biomechanics have been studied through the evaluation of rotational and linear velocities and acceleration. Brain injury can be caused either by vigorous shaking, by a shaking followed by an impact on a soft or hard surface or by direct blows to the head. Vigorous shaking will initiate for a certain frequency a relative motion of the brain and skull, tearing the bridging veins that extend from the cortex to the dural venous sinus and leading to a subdural hematoma. Vigorous shaking can also cause neck injuries, and the younger is the child, the greater is the effect of force exerted during shaking. Injuries to the neck will be either articular or ligament injuries of the cervical spine as well as injuries to the spinal cord. Studies using dummies or analytical models have compared child head injuries as a function of angular and linear acceleration, but this scientific approach is insufficient when the local behaviour of biological tissues must be taken into account. Finite element methods appear as an emerging tool in the study of the biomechanics of head injuries in children and we shall show their potential application in the study of the “shaken baby syndrome”.



Session 3B

Biomechanics - Biomaterials

Dr. B Serpil Acar
Loughborough university
UK



“Computational Modelling and Simulations for Pregnant Occupant Safety”

B Serpil Acar and V Esat

Keywords: Pregnant woman, injury, Finite Element simulation

Summary:

Motor vehicle collisions are the leading cause of accidental death worldwide. Seatbelts save lives however, there is a need for improved automotive seatbelt protection for people who have difficulties in keeping the traditional seatbelt in its intended position. In particular, pregnant women are perfect examples of this group of people and present a challenge for automobile manufacturers. A series of projects have been undertaken in Loughborough University to improve the safety of pregnant occupant by developing guidelines and products based on biomechanics research, modelling and simulations. In this paper modelling the pregnant occupant ‘Expecting’ and simulations are explained, and some research results with ‘Expecting’ to improve safety of pregnant women are presented.



Session 3B

Biomechanics - Biomaterials

Mr. Jérôme Delotte
CHU Nice
France



“A 50th centile Humos pregnant woman model and a study of the injury mechanisms to the uterus”

Jerome Delotte (1), Lionel Thollon (2), Michel Behr (2), Jeremie Peres (2), Kambiz Kayvantash (3), Christian Brunet (2)

1. CHU Nice
2. INRETS
3. Cranfield University

Keywords: Pregnant woman, injury, Finite Element simulation

Summary:

Based on crash statistics, it has been estimated that approximately 130 000 pregnant women are involved in car crashes in the United States of which 160 are killed. For the pregnant women who survive it is estimated that between 300 and 3800 experience fetal loss.

To better understand the mechanisms involved and the influent parameters leading to foetal death in car accidents a pregnant dummy and finite element models of a 5th centile pregnant woman have been developed over the last ten years. None of those models integrate internal organs whereas abdominal organs are in direct contact with the uterus.

That is why a model has been developed in the Laboratory of applied Biomechanics. This model is based on the 50th centile Humos Model and integrates a detailed pregnant uterus which geometry has been taken from MRI images.

Various limitations have been identified in former studies:

- The Geometry is not representative of a medium woman
- The shape of the pelvis is that of a male
- The amniotic liquid is represented as a solid instead of a fluid

We present the design of a 50th centile finite element pregnant woman model based on the Humos FE model.

Three steps have been performed to build the whole model:

- The Building of a Gravid Uterus Model composed of the uterine wall, the placenta, the foetus and the amniotic liquid represented using the ALE Finite element formulation.
- The modification of the Humos 50th centile male model into a 50th centile female model.
- The integration of the Gravid Uterus into the 50th centile female model.

We present also a study on the hypothesised injury mechanisms that can lead to abruptio placentae.



Session 3B

Biomechanics - Biomaterials

Mr. Jérémie Peres

INRETS

France

Jeremie.peres@inrets.fr



“A 50th centile Humos pregnant woman model and a study of the injury mechanisms to the uterus”

J. Peres (1), M. Behr (1), L. Thollon (1), K. Kayvantash (2), C. Brunet (1)

1. INRETS

2. Cranfield University

Keywords: Pregnant woman, injury, Finite Element simulation

Summary:

Based on crash statistics, it has been estimated that approximately 130 000 pregnant women are involved in car crashes in the United States of which 160 are killed. For the pregnant women who survive it is estimated that between 300 and 3800 experience fetal loss.

To better understand the mechanisms involved and the influent parameters leading to foetal death in car accidents a pregnant dummy and finite element models of a 5th centile pregnant woman have been developed over the last ten years. None of those models integrate internal organs whereas abdominal organs are in direct contact with the uterus.

That is why a model has been developed in the Laboratory of applied Biomechanics. This model is based on the 50th centile Humos Model and integrates a detailed pregnant uterus which geometry has been taken from MRI images.

Various limitations have been identified in former studies:

- The Geometry is not representative of a medium woman
- The shape of the pelvis is that of a male
- The amniotic liquid is represented as a solid instead of a fluid

We present the design of a 50th centile finite element pregnant woman model based on the Humos FE model.

Three steps have been performed to build the whole model:

- The Building of a Gravid Uterus Model composed of the uterine wall, the placenta, the foetus and the amniotic liquid represented using the ALE Finite element formulation.
- The modification of the Humos 50th centile male model into a 50th centile female model.
- The integration of the Gravid Uterus into the 50th centile female model.

We present also a study on the hypothesised injury mechanisms that can lead to abruptio placentae.



Session 3B

Biomechanics - Biomaterials

Mr. Frank Meier
University of Strasbourg
France
meyer@imfs.u-strasbg.fr



“Numerical tools for real world whiplash accident investigation”

Meyer F., Bourdet N., Willinger R.

Keywords: whiplash, head/neck finite element model, modal analysis

Summary:

The objective of the present study was to simulate numerically with the Head-Neck FE model developed at University of Strasbourg a real rear impact. The crash pulse acceleration was obtained from Folksam, an insurance company. In order to obtain the full kinematics at the first thoracic (T1) an original lumped model of the human torso was developed and coupled to a car seat-head rest complex. The hypothesis of linear behaviour was

used for the torso being subjected to small deformations. The validation was performed in the frequency domain in terms of natural frequencies and damping as well as mode shapes. The modal

analysis of the human torso in a seating position conducted by Kitazaki et al. (1992) was used for both masses and mechanical properties identification. Concerning the simulation of the rear impact the crash pulse recording was implemented in the seat and the 6 accelerations at T1 was calculated and transfer to the Head-Neck FE model (Meyer et al. 2004). The joint relative motions, the vertebrae relative rotations and the classical parameters such as the linear and rotational head acceleration, T1 versus head linear displacement and NIC were computed.

Does neck segment exhibit the same vulnerability according to various impact conditions?

J. SUN*†‡, P. BERTRAND‡, R. KRAENZLER† and P.J. ARNOUX†

† Laboratoire de Biomécanique Appliquée, UMRT24 INRETS Université de la Méditerranée, Faculté de Médecine Nord, Bd. P. Dramard, 13916 Marseille cedex

‡ SHARK-Helmets, Zac. De la valentine, 110 route de la Valentine, 13396 Marseille cedex 11

*Corresponding author. Email: jingchao.sun@inrest.fr

Keywords: cervical spine; trauma; impact velocity; finite element simulation

Abstract: In pedestrian, cyclist and motorcyclist accidents, cervical spine injuries are often observed with complex mechanisms as occurring for multidirectional loadings. In this work, the finite element analysis was used to predict the injury chronology and specific injured components of the cervical spine segment. Five different impact directions (frontal, lateral, rear, frontal oblique, rear oblique) simulations were analyzed with an initial velocity 5m/s and 7m/s. The first injury recorded were ligament ruptures of upper cervical spine and bone fractures of low cervical spine. Comparing these simulation results, the injuries under flexion mechanism seems to be less severe as for extension or coupled kinematics.

1 Introduction

The cervical spine segment is a very complex and mobile structure of the human body [1]. Once trauma situation occurs, the head-neck segment is highly loaded leading to severe trauma with a lethal or permanent incapacity risk. Cervical spine was largely studied from its mechanical properties to frontal impact to investigate whiplash mechanisms [2, 3]. For pedestrian, cyclist and motorcyclist accidents, the head-neck segment is loaded under various impact directions. Also, how these impact directions can have an incidence on the injury mechanisms, potential injury and their severity? And does neck segment could be observed different kinematics and injuries in various impact velocities? To answer these questions, the finite element simulations [4] could be a valuable tool. By simulating frontal, lateral, rear and oblique dynamic loadings on the HUMOS head-neck segment, this numerical study showed weakness area on the spinal segment whatever the impact condition.

2 Material and Methods

The model used was the HUMOS head-neck segment under loading conditions relevant with those used for model validation [4]. For test convenience, the lower thorax, abdomen, lower and upper limb were removed. The upper thorax component was set as a rigid body and fixed. As no investigations were

performed on head segment, it was set as rigid body. The test consisted in a 75Kg circular plate (to include whole body inertial effects) with an initial velocity of 5m/s and 7m/s. Five loading conditions, from frontal impact to rear impact were investigated (cf. Figure 1). The simulations were recorded during 40ms on the 5m/s and 30ms on the 7m/s. One major interest in human modelling remains in the possibility to record specific parameters which cannot be recorded during experiments. Hence, the numerical injury identifications are assessed through the combined analysis of the joints kinematics (to identify pathological movement [5]); the Von Mises level was assumed as an indicator for bone fracture (130MPa and 50MPa for compact and spongy bone respectively); and strain level to investigate potential failure risk for ligaments according to Yoganandan and Panjabi works [4, 6, 7].



Figure 1 illustration of impact configuration

3 Results

Head-neck segment kinematics:

On the 5m/s velocity:

In the frontal impact direction, head segment exhibited a translating kinematics which is perpendicular to the impactor plane from 0ms to 14ms. The neck segment showed an extension kinematics. From 14ms the whole head-neck segment exhibited a hyper extension kinematics. At the end, the upper cervical spine exhibited dilatation processes.

In the lateral impact direction, the head-neck segment showed lateral rotation whereas the upper and lower cervical spines exhibited local rotation.

In the rear impact direction, from 0ms to 10ms head segment exhibited a translating kinematics in the

impact velocity direction which induced a homogeneous flexion kinematics for the cervical spine. After 10ms, the whole head-neck segment was observed a hyper flexion kinematics.

In the frontal oblique and rear oblique impact direction, the head-neck segment reported coupled lateral flexion (extension) and torsion effects homogenously distributed along cervical spine.

On the 7m/s velocity, the similar mechanisms as reported before were observed. The major differences were reported by the time for the different steps of cervical spine kinematics. In the particular, if the lower cervical spine exhibits same amplitude for rotations, the upper cervical spine exhibits increase rotation level which could be correlated to a higher injury risk.

	5m/s					7m/s				
	8ms	16ms	24ms	32ms	40ms	6ms	12ms	18ms	24ms	30ms
Frontal										
Lateral										
Rear										
Frontal Oblique										
Rear Oblique										

Table 1 head neck segment kinematics on different velocity

Virtual trauma:

On the 5m/s velocity:

In the frontal impact direction, the lower cervical region i.e. around C4-C6 was highly recruited leading to potential bone failure translating from C6 to C5 and C4. The upper cervical component C0-C2 exhibits also a potential failure of the anterior longitudinal ligament due to hyper extension effects.

The lateral impact showed firstly potential bone fracture for the lower cervical spine structure with C6 bone fracture to C5 C4 and C3. Local rotation on C0-C2 induced potential failure of apical ligament.

The rear impact showed potential simultaneous bone failure on C6 and C5. The interspinous ligament was assumed to reach its ultimate threshold on C1-C2.

The frontal oblique impact led to postulate on severe trauma probably induced by the combination of lateral and frontal extension. The lower cervical spine showed fractures from C6 to C3 spine units. The ligament failures were postulated on the upper cervical spine mainly with apical ligament on C0-C2.

The rear oblique impact exhibited the same combination effects as in the previous case: potential injury the interspinous ligament on C0-C2. The C6 and C5 bone potential failure was showed.

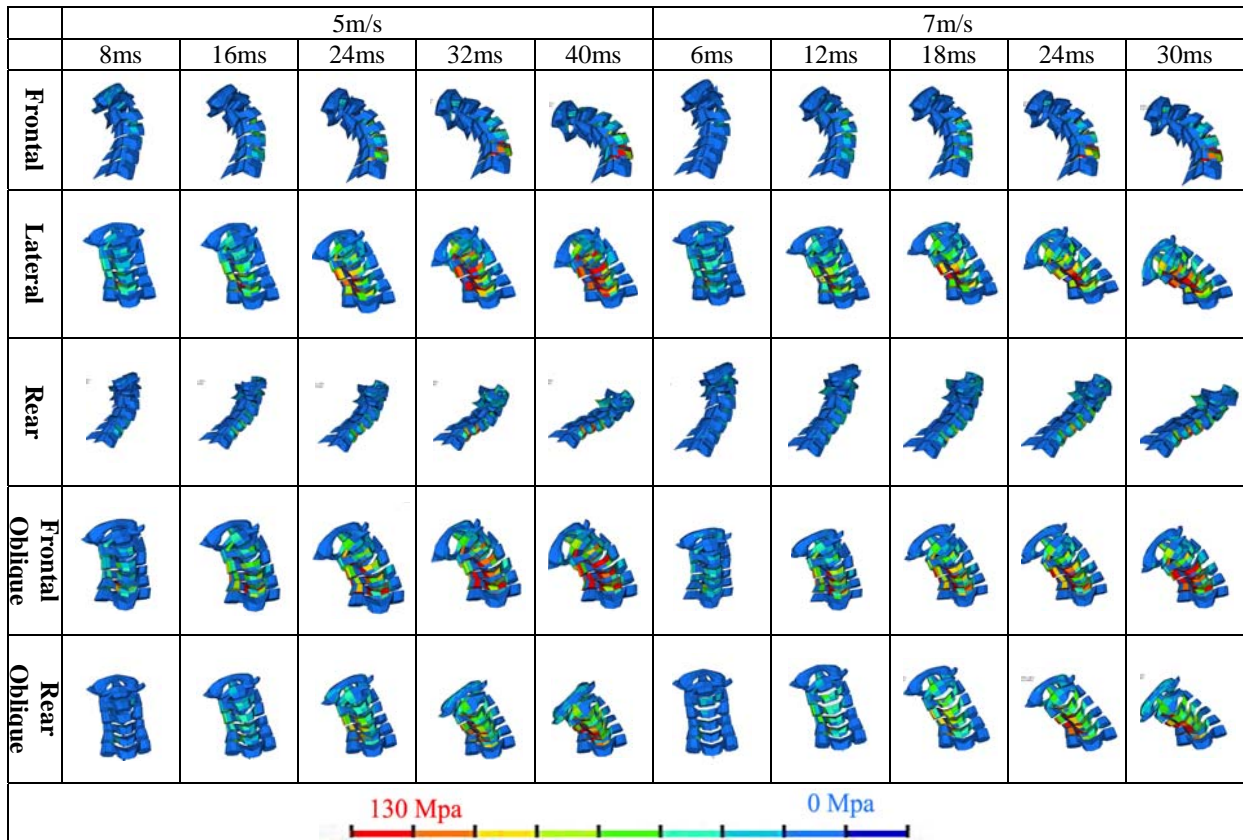


Table 2 cervical vertebraes Von Mises

On the 7m/s velocity:

The frontal impact showed potential bone failure on C6 and C5. Note that there is not bone failure recorded on C4. The anterior longitudinal ligament of

upper cervical spine segment was highly recruited to its potential failure level.

The lateral impact exhibited the similar injury chronology as on the 5m/s velocity with fracture C6,

C5, C4 and C3. A potential failure of apical ligament on C0-C2 was postulated.

The rear impact led to a hyper flexion kinematics with C6 and C5 potential failure. Local rotation on C1-C2 induced the interspinous ligament potential failure.

The frontal oblique impact showed the same mechanisms as with the previous velocity. The lower cervical spine potential failure was observed with C6 to C3. The apical ligament was observed a potential failure.

The rear oblique impact exhibited combination flexion and torsion effects leading to C6 and C5 potential failure.

4 Conclusions – Discussion

In frontal impact, for the same position of the impactor, the lower cervical spine showed the same kinematics level whereas the upper cervical structure, exhibited an increase range of mobility compatible with S-shape effects described for Whiplash trauma [4]. This increased mobility could have strong incidences on injury risk (bone fracture, ligaments injuries).

Simulations performed in these works exhibit potential injuries of the upper and the lower cervical spine. Bone fractures were essentially recorded from C6 to C4 in the frontal, lateral and frontal oblique impact simulations; the ligament injuries were most recorded on the upper cervical spine in the lateral, frontal oblique and rear oblique impact simulations. If the injury chronology showed large dispersion (Table 3), the injuries observed under flexion mechanisms were less severe as under extension and coupled kinematics. It seems that these potential failures were observed at the similar head-neck segment kinematics. The velocity could not influence the potential injuries according to the risk of bone fracture. Additionally velocity has an incidence on the upper cervical spine potential injuries with higher amplitude recorded. If fuses areas could be clearly established on the upper and lower cervical spine, enlarge investigation are needed to promote new injury criteria for neck segment. Such investigation could also be followed by significant improvement in model to properly describe fracture processes.

Impact	1 st injury	2 nd injury	3 rd injury
Frontal	ALL at C1-2	C6	C5
Lateral	C6	C1-2	C5&CLR&LF at C5-6
Rear	ISL at C1-2	PLL	LF at C4-6
Frontal oblique	C6	C5&AL	C4&AlarLig
Rear oblique	ISL at C1-2	C5	ISL at C2-3

Table 3 The injury chronology in these tests

References

- [1] Franckel N., *Basic biomechanics of the musculoskeletal system* third edition, ISBN 0-683-30247-7
- [2] Panjabi MM, Cholewicki J, Nibu K, Babat LB, Dvorak J, *Simulation of whiplash trauma using whole cervical spine specimens*, Spine, 23(1), 17-24, Jan 1998
- [3] Panjabi MM, Cholewicki J, Nibu K, Grauer JN, Babat LB, Dvorak J, Bar HF, *Biomechanics of whiplash injury*, Orthopade, 27(12), 813-9, December 1998
- [4] P. Tropiano, L. Thollon, P. J. Arnoux, K. Kayvantash, C. Brunet, D.G.Poitout, *Simulation d'un traumatisme du rachis cervical par impact postérieur (Whiplash) à l'aide du modèle HUMOS*, e-mémoires de l'Académie Nationale de Chirurgie, 2003, 2 (1) : 24-30
- [5] J. Cholewicki, M.M. Panjabi, K. Nibu, L.B. Babat, J.N. Grauer and J. Dvorak, *Head kinematics during in vitro whiplash simulation*, Accid Anal Prev 30 (1998), pp. 469–479.
- [6] Ito S, Ivancic PC, Panjabi MM, et al. *Soft tissue injury threshold during simulated whiplash: a biomechanical investigation*. Spine 2004;29(9):979-87
- [7] Yoganandan N, Kumaresan S, Pintar FA., *Biomechanics of the cervical spine Part 2: Cervical spine soft tissue responses and biomechanical modeling*. Clin Biomech (Bristol Avon) 2001 jan;16(1):1-27



Session 4

Impact Biomechanics

Mrs. Caroline Deck
University of Strasbourg
France
deck@imfs.u-strasbg.fr



“Improved Model Based Head Injury Criteria”

C. Deck, R. Willinger

Keywords: Human head finite element model, accident reconstruction, head injury criteria

Summary:

This paper presents an original numerical human head FE models followed by its modal and temporal validation against human head vibration analysis in vivo and cadaver impact tests from the literature. The human head FE model developed presents two particularities : one at the brain-skull interface level where fluid-structure interaction is taken into account, the other at the skull modelling level by integrating the bone fracture simulation. Validation shows that the model correlated well with a number of experimental cadaver tests including skull deformation and rupture, intra-cranial pressure and brain deformation. This improved numerical human head surrogate has then been used for numerical real world accident simulation. Helmet damage from thirteen motorcycle accidents was replicated in drop tests in order to define the head's loading conditions. A total of twenty two well documented American football head trauma have been reconstructed as well as twenty eight pedestrian head impacts and six formula one head traumas. By correlating head injury type and location with intra-cerebral mechanical field parameters, it was possible to derive new injury risk curves for injuries as different as skull fracture, subdural haematoma and neurological injury. Illustrations of how this new head injury prediction tool can participate to the head protection system optimisation is also provided.

Virtual Trauma of Petrous bone fracture under lateral impact : from medical images to fracture process evaluation.

M. Montava¹, S. Bidal², J.P. Lavieille¹, P.J. Arnoux³, C. Brunet³

Service ORL et Chirurgie Cervico-Faciale, Hôpital Nord, APHM
Altair Development France
Laboratoire de Biomécanique Appliquée, UMR T 24, INRETS - UNIVERSITE DE LA MEDITERRANEE

Introduction

Head trauma, reported in sport injury and road accident analysis, frequently induce complex injury of Petrous bone. Such bone fractures are assumed to occur during lateral or posterior impact on the head [1, 2].

The location of the trauma on head structure, specifically on the Petrous bone area, concerns facial nerves, vestibule, cochlea, internal carotid artery. Over the lethal risk, the pathology associated to these injuries could be very severe from facial paralysis, vestibular trauma, tinnitus, deafness, vascular injuries and high blood pressure in skull [3].

Hence in order to provide a better understanding of this trauma, based on recent advance in medical data processing, a detailed numerical model of the Petrous bone structure was built. Lateral impact simulation was performed, leading to investigate macroscopic damage process of Petrous bone trauma and their anatomical correlation with clinical potential pathologies.

Materials and methods

A CT-Scan of a volunteer without pathology in relation with the Petrous bone was used to build a numerical model. Using Scan2Mesh [6], a tool dedicated to the generation of a mesh from medical data, 169 slices separated by a thickness of 0.6 millimeters were processed, using an automatic detection method based on thresholding. Then an anatomist checked the detected contours of the bone in order to validate them. Once the contours were validated on the whole 3D data, they were processed by the Marching-Octaedra algorithm, a fast and precise 3D reconstruction method [4], which leads to a 3D reconstruction of the bone and its mesh. The 3D Petrous bone mesh obtained is composed by tria/tetra elements, including cortical bone and spongy bone components (Fig. 1).

The bone structure was assumed to be isotropic. Spongy and compact bone material were simulated using an elastoplastic behaviour coupled to a Lemaitre damage model. The bone material set of parameters were obtained from previous works [5] (cf. table 1). Physical failure was simulated by a kill element method.

To investigate damage process on the bone structure, a lateral impact of a 50Kg wall launched at an initial velocity of 7m/s was simulated. In order to take into account the whole head structure effects, the petro occipitalis synostosis (a, Fig. 1) was fully blocked, and outer areas (b, Fig. 1) were only fixed in X directions (b, Fig. 1). Then forces level and stress distribution were recorded up to physical bone fracture process. These data were investigated in order to evaluate Petrous bone fracture mechanism and obtain the map of complete bone fracture.

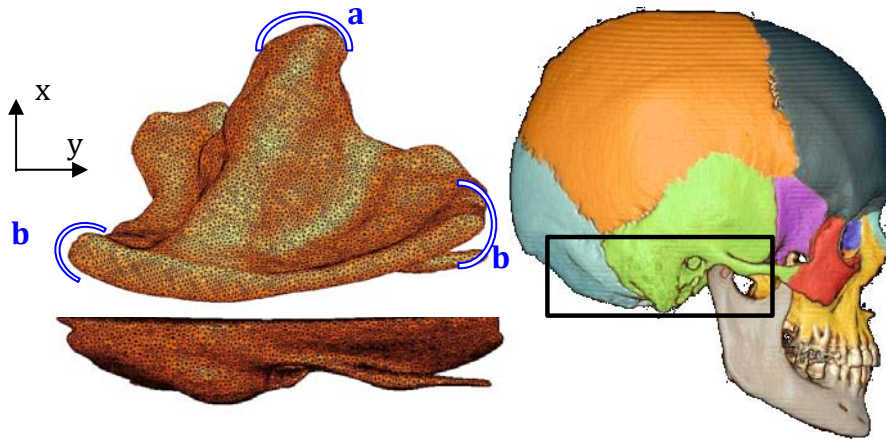


Figure 1 : Petrous bone model overview

Spongious bone		Law 23 (Elastic Plastic law with Damage Material)				
Density	Young's modulus	Poisson's ratio	Plasticity yield stress	Plasticity hardening parameter	Failure plastic strain	Plasticity maximum stress
0.00024	550	0.3	130	20	8%	40
Cortical bone		Johnson-Cook Material Law				
Density	Young's modulus	Poisson's ratio	Plasticity yield stress	Plasticity hardening parameter	Failure plastic strain	Plasticity maximum stress
0.0021	8000	0.3	80	100	3%	125

Table 1 :Material laws used for bone

Results

According to the complex geometry of bone structure (which could be compared to a pyramidal shape with an oblique direction to head centre point), its recruitment process, as recorded through Von Mises stress distribution, follows Petrous bone axes up to be transferred to lateral components.

From forces versus time curves (Fig. 2), the structure failure process spent less than 1.5 ms from impact point. From this time, three peaks were recorded.

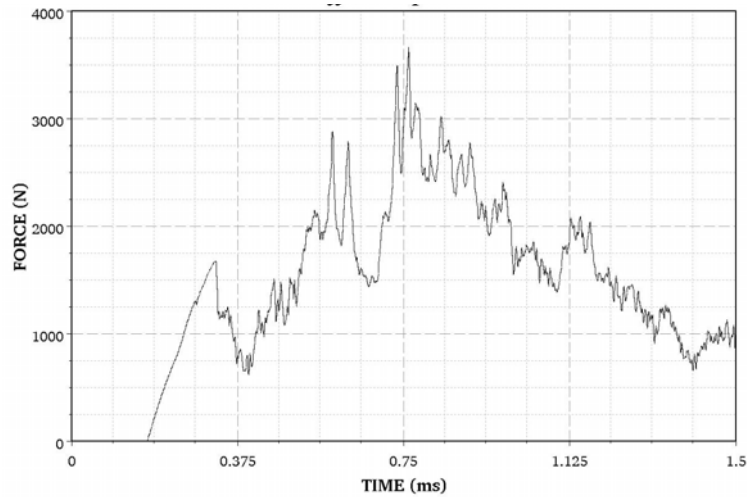


Figure 2 : Impact force

The first peak seems to be correlated to the impact on diploid structure and its related damage (Fig. 3).

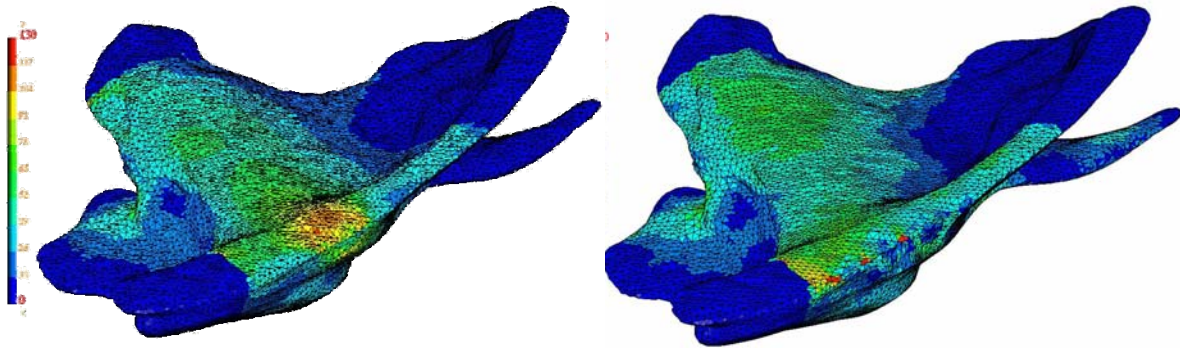


Figure 3 : Stress distribution and damage process at impact time

The two next peaks are in relation with the Petrous bone fracture propagation (Fig. 4).

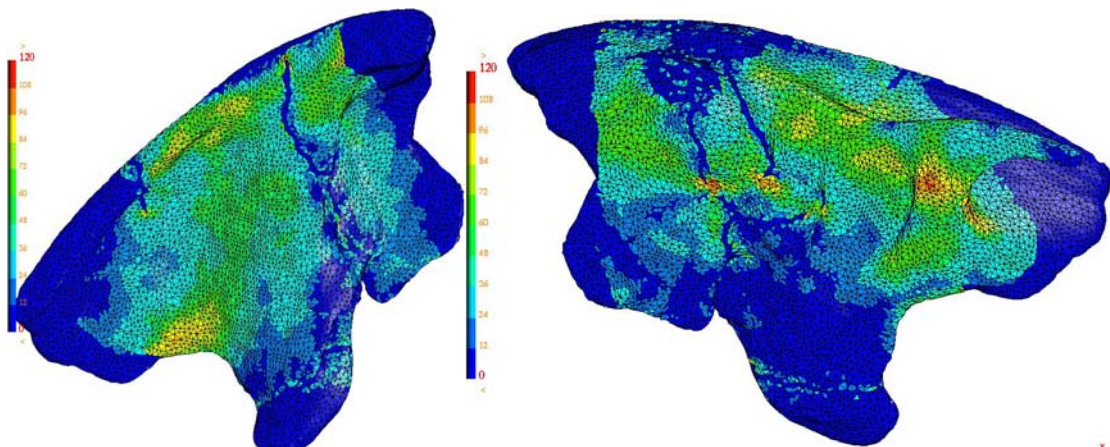


Figure 4 : Overview of bone fracture distribution at complete Petrous bone fracture

The fracture location obtained by simulation is relevant with real fracture longitudinal location. The Petrous bone fracture process converges to tympanal bone, to meatus acusticus externus associated to longitudinal fracture from the mastoid petrous bone joint to the the

vestibule of the internal ear. According to anatomical consideration, bone fracture location is closed to main vascular structure, nerves and hearing structure of the ear area. This fracture location could explain clinically observed trauma.

Discussion – Conclusion

A precise numerical model of the isolated Petrous bone structure was built from CT-scan data and used to investigate the fracture process occurring during a lateral impact. The fracture location on diploid structure, and then across Petrous bone, were evaluated. The fractures convergence is relevant with the longitudinal fracture classification. The fracture location on the mean ear area confirm the severity of induce trauma due to the important vascular and nervous structures being injured.

The fracture process map was reported as relevant with clinical data. These first results should be now completed by taken into account the whole head structure. According to the complex shape of Petrous bone, the numerical simulation seems to show a convergence area of fractures to the area of the external ear and mean ear. Further analysis and reconstruction of medical data, will integrate structure porosity effects and soft tissue component.

Additional work need to be done to investigate sensitivity of fracture process to speed and impact. However this approach could be used to complete existing fracture classification according to the accurate location of fracture and its consequences on surrounding soft tissues.

References

[1] Ramírez Sabio JB, de Paula Vernetta C, García Sanchís JM, Callejo García FJ, Cortés Andrés O, Quilis Quesada V, Dualde Beltrán D, Marco Algarra J. *Petrous bone fracture. Our experience: 1999-2004*, Acta Otorrinolaringol Esp. 2006 Dec;57(10):450-4. Spanish.

[2] Chays A, Girard N, Magnan J., *Fracture du rocher en urgence*, In: Tran Ba Huy P. Manach Y (coord.) Les Urgences en ORL. Paris: Société Française d'ORL et chirurgie cervico-faciale. Ed. 2002:365-82.

[3] Brodie HA, Thompson TC., Management of complications from 820 temporal bone fractures. Am J Otol. 1997 Mar;18(2):188-97.

[4] Bidal S, Serre T, Kayvantash K, Brunet C, *From organs' 2D contours detection to biofidelis finite element meshes generation*, 9th Numérisation 3D - Human Modelling, Paris, 28th&29th of April 2004

[5] Behr M., Arnoux P.J., Serre T., Bidal S., Kang H. S., Thollon L., Cavallero C., Kayvantash K., Brunet C., A Human model for Road Safety : From geometrical acquisition to Model Validation with Radioss. International Journal on Computer Methods in Biomechanics and Biomedical Engineering. Vol. 6, 4, pp.263, 2003

[6] Scan2Mesh - Hypercrash Reference Guide, Hyperworks, Altair, www.altair.com



Session 4

Impact Biomechanics

Mr. Jean-François Libra

INRETS

France

jean-francois.libra@inrets.fr



“Kinematics and Injury patterns of Vulnerable road users involved in road accidents with commercial Vehicles”

J.F. Libra, P. Beillas, JP Verriest

Keywords: vulnerable road user, commercial vehicles, injury

Summary:

Urban Commercial Vehicles (CV) include delivery trucks, light trucks, vans and public transportation vehicles (coaches, buses and tram). Because of the nature of their urban activities, they share a common space with Vulnerable Road Users (VRU). Although resulting road accidents are relatively uncommon, they are often very serious: in France in 2001, pedestrians involved in accidents with CV represented only 7.9% of all pedestrian victims but 20.1% of the fatalities. Other studies also show that the thoracic injuries are more common in pedestrian accidents involving vertical vans. CV are very diverse, with geometrical characteristics ranging from vertical trucks and buses to vans with small bonnets. In general, CV differs from automobiles in terms of mass, materials, external shape and front structure. Using rigid body dynamics, this study aims to estimate the effects of vehicle shape and stiffness on the kinematics and dynamics of pedestrians and cyclists during an accident. A simplified parametric model of the front of a vehicle, designed to simulate the transition of physical characteristics from automobiles to vans to vertical trucks and buses was used to impact VRU models. The results suggest that the verticality of the vehicle affects the pedestrian kinematics, with the wrap around kinematics disappearing gradually during the transition between small vans and vertical vehicles, affecting the trajectory and therefore the risk of run over. The thorax and the abdomen are also subjected to increasing loading during the transition from automobile to CV, which may be one of the causes explaining the difference in injury patterns between the two types of vehicles.